

การเตรียม  $Ba_{0.5}Sr_{0.5}Co_{0.8}Fe_{0.2}O_{3-\delta}$  เพอร์อฟสไกต์โคป  
เป็นแคโทดสำหรับเซลล์เชื้อเพลิงออกไซด์ของแข็ง

นางสาว สุวิชา ดีหะสิงห์

วิทยานิพนธ์นี้เป็นส่วนหนึ่งของการศึกษาตามหลักสูตรปริญญาวิทยาศาสตรมหาบัณฑิต  
สาขาวิชาปิโตรเคมีและวิทยาศาสตร์พอลิเมอร์  
คณะวิทยาศาสตร์ จุฬาลงกรณ์มหาวิทยาลัย  
ปีการศึกษา 2553  
ลิขสิทธิ์ของจุฬาลงกรณ์มหาวิทยาลัย

PREPARATION OF DOPED  $\text{Ba}_{0.5}\text{Sr}_{0.5}\text{Co}_{0.8}\text{Fe}_{0.2}\text{O}_{3-\delta}$  PEROVSKITES AS  
CATHODE FOR SOLID OXIDE FUEL CELL

Miss Suwichar Deehasing

A Thesis Submitted in Partial Fulfillment of the Requirements  
for the Degree of Master of Science Program in Petrochemistry and Polymer Science

Faculty of Science

Chulalongkorn University

Academic Year 2010

Copyright of Chulalongkorn University

Thesis Title            PREPARATION OF DOPED Ba<sub>0.5</sub>Sr<sub>0.5</sub>Co<sub>0.8</sub>Fe<sub>0.2</sub>O<sub>3-δ</sub>  
PEROVSKITES AS CATHODE FOR SOLID OXIDE FUEL  
CELL  
By                         Miss Suwichar Deehasing  
Field of Study         Petrochemistry and Polymer Science  
Thesis Advisor        Assistant Professor Soamwadee Chaianansutcharit, Ph.D.  
Thesis Co-Advisor    Assistant Professor Oravan Sanguanruang, Ph.D.

---

Accepted by the Faculty of Science, Chulalongkorn University in Partial  
Fulfillment of the Requirements for the Master's Degree

.....Dean of the Faculty of Science  
(Professor Supot Hannongbua, Dr.rer.nat)

#### THESIS COMMITTEE

.....Chairman  
(Professor Pattarapan Prasassarakich, Ph.D.)

.....Thesis Advisor  
(Assistant Professor Soamwadee Chaianansutcharit, Ph.D.)

.....Thesis Co-Advisor  
(Assistant Professor Oravan Sanguanruang, Ph.D.)

.....Examiner  
(Associate Professor Wimonrat Trakarnpruk, Ph.D.)

.....External Examiner  
(Siriporn Larpeattavorn, Ph.D.)

สุวิชา ดีหะสิงห์ : การเตรียม  $\text{Ba}_{0.5}\text{Sr}_{0.5}\text{Co}_{0.8}\text{Fe}_{0.2}\text{O}_{3-\delta}$  เพอรอฟสไกต์โคปเป็นแคโทด สำหรับเซลล์เชื้อเพลิงออกไซด์ของแข็ง . (PREPARATION OF DOPED  $\text{Ba}_{0.5}\text{Sr}_{0.5}\text{Co}_{0.8}\text{Fe}_{0.2}\text{O}_{3-\delta}$  PEROVSKITES AS CATHODE FOR SOLID OXIDE FUEL CELL) อ. ที่ปรึกษาวิทยานิพนธ์หลัก : ผศ.ดร. โสภวดี ไชยอนันต์สุจริต, อ. ที่ปรึกษาวิทยานิพนธ์ร่วม : ผศ.ดร. อรวรรณ สงวนเรือง, 99 หน้า.

การแทนที่ไอออน  $\text{Ca}^{2+}$  และ  $\text{La}^{3+}$  ที่ตำแหน่ง A และการเติมไอออน  $\text{Ca}^{2+}$ ,  $\text{Cu}^{2+}$  และ  $\text{Zn}^{2+}$  ในโครงสร้างของ BSCF สามารถเตรียมได้จากวิธีสังเคราะห์แบบการตรวจสอบเอกลักษณ์ด้วยเทคนิค XRD และ SEM แสดงให้เห็นว่าสารตัวอย่างทั้งหมดแสดงเฟสเดี่ยวของลูกบาศก์  $\text{ABO}_3$  เพอรอฟสไกต์ออกไซด์ ยกเว้น BSCF ที่ถูกแทนที่ด้วยไอออนของ  $\text{Ca}^{2+}$  สัดส่วน 40 เปอร์เซ็นต์โดยโมล ในตำแหน่ง A ยังคงปรากฏสารเจือปนของ CaO เล็กน้อย ค่าการนำไฟฟ้าของสารตัวอย่างเพิ่มขึ้นเมื่อการเพิ่ม การแทนที่ของไอออน  $\text{Ca}^{2+}$  และพบค่าการนำไฟฟ้าสูงสุดที่ 96 ซีเมนต่อเซนติเมตร ที่อุณหภูมิ 650 องศาเซลเซียส จาก  $\text{Ca}^{2+}$  30 เปอร์เซ็นต์โดยโมล ผลของ  $\text{O}_2$ -TPD ซึ่งให้ให้เห็นว่า การแทนที่ด้วยไอออน  $\text{Ca}^{2+}$  ที่ตำแหน่ง A จะทำให้ค่าการคายออกซิเจนสูงขึ้น นอกจากนี้ การแทนที่ไอออน  $\text{Ca}^{2+}$  ในไอออน  $\text{La}^{3+}$  ของ BSLCF มีผลต่อการลดลงของค่าการนำไฟฟ้า และพบค่าการนำไฟฟ้าสูงสุดใน BSLCF ซึ่งมีค่าเท่ากับ 353 ซีเมนต่อเซนติเมตร ที่อุณหภูมิ 350 องศาเซลเซียส นอกจากนี้ BSLCF $\text{Ca}_{0.01}$  ให้ค่าการนำไฟฟ้าสูงสุดที่ 593 ซีเมนต่อเซนติเมตร ที่อุณหภูมิ 350 องศาเซลเซียส และการเติมไอออนของ  $\text{Cu}^{2+}$  และ  $\text{Zn}^{2+}$  ไม่มีผลต่อการเพิ่มค่าการนำไฟฟ้าของวัสดุ

สาขาวิชา.....ปิโตรเคมีและวิทยาศาสตร์พอลิเมอร์.....ลายมือชื่อนิสิต.....

ปีการศึกษา.....2553.....ลายมือชื่อ อ.ที่ปรึกษาวิทยานิพนธ์หลัก.....

ลายมือชื่อ อ.ที่ปรึกษาวิทยานิพนธ์ร่วม.....

# # 5072540823: MAJOR PETROCHEMISTRY AND POLYMER SCIENCE  
 KEYWORDS: PEROVSKITE OXIDE/ CATHODE MATERIAL/  $ABO_3$   
 STRUCTURE/ OXYGEN PERMEATION/ ELECTRICAL CONDUCTIVITY

SUWICHAR DEEHASING: PREPARATION OF DOPED  $Ba_{0.5}Sr_{0.5}Co_{0.8}Fe_{0.2}O_{3-\delta}$  PEROVSKITES AS CATHODE FOR SOLID OXIDE FUEL CELL. THESIS ADVISOR: ASST. PROF. SOAMWADEE CHAIANANSUTCHARIT, Ph.D., THESIS CO-ADVISOR: ASST. PROF. ORAVAN SANGUANRUANG, Ph.D., 99 pp.

The substitution of  $Ca^{2+}$  and  $La^{3+}$  ions at A-site and the addition of  $Ca^{2+}$ ,  $Cu^{2+}$  and  $Zn^{2+}$  ions in the structure of  $Ba_{0.5}Sr_{0.5}Co_{0.8}Fe_{0.2}O_{3-\delta}$  (BSCF) were successfully performed by the modified citrate method. The characterization by XRD and SEM demonstrated that all samples showed the single phase of cubic  $ABO_3$  perovskite oxide however the BSCF substituted by  $Ca^{2+}$  ion at 40 mol% in A-site still presenting small impurity phase of CaO. The electrical conductivity was increased with the increasing substitution of  $Ca^{2+}$  ion and the maximum electrical conductivity was  $96 \text{ S}\cdot\text{cm}^{-1}$  at  $650^\circ\text{C}$  for the BSCCF (Ca 30 mol%). The results of  $O_2$ -TPD indicated the substitution of  $Ca^{2+}$  ion in A-site showed the increasing of oxygen desorption. Furthermore, the substitution of  $Ca^{2+}$  ion in  $La^{3+}$  ion of the BSLCF affected the decreasing of electrical conductivity and the maximum conductivity achieved from the BSLCF was  $353 \text{ S}\cdot\text{cm}^{-1}$  at  $350^\circ\text{C}$ . In addition, the electrical conductivity of the BSLCF $Ca_{0.01}$  showed the maximum value of  $593 \text{ S}\cdot\text{cm}^{-1}$  at  $350^\circ\text{C}$  and the addition of  $Cu^{2+}$  and  $Zn^{2+}$  ions not had the affected on the electrical conductivity of materials.

Field of Study: Petrochemistry and Polymer Science Student's Signature:.....

Academic year:.....2010..... Advisor's Signature:.....

Co-Advisor's Signature:.....

## ACKNOWLEDGEMENTS

The author wishes to express greatest gratitude to Assistant Professor Dr. Soamwadee Chaianansutcharit, advisor and Assistant Professor Dr. Oravan Saganruang, co-advisor, for their kindness, valuable advices and encouragement throughout this research. Especially, she deeply gratitude to Professor Dr. Kazunori SATO, Nagaoka University of Technology, Japan, JENESYS program advisor for his kindness, valuable advices during she stayed in Japan.

In addition, the author wishes to express appreciation to Professor Dr. Pattarapan Prasassarakich, Associate Professor Dr. Wimonrat Trakarnpruk, and Dr. Siriporn Larpkeattavorn for serving as the chairman and members of this thesis committee, respectively, for all of their valuable advices and comments in the research.

The author would like to thank Rachadapiseksomphot Endowment, and Graduate school Chulalongkorn University for financial supports and appreciation is also extended to National Center of Excellence for Petroleum, Petrochemical and Advanced Materials through Program of Petrochemistry and Polymer Science for educational scholarship. Moreover, she would like to acknowledge the financial support by a JENESYS scholarship 2009 at Nagaoka University of Technology, Japan. Thanks for Department of Chemistry, Faculty of Science for research facilities.

For all of her friends in laboratory, the members of Materials Chemistry and Catalysis Research Unit and her friends in laboratory at Japan, Dr.Tanawat Kanjanaboonmalert and Miss Jiratchaya Ayawanna, she greatly appreciate their kind assistance, generosity and encouragement throughout the course of her research.

Finally, she would like to express her deepest gratitude to her family specially her father, mother and sister for their love, entirely care and encouragement. The usefulness of this thesis, she dedicate to her family and all teachers who have taught her since her childhood.

# CONTENTS

	<b>Page</b>
<b>ABSTRACT IN THAI</b> .....	iv
<b>ABSTRACT IN ENGLISH</b> .....	v
<b>ACKNOWLEDGEMENTS</b> .....	vi
<b>CONTENTS</b> .....	vii
<b>LIST OF TABLES</b> .....	xii
<b>LIST OF FIGURES</b> .....	xiv
<b>LIST OF ABBREVIATIONS</b> .....	xvii
<b>CHAPTER I INTRODUCTION</b> .....	1
1.1 Fuel cell .....	1
1.2 Solid oxide fuel cells .....	2
1.2.1 Electrolyte for SOFC .....	4
1.2.2 Anode for SOFC .....	4
1.2.3 Cathode for SOFC .....	5
1.2.4 Interconnect .....	6
1.3 Perovskite .....	7
1.4 Literature reviews .....	8
1.5 The objective of the thesis .....	12
<b>CHAPTER II THEORY</b> .....	13
2.1 Fuel cell .....	13
2.2 Solid oxide fuel cell .....	14
2.3 Perovskite oxide .....	15
2.3.1 Crystal structure of perovskite oxide .....	15
2.3.2 Oxygen nonstoichiometry .....	17
2.4 Physical properties of perovskite .....	17
2.4.1 Magnetic properties .....	18
2.4.2 Electrical properties .....	18

	<b>Page</b>
2.4.2.1 n-type extrinsic semiconductor.....	19
2.4.2.2 p-type extrinsic semiconductor.....	19
2.4.3 Mixed electric-ionic conductors.....	21
2.4.4 Thermal expansion.....	22
2.4.5 Oxygen adsorption property.....	23
2.5 Perovskite synthesis .....	23
2.5.1 Solid state reaction.....	24
2.5.2 Solution preparation.....	24
2.5.2.1 Sol gel method.....	25
2.5.2.2 Co-precipitation process.....	27
2.6 Powder sizing.....	27
2.6.1 Powder compacting by uniaxial pressing.....	28
2.7 Sintering.....	29
2.7.1 Mechanism of sintering.....	29
2.8 Electrical measurement.....	32
<b>CHAPTER III EXPERIMENTAL.....</b>	<b>33</b>
3.1 Chemicals.....	33
3.2 Synthesis of perovskite oxide powder by modified citrate method.....	34
3.3 Characterization techniques.....	36
3.3.1 x-ray diffractometry (XRD).....	36
3.3.2 scanning electron microscopy (SEM).....	36
3.3.3 electron probe micro analyzer (EPMA).....	36
3.3.4 relative density.....	37
3.3.5 temperature programmed desorption (TPD).....	37
3.3.6 electrical conductivity measurement.....	37
3.3.7 dilatometer.....	39



	<b>Page</b>
<b>CHAPTER IV RESULTS AND DISSCUSSION</b> .....	40
4.1 Preparation and properties of $(\text{Ba}_{0.5}\text{Sr}_{0.5})_{1-x}\text{Ca}_x\text{Co}_{0.8}\text{Fe}_{0.2}\text{O}_{3-\delta}$ (BSCCF), $(0 \leq x \leq 0.5)$ perovskite oxide .....	40
4.1.1 Phase formation of $(\text{Ba}_{0.5}\text{Sr}_{0.5})_{1-x}\text{Ca}_x\text{Co}_{0.8}\text{Fe}_{0.2}\text{O}_{3-\delta}$ perovskite .....	40
4.1.2 The surface morphology of $(\text{Ba}_{0.5}\text{Sr}_{0.5})_{1-x}\text{Ca}_x$ $\text{Co}_{0.8}\text{Fe}_{0.2}\text{O}_{3-\delta}$ , $(0 \leq x \leq 0.4)$ .....	42
4.1.3 Electrical conductivity of $(\text{Ba}_{0.5}\text{Sr}_{0.5})_{1-x}\text{Ca}_x$ $\text{Co}_{0.8}\text{Fe}_{0.2}\text{O}_{3-\delta}$ , $(0 \leq x \leq 0.4)$ .....	45
4.1.4 Temperature programmed desorption of $(\text{Ba}_{0.5}\text{Sr}_{0.5})_{1-x}\text{Ca}_x\text{Co}_{0.8}\text{Fe}_{0.2}\text{O}_{3-\delta}$ , $(0 \leq x \leq 0.4)$ .....	47
4.1.5 Thermal expansion of $(\text{Ba}_{0.5}\text{Sr}_{0.5})_{1-x}\text{Ca}_x\text{Co}_{0.8}\text{Fe}_{0.2}\text{O}_{3-\delta}$ , $(0 \leq x \leq 0.4)$ .....	48
4.2 Preparation and properties of $(\text{Ba}_{0.5}\text{Sr}_{0.5})_{0.8}\text{La}_{0.2-x}\text{Ca}_x\text{Co}_{0.8}\text{Fe}_{0.2}\text{O}_{3-\delta}$ (BSLCCF), $(0 \leq x \leq 0.15)$ perovskite oxide .....	50
4.2.1 Phase formation of $(\text{Ba}_{0.5}\text{Sr}_{0.5})_{0.8}\text{La}_{0.2-x}\text{Ca}_x$ $\text{Co}_{0.8}\text{Fe}_{0.2}\text{O}_{3-\delta}$ perovskite .....	50
4.2.2 The surface morphology of $(\text{Ba}_{0.5}\text{Sr}_{0.5})_{0.8}\text{La}_{0.2-x}\text{Ca}_x$ $\text{Co}_{0.8}\text{Fe}_{0.2}\text{O}_{3-\delta}$ , (BSLCF), $(0 \leq x \leq 0.15)$ .....	52
4.2.3 Electrical conductivity of $(\text{Ba}_{0.5}\text{Sr}_{0.5})_{0.8}\text{La}_{0.2-x}\text{Ca}_x\text{Co}_{0.8}\text{Fe}_{0.2}\text{O}_{3-\delta}$ , $(0 \leq x \leq 0.15)$ .....	55
4.2.4 Temperature programmed desorption of $(\text{Ba}_{0.5}\text{Sr}_{0.5})_{0.8}\text{La}_{0.2-x}\text{Ca}_x\text{Co}_{0.8}\text{Fe}_{0.2}\text{O}_{3-\delta}$ , $(0 \leq x \leq 0.15)$ .....	57
4.2.5 Thermal expansion of $(\text{Ba}_{0.5}\text{Sr}_{0.5})_{0.8}\text{La}_{0.2-x}\text{Ca}_x\text{Co}_{0.8}\text{Fe}_{0.2}\text{O}_{3-\delta}$ , $(0 \leq x \leq 0.15)$ .....	58
4.3 Preparation and properties of $(\text{Ba}_{0.5}\text{Sr}_{0.5})_{0.8}\text{La}_{0.2}\text{Co}_{0.8}\text{Fe}_{0.2}\text{Ca}_x\text{O}_{3-\delta}$ (BSLCFCa), $(0 \leq x \leq 0.05)$ perovskite oxide .....	60
4.3.1 Phase formation of $(\text{Ba}_{0.5}\text{Sr}_{0.5})_{0.8}\text{La}_{0.2}\text{Co}_{0.8}\text{Fe}_{0.2}\text{Ca}_x\text{O}_{3-\delta}$ perovskite .....	60

	<b>Page</b>
4.3.2 The surface morphology of (Ba <sub>0.5</sub> Sr <sub>0.5</sub> ) <sub>0.8</sub> La <sub>0.2</sub> Co <sub>0.8</sub> Fe <sub>0.2</sub> Ca <sub>x</sub> O <sub>3-δ</sub> .....	62
4.3.3 Electrical conductivity of (Ba <sub>0.5</sub> Sr <sub>0.5</sub> ) <sub>0.8</sub> La <sub>0.2</sub> Co <sub>0.8</sub> Fe <sub>0.2</sub> Ca <sub>x</sub> O <sub>3-δ</sub> , (x = 0 and 0.01).....	64
4.3.4 Temperature programmed desorption of (Ba <sub>0.5</sub> Sr <sub>0.5</sub> ) <sub>0.8</sub> La <sub>0.2</sub> Co <sub>0.8</sub> Fe <sub>0.2</sub> Ca <sub>x</sub> O <sub>3-δ</sub> , (x = 0 and 0.01).....	65
4.3.5 Thermal expansion of (Ba <sub>0.5</sub> Sr <sub>0.5</sub> ) <sub>0.8</sub> La <sub>0.2</sub> Co <sub>0.8</sub> Fe <sub>0.2</sub> Ca <sub>x</sub> O <sub>3-δ</sub> , (x = 0 and 0.01).....	67
4.4 Preparation and properties of (Ba <sub>0.5</sub> Sr <sub>0.5</sub> ) <sub>0.8</sub> Co <sub>0.8</sub> Fe <sub>0.2</sub> Cu <sub>x</sub> O <sub>3-δ</sub> (BSCFCu), (0 ≤ x ≤ 0.2) perovskite oxide.....	68
4.4.1 Phase formation of (Ba <sub>0.5</sub> Sr <sub>0.5</sub> ) <sub>0.8</sub> Co <sub>0.8</sub> Fe <sub>0.2</sub> Cu <sub>x</sub> O <sub>3-δ</sub> perovskite.....	69
4.4.2 The surface morphology of (Ba <sub>0.5</sub> Sr <sub>0.5</sub> ) <sub>0.8</sub> Co <sub>0.8</sub> Fe <sub>0.2</sub> Cu <sub>x</sub> O <sub>3-δ</sub> BSCFCu, (0 ≤ x ≤ 0.2).....	70
4.4.3 Electrical conductivity of (Ba <sub>0.5</sub> Sr <sub>0.5</sub> ) <sub>0.8</sub> Co <sub>0.8</sub> Fe <sub>0.2</sub> Cu <sub>x</sub> O <sub>3-δ</sub> BSCFCu, (0 ≤ x ≤ 0.2).....	73
4.4.4 Temperature programmed desorption of (Ba <sub>0.5</sub> Sr <sub>0.5</sub> ) <sub>0.8</sub> Co <sub>0.8</sub> Fe <sub>0.2</sub> Cu <sub>x</sub> O <sub>3-δ</sub> , (0 ≤ x ≤ 0.2).....	75
4.4.5 Thermal expansion of (Ba <sub>0.5</sub> Sr <sub>0.5</sub> ) <sub>0.8</sub> Co <sub>0.8</sub> Fe <sub>0.2</sub> Cu <sub>x</sub> O <sub>3-δ</sub> , (0 ≤ x ≤ 0.2).....	76
4.5 Preparation and properties of (Ba <sub>0.5</sub> Sr <sub>0.5</sub> ) <sub>0.8</sub> Co <sub>0.8</sub> Fe <sub>0.2</sub> Zn <sub>x</sub> O <sub>3-δ</sub> (BSCFZn), (0 ≤ x ≤ 0.2).....	78
4.5.1 Phase formation of (Ba <sub>0.5</sub> Sr <sub>0.5</sub> ) <sub>0.8</sub> Co <sub>0.8</sub> Fe <sub>0.2</sub> Zn <sub>x</sub> O <sub>3-δ</sub> perovskite.....	78
4.5.2 The surface morphology of (Ba <sub>0.5</sub> Sr <sub>0.5</sub> ) <sub>0.8</sub> Co <sub>0.8</sub> Fe <sub>0.2</sub> Zn <sub>x</sub> O <sub>3-δ</sub> BSCFZn, (0 ≤ x ≤ 0.2).....	80
4.5.3 Electrical conductivity of (Ba <sub>0.5</sub> Sr <sub>0.5</sub> ) <sub>0.8</sub> Co <sub>0.8</sub> Fe <sub>0.2</sub> Zn <sub>x</sub> O <sub>3-δ</sub> , (0 ≤ x ≤ 0.2).....	83

	<b>Page</b>
4.5.4 Temperature programmed desorption of $\text{Ba}_{0.5}\text{Sr}_{0.5})_{0.8}\text{Co}_{0.8}\text{Fe}_{0.2}\text{Zn}_x\text{O}_{3-\delta}$ .....	85
4.5.5 Thermal expansion of $(\text{Ba}_{0.5}\text{Sr}_{0.5})_{0.8}\text{Co}_{0.8}\text{Fe}_{0.2}\text{Zn}_x\text{O}_{3-\delta}$ , ( $0 \leq x \leq 0.2$ ).....	86
<b>CHAPTER IV CONCLUSIONS</b> .....	88
<b>REFERENCES</b> .....	91
<b>APPENDICES</b> .....	95
<b>VITAE</b> .....	99

## LIST OF TABLES

Table	Page
1.1 Type of fuel cells .....	3
2.1 Electrochemical reactions in fuel cell systems.....	13
3.1 Chemical and reagents for synthesis of perovskite oxide.....	33
3.2 The components of all samples.....	34
4.1 Lattice parameters and crystallite sizes of $(\text{Ba}_{0.5}\text{Sr}_{0.5})_{1-x}\text{Ca}_x\text{Co}_{0.8}\text{Fe}_{0.2}\text{O}_{3-\delta}$ ( $0 \leq x \leq 0.4$ ) powder after calcined at 1000°C for 5 hours.....	42
4.2 The relative density of $(\text{Ba}_{0.5}\text{Sr}_{0.5})_{1-x}\text{Ca}_x\text{Co}_{0.8}\text{Fe}_{0.2}\text{O}_{3-\delta}$ ( $0 \leq x \leq 0.4$ ) membrane after sintered at 1100°C.....	45
4.3 The electrical conductivity values of $(\text{Ba}_{0.5}\text{Sr}_{0.5})_{1-x}\text{Ca}_x\text{Co}_{0.8}\text{Fe}_{0.2}\text{O}_{3-\delta}$ , ( $0 \leq x \leq 0.4$ ) at various temperatures.....	46
4.4 Oxygen desorption peak area of $(\text{Ba}_{0.5}\text{Sr}_{0.5})_{1-x}\text{Ca}_x\text{Co}_{0.8}\text{Fe}_{0.2}\text{O}_{3-\delta}$ , ( $0 \leq x \leq 0.4$ ).....	48
4.5 Thermal expansion coefficients of BSCCF specimens at 50°C-800°C.....	49
4.6 Lattice parameters and crystallite sizes of $(\text{Ba}_{0.5}\text{Sr}_{0.5})_{0.8}\text{La}_{0.2-x}\text{Ca}_x\text{Co}_{0.8}\text{Fe}_{0.2}\text{O}_{3-\delta}$ ( $0 \leq x \leq 0.15$ ) powder after calcined.....	52
4.7 The relative density of $(\text{Ba}_{0.5}\text{Sr}_{0.5})_{0.8}\text{La}_{0.2-x}\text{Ca}_x\text{Co}_{0.8}\text{Fe}_{0.2}\text{O}_{3-\delta}$ , ( $0 \leq x \leq 0.15$ ).....	55
4.8 The electrical conductivity of $(\text{Ba}_{0.5}\text{Sr}_{0.5})_{0.8}\text{La}_{0.2-x}\text{Ca}_x\text{Co}_{0.8}\text{Fe}_{0.2}\text{O}_{3-\delta}$ , ( $0 \leq x \leq 0.15$ ) at various temperatures.....	56
4.9 Oxygen desorption peak area of BSCF, $(\text{Ba}_{0.5}\text{Sr}_{0.5})_{0.8}\text{La}_{0.2-x}\text{Ca}_x\text{Co}_{0.8}\text{Fe}_{0.2}\text{O}_{3-\delta}$ , ( $0 \leq x \leq 0.15$ ).....	58
4.10 Thermal expansion coefficients of BSLCCF specimens at 50°C to 800°C.....	59
4.11 Lattice parameter of $(\text{Ba}_{0.5}\text{Sr}_{0.5})_{0.8}\text{La}_{0.2}\text{Co}_{0.8}\text{Fe}_{0.2}\text{Ca}_x\text{O}_{3-\delta}$ , $x = 0$ and $0.01$ after calcined at 1000°C for 5 hours.....	61

<b>Table</b>	<b>Page</b>
<b>4.12</b> Relative density of $(\text{Ba}_{0.5}\text{Sr}_{0.5})_{0.8}\text{La}_{0.2}\text{Co}_{0.8}\text{Fe}_{0.2}\text{Ca}_x\text{O}_{3-\delta}$ , ( $x=0$ and $0.01$ ).....	63
<b>4.13</b> The electrical conductivity of $(\text{Ba}_{0.5}\text{Sr}_{0.5})_{0.8}\text{La}_{0.2}\text{Co}_{0.8}\text{Fe}_{0.2}\text{Ca}_x\text{O}_{3-\delta}$ , ( $x = 0$ and $0.01$ ) at various temperature.....	65
<b>4.14</b> Oxygen desorption peak area of $\text{Ba}_{0.5}\text{Sr}_{0.5}\text{La}_{0.2}\text{Co}_{0.8}\text{Fe}_{0.2}\text{Ca}_x\text{O}_{3-\delta}$ , ( $x = 0$ and $0.01$ ).....	66
<b>4.15</b> Thermal expansion coefficients of BSLCFCa <sub>0.01</sub> specimens at $50^\circ\text{C}$ to $800^\circ\text{C}$ .....	68
<b>4.16</b> Lattice parameters and crystallite sizes of $\text{Ba}_{0.5}\text{Sr}_{0.5}\text{Co}_{0.8}\text{Fe}_{0.2}$ $\text{Cu}_x\text{O}_{3-\delta}$ ( $0 \leq x \leq 0.2$ ) powder after calcined.....	70
<b>4.17</b> Relative density of $\text{Ba}_{0.5}\text{Sr}_{0.5}\text{Co}_{0.8}\text{Fe}_{0.2}\text{Cu}_x\text{O}_{3-\delta}$ , ( $0 \leq x \leq 0.2$ ).....	73
<b>4.18</b> The electrical conductivity of $\text{Ba}_{0.5}\text{Sr}_{0.5}\text{Co}_{0.8}\text{Fe}_{0.2}\text{Cu}_x\text{O}_{3-\delta}$ , ( $0 \leq x \leq 0.2$ ) at various temperature.....	74
<b>4.19</b> Oxygen desorption peak area of $\text{Ba}_{0.5}\text{Sr}_{0.5}\text{Co}_{0.8}\text{Fe}_{0.2}\text{Cu}_x\text{O}_{3-\delta}$ , ( $0 \leq x \leq 0.2$ ).....	76
<b>4.20</b> Thermal expansion coefficients of $\text{Ba}_{0.5}\text{Sr}_{0.5}\text{Co}_{0.8}\text{Fe}_{0.2}\text{Cu}_x\text{O}_{3-\delta}$ specimens at $50^\circ\text{C}$ to $800^\circ\text{C}$ .....	77
<b>4.21</b> Lattice parameters and crystallite sizes of $\text{Ba}_{0.5}\text{Sr}_{0.5}\text{Co}_{0.8}\text{Fe}_{0.2}\text{Zn}_x\text{O}_{3-\delta}$ ( $0 \leq x \leq 0.2$ ) powder after calcined.....	79
<b>4.22</b> Relative density of $\text{Ba}_{0.5}\text{Sr}_{0.5}\text{Co}_{0.8}\text{Fe}_{0.2}\text{Zn}_x\text{O}_{3-\delta}$ , ( $0 \leq x \leq 0.2$ ).....	83
<b>4.23</b> The electrical conductivity of $\text{Ba}_{0.5}\text{Sr}_{0.5}\text{Co}_{0.8}\text{Fe}_{0.2}\text{Zn}_x\text{O}_{3-\delta}$ , ( $0 \leq x \leq 0.2$ ) at various temperature.....	84
<b>4.24</b> Oxygen desorption peak area of $\text{Ba}_{0.5}\text{Sr}_{0.5}\text{Co}_{0.8}\text{Fe}_{0.2}\text{Zn}_x\text{O}_{3-\delta}$ , ( $0 \leq x \leq 0.2$ ).....	86
<b>4.25</b> Thermal expansion coefficients of $\text{Ba}_{0.5}\text{Sr}_{0.5}\text{Co}_{0.8}\text{Fe}_{0.2}\text{Zn}_x\text{O}_{3-\delta}$ specimens measured at $50^\circ\text{C}$ to $800^\circ\text{C}$ .....	87

## LIST OF FIGURES

<b>Figure</b>	<b>Page</b>
2.1 A planar design of SOFC .....	14
2.2 Lattice structure of $ABO_3$ perovskite.....	15
2.3 The relationship of ionic radii in a unit cell of perovskite structure.....	16
2.4 The mechanisms of sintering in crystalline particles model.....	30
2.5 The idealized models for the three stages of sintering	
a) Initial stage b) End of the initial stage c) Intermediate stage	
d) Final stage.....	31
2.6 DC 4-probes measurement.....	32
3.1 The rectangular sample wrapped with gold (Au) wire	
when $W = \text{wide}$ $L = \text{length}$ $T = \text{thickness}$ .....	38
4.1 XRD patterns of $(Ba_{0.5}Sr_{0.5})_{1-x}Ca_xCo_{0.8}Fe_{0.2}O_{3-\delta}$ , ( $0 \leq x \leq 0.5$ ) powder	
after calcined at $1000^\circ C$ for 5 hours .....	41
4.2 XRD patterns of $(Ba_{0.5}Sr_{0.5})_{1-x}Ca_xCo_{0.8}Fe_{0.2}O_{3-\delta}$ , ( $0 \leq x \leq 0.4$ ) membranes	
after sintered at $1100^\circ C$ for 10 hours.....	41
4.3 SEM micrograph of $(Ba_{0.5}Sr_{0.5})_{1-x}Ca_xCo_{0.8}Fe_{0.2}O_{3-\delta}$ , ( $0 \leq x \leq 0.4$ ) after	
sintered at $1100^\circ C$ for 10 hours.....	43
4.4 Surface morphology (a) and Ca-mapping of $(Ba_{0.5}Sr_{0.5})_{1-x}Ca_xCo_{0.8}Fe_{0.2}O_{3-\delta}$	
disc, ( $x=0.1, 0.2$ and $0.4$ ) (b).....	44
4.5 The electrical conductivity of $(Ba_{0.5}Sr_{0.5})_{1-x}Ca_xCo_{0.8}Fe_{0.2}O_{3-\delta}$ , ( $0 \leq x \leq 0.4$ )	
at $300^\circ C$ to $750^\circ C$ .....	46
4.6 Oxygen temperature programmed desorption curves of $(Ba_{0.5}Sr_{0.5})_{1-x}$	
$Ca_xCo_{0.8}Fe_{0.2}O_{3-\delta}$ , ( $0 \leq x \leq 0.4$ ) at $200^\circ C$ to $800^\circ C$ .....	47
4.7 Thermal expansion curves of Ca-doped A-site of $(Ba_{0.5}Sr_{0.5})_{1-x}Ca_x$	
$Co_{0.8}Fe_{0.2}O_{3-\delta}$ , ( $0 \leq x \leq 0.4$ ) at $50^\circ C$ to $800^\circ C$ .....	49
4.8 XRD patterns of $(Ba_{0.5}Sr_{0.5})_{0.8}La_{0.2-x}Ca_xCo_{0.8}Fe_{0.2}O_{3-\delta}$ , ( $0 \leq x \leq 0.15$ ) powder	
after calcined at $1000^\circ C$ for 5 hours.....	51

<b>Figure</b>	<b>Page</b>
<b>4.9</b> XRD patterns of $(\text{Ba}_{0.5}\text{Sr}_{0.5})_{0.8}\text{La}_{0.2-x}\text{Ca}_x\text{Co}_{0.8}\text{Fe}_{0.2}\text{O}_{3-\delta}$ , ( $0 \leq x \leq 0.15$ ) membranes after sintered at 1100°C for 10 hours.....	51
<b>4.10</b> SEM micrographs of $(\text{Ba}_{0.5}\text{Sr}_{0.5})_{0.8}\text{La}_{0.2-x}\text{Ca}_x\text{Co}_{0.8}\text{Fe}_{0.2}\text{O}_{3-\delta}$ , ( $0 \leq x \leq 0.15$ ) after sintered at 1100°C for 10 hours.....	53
<b>4.11</b> Surface morphology (a) and Ca-mapping of $(\text{Ba}_{0.5}\text{Sr}_{0.5})_{0.8}\text{La}_{0.2-x}\text{Ca}_x\text{Co}_{0.8}\text{Fe}_{0.2}\text{O}_{3-\delta}$ , ( $0.05 \leq x \leq 0.15$ ) discs (b).....	53
<b>4.12</b> The electrical conductivity of $(\text{Ba}_{0.5}\text{Sr}_{0.5})_{0.8}\text{La}_{0.2-x}\text{Ca}_x\text{Co}_{0.8}\text{Fe}_{0.2}\text{O}_{3-\delta}$ , ( $0 \leq x \leq 0.15$ ) at 300°C to 750°C.....	56
<b>4.13</b> Oxygen temperature programmed desorption curves of $(\text{Ba}_{0.5}\text{Sr}_{0.5})_{0.8}\text{La}_{0.2-x}\text{Ca}_x\text{Co}_{0.8}\text{Fe}_{0.2}\text{O}_{3-\delta}$ , ( $0 \leq x \leq 0.15$ ) at 200°C to 800°C.....	57
<b>4.14</b> Thermal expansion curves of $(\text{Ba}_{0.5}\text{Sr}_{0.5})_{0.8}\text{La}_{0.2-x}\text{Ca}_x\text{Co}_{0.8}\text{Fe}_{0.2}\text{O}_{3-\delta}$ ( $0 \leq x \leq 0.15$ ) at 50°C to 800°C.....	59
<b>4.15</b> XRD patterns of $(\text{Ba}_{0.5}\text{Sr}_{0.5})_{0.8}\text{La}_{0.2}\text{Co}_{0.8}\text{Fe}_{0.2}\text{Ca}_x\text{O}_{3-\delta}$ , ( $0 \leq x \leq 0.05$ ) powder after calcined at 1000°C for 5 hours.....	60
<b>4.16</b> XRD patterns of $(\text{Ba}_{0.5}\text{Sr}_{0.5})_{0.8}\text{La}_{0.2}\text{Co}_{0.8}\text{Fe}_{0.2}\text{Ca}_x\text{O}_{3-\delta}$ and $(\text{Ba}_{0.5}\text{Sr}_{0.5})_{0.8}\text{La}_{0.2}\text{Co}_{0.8}\text{Fe}_{0.2}\text{Ca}_{0.01}\text{O}_{3-\delta}$ , disc after sintered at 1100°C for 10 hours.....	61
<b>4.17</b> SEM micrographs of $(\text{Ba}_{0.5}\text{Sr}_{0.5})_{0.8}\text{La}_{0.2}\text{Co}_{0.8}\text{Fe}_{0.2}\text{Ca}_x\text{O}_{3-\delta}$ , ( $x=0$ and $0.01$ ) after sintered at 1100°C for 10 hours.....	62
<b>4.18</b> Surface morphology (a) and Ca-mapping of $(\text{Ba}_{0.5}\text{Sr}_{0.5})_{0.8}\text{La}_{0.2-x}\text{Ca}_x\text{Co}_{0.8}\text{Fe}_{0.2}\text{O}_{3-\delta}$ disc, $x=0.01$ (b).....	63
<b>4.19</b> The electrical conductivity of $(\text{Ba}_{0.5}\text{Sr}_{0.5})_{0.8}\text{La}_{0.2}\text{Co}_{0.8}\text{Fe}_{0.2}\text{Ca}_x\text{O}_{3-\delta}$ , ( $x = 0$ and $0.01$ ) at 300°C to 750°C.....	64
<b>4.20</b> Oxygen temperature programmed desorption curves of $(\text{Ba}_{0.5}\text{Sr}_{0.5})_{0.8}\text{La}_{0.2}\text{Co}_{0.8}\text{Fe}_{0.2}\text{Ca}_x\text{O}_{3-\delta}$ , ( $x= 0$ and $0.01$ ) at 200°C to 800°C.....	66
<b>4.21</b> Thermal expansion curves of $(\text{Ba}_{0.5}\text{Sr}_{0.5})_{0.8}\text{La}_{0.2}\text{Co}_{0.8}\text{Fe}_{0.2}\text{Ca}_x\text{O}_{3-\delta}$ , ( $x= 0$ and $0.01$ ) at 50°C to 800°C.....	67
<b>4.22</b> XRD patterns of $\text{Ba}_{0.5}\text{Sr}_{0.5}\text{Co}_{0.8}\text{Fe}_{0.2}\text{Cu}_x\text{O}_{3-\delta}$ , ( $0 \leq x \leq 0.2$ ) powder after calcined at 900°C for 5 hours.....	69

<b>Figure</b>	<b>Page</b>
<b>4.23</b> XRD patterns of $\text{Ba}_{0.5}\text{Sr}_{0.5}\text{Co}_{0.8}\text{Fe}_{0.2}\text{Cu}_x\text{O}_{3-\delta}$ , ( $0 \leq x \leq 0.2$ ) discs after sintered at $1000^\circ\text{C}$ for 10 hours.....	69
<b>4.24</b> SEM micrographs of $\text{Ba}_{0.5}\text{Sr}_{0.5}\text{Co}_{0.8}\text{Fe}_{0.2}\text{Cu}_x\text{O}_{3-\delta}$ , ( $0 \leq x \leq 0.2$ ) after sintered at $1000^\circ\text{C}$ for 10 hours.....	71
<b>4.25</b> Surface morphology (a) and Cu-mapping of $\text{Ba}_{0.5}\text{Sr}_{0.5}\text{Co}_{0.8}\text{Fe}_{0.2}\text{Cu}_x\text{O}_{3-\delta}$ disc (b).....	72
<b>4.26</b> The electrical conductivity of $\text{Ba}_{0.5}\text{Sr}_{0.5}\text{Co}_{0.8}\text{Fe}_{0.2}\text{Cu}_x\text{O}_{3-\delta}$ , ( $0 \leq x \leq 0.2$ ) at $300^\circ\text{C}$ to $750^\circ\text{C}$ .....	74
<b>4.27</b> Oxygen temperature programmed desorption curves of $(\text{Ba}_{0.5}\text{Sr}_{0.5})_{0.8}$ $\text{Co}_{0.8}\text{Fe}_{0.2}\text{Cu}_x\text{O}_{3-\delta}$ , ( $0 \leq x \leq 0.2$ ) at $200^\circ\text{C}$ to $800^\circ\text{C}$ .....	75
<b>4.28</b> Thermal expansion curves of $\text{Ba}_{0.5}\text{Sr}_{0.5}\text{Co}_{0.8}\text{Fe}_{0.2}\text{Cu}_x\text{O}_{3-\delta}$ , ( $0 \leq x \leq 0.2$ ) at $50^\circ\text{C}$ to $800^\circ\text{C}$ .....	77
<b>4.29</b> XRD patterns of $\text{Ba}_{0.5}\text{Sr}_{0.5}\text{Co}_{0.8}\text{Fe}_{0.2}\text{Zn}_x\text{O}_{3-\delta}$ , ( $0 \leq x \leq 0.2$ ) powder after calcined at $1000^\circ\text{C}$ for 5 hours.....	78
<b>4.30</b> XRD patterns of $\text{Ba}_{0.5}\text{Sr}_{0.5}\text{Co}_{0.8}\text{Fe}_{0.2}\text{Zn}_x\text{O}_{3-\delta}$ , ( $0 \leq x \leq 0.2$ ) membrane after sintered at $1100^\circ\text{C}$ for 10 hours.....	79
<b>4.31</b> SEM micrographs of $\text{Ba}_{0.5}\text{Sr}_{0.5}\text{Co}_{0.8}\text{Fe}_{0.2}\text{Zn}_x\text{O}_{3-\delta}$ , ( $0 \leq x \leq 0.2$ ) after sintered at $1100^\circ\text{C}$ for 10 hours.....	81
<b>4.32</b> Surface morphology (a) and Zn-mapping of $\text{Ba}_{0.5}\text{Sr}_{0.5}\text{Co}_{0.8}\text{Fe}_{0.2}\text{Zn}_x\text{O}_{3-\delta}$ , disc (b).....	82
<b>4.33</b> The electrical conductivity of $\text{Ba}_{0.5}\text{Sr}_{0.5}\text{Co}_{0.8}\text{Fe}_{0.2}\text{Zn}_x\text{O}_{3-\delta}$ , ( $0 \leq x \leq 0.2$ ) at $300^\circ\text{C}$ to $750^\circ\text{C}$ .....	84
<b>4.34</b> Oxygen temperature programmed desorption curves of $(\text{Ba}_{0.5}\text{Sr}_{0.5})_{0.8}$ $\text{Co}_{0.8}\text{Fe}_{0.2}\text{Zn}_x\text{O}_{3-\delta}$ , ( $0 \leq x \leq 0.2$ ) at $200^\circ\text{C}$ to $800^\circ\text{C}$ .....	85
<b>4.35</b> Thermal expansion curves of $\text{Ba}_{0.5}\text{Sr}_{0.5}\text{Co}_{0.8}\text{Fe}_{0.2}\text{Zn}_x\text{O}_{3-\delta}$ , ( $0 \leq x \leq 0.2$ ) measured at $50^\circ\text{C}$ to $800^\circ\text{C}$ .....	87



## LIST OF ABBREVIATIONS

SOFC	Solid Oxide Fuel Cell
MIEC	Mixed Ionic Electronic Conductor
EDTA	Ethylene Diamine Tetraacetic Acid
XRD	X-ray diffractometer
SEM	Scanning electron microscopy
EDX	Energy Dispersive X-ray spectroscopy
TEC	Thermal expansion coefficient
TPD	Temperature program desorption
R	Electrical resistance
V	Voltage
g	gram (s)
%	percent
°C	degree celsius
$a$	cubic unit lattice parameter
$r$	ionic radius
$t$	tolerance factor
$\sigma$	specific conductivity
$\mu\text{m}$	micrometer
$k$	temperature constant
Å	angstrom
nm	nanometer
$\delta$	oxygen non-stoichiometry
ml	milliliter
$\rho$	specific resistance
A	area
l	length
I	electrical current

# CHAPTER I

## INTRODUCTION

Nowaday, many people are seeking for a new energy in order to compensate the energy from petroleum that is rising to high cost, emits pollutants to environment, causes global warming and becomes scarcity in the future. Since the requirement for the industrial energy is the system which can produce the continuous energy, solid oxide fuel cell (SOFC) is the forefront type of candidates. The reasons are a good performance in producing energy, friendly production for environment and producing the continuous energy as long as feeding of fuel. In the past years, it has been an interesting in perovskite oxide which can be used as the electrode in SOFC because it has the mix ionic-electronic conductivity as appropriate properties of the cathode in SOFC. BaSrCoFeO<sub>3</sub> (BSCF) has been continuously developed because it not only has low price but also allows oxygen gas passing through the bulk of material. However, low electrical conductivity of material around 50 S·cm<sup>-1</sup> is disadvantage and its operation at high temperature also causes the structure problem. Thus, this research is focusing on the development of electrical conductivity and other properties of BSCF material in order to be used as the cathode material in SOFC.

### 1.1 Fuel Cell

Fuel cells are the promising next generation energy conversion systems because of its potentials in high power generation efficiency, silent operation and extremely low pollutant emissions. Fuel cell is an electrochemical device that allows the direct conversion of chemical energy to electrical energy. Every fuel cells consist of cathode, anode and electrolyte which carries electrically charged particle from one electrode to the other electrode.

The types and sizes of fuel cells are classified by the efficiency and the working electrolyte. In present, the main electrolytes are alkali, molten carbonate, phosphoric acid, proton exchange membrane and solid oxide. The first three types are liquid electrolytes and the last two types are solid electrolytes. Fuel cell can also be divided into two groups: low temperature fuel cell and high temperature fuel cell. The first one operates approximately 200°C and the second one operates at temperature above 500°C. The summary of several kinds of fuel cells is shown in Table 1.1

## **1.2 Solid oxide fuel cell**

Solid oxide fuel cell (SOFC) is the most efficient devices that converts the chemical fuel and oxidant gas directly into electrical power by electrochemical reaction. The efficiency of the system is about 45-70% and the high operating temperature is around 600-1000°C. A significant reduction of operating temperature from traditional 1000°C to intermediate temperature range of 600 to 800°C greatly improves the long-term stability of the solid oxide materials. Comparing SOFCs with other kinds of fuel cells, the advantage is the fuel flexibility, that offers the utilization of hydrocarbons and other renewable fuels. However, the high temperature operation is the limitation of SOFC which affects the stability of cells.

Solid oxide fuel cell is intended mainly for stationary application with an output from 1 kW to 10 MW. The effective efficiency can be reached as high as 70% in the hybrid systems called combined heat and power (CHP) device. Due to the high operating temperature of SOFC, there is no need for expensive catalyst requirement (platinum). This means that SOFCs do not get poisoned by carbon monoxide and they are highly fuel-flexible in use. This system consists of four main components: an electrolyte, a porous anode, a porous cathode, and the interconnect.

**Table 1.1** Type of fuel cells [1]

<b>Fuel Cell Name</b>	<b>Electrolyte</b>	<b>Qualified Power (W)</b>	<b>Working Temperature (°C)</b>	<b>Electrical efficiency</b>
Alkaline fuel cell	Aqueous alkaline solution (e.g., potassium hydroxide)	10 - 100 kW	under 80	Cell: 60–70% System: 62%
Direct methanol fuel cell (DMEC)	Polymer membrane (ionomer)	100 kW-1 MW	90–120	Cell: 20–30% System: 10–20%
Proton exchange membrane fuel cell (PEMFC)	Polymer membrane (ionomer) (e.g., Nafion® or Polybenzimidazole fiber)	100W – 500 kW	Nafion 70–120 PBI 125–220	Cell: 50–70% System: 30–50%
Phosphoric acid fuel cell (PAFC)	Molten phosphoric acid (H <sub>3</sub> PO <sub>4</sub> )	up to 10 MW	150-200	Cell: 55% System: 40%
Molten carbonate fuel cell (MCFC)	Molten alkaline carbonate (e.g., sodium bicarbonate NaHCO <sub>3</sub> )	100 MW	600-650	Cell: 55% System: 47%
Solid oxide fuel cell (SOFC)	O <sup>2-</sup> -conducting ceramic oxide (e.g., zirconium dioxide, ZrO <sub>2</sub> )	up to 100 MW	700–1000	Cell: 60–70% System: 55–60%

### **1.2.1 Electrolyte for SOFC**

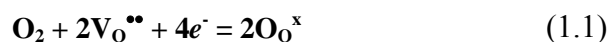
The electrolyte for solid oxide fuel cell is generally oxygen ion conductors. It must be stable in both reducing and oxidizing environment, and must have sufficiently high ionic conductivity and low electronic conductivity. The current flow occurs by the movement of oxygen ions through the crystal lattice by a thermally activated hopping of oxygen ion from one crystal lattice to its neighbor site. To achieve the movement, the crystal needs to contain unoccupied site for oxygen ion from the neighbouring site to migrate into the lattice of oxygen ion. The energy involved in the process of migration is small, certainly less than about 1 eV. The materials used for making the electrolyte must be thin and strong film especially without the gas leakage. In addition, they must have thermal expansion compatible with electrodes and other construction of materials, be suitable mechanical properties, be negligible volatilization of components and negligible interaction with electrode materials under operation and fabrication conduction. In present, there are many electrolytes in SOFC but zirconia is the most favorable electrolyte at temperature above 800°C, for example YSZ and ScSZ. In addition, ceria electrolyte is also attractive for low temperature (400-600°C) SOFCs, e.g. Gadolinium doped Ceria (GDC) and Samarium doped Ceria (SDC).

### **1.2.2 Anode for SOFC**

Normally, anode is the porous material and has the function to promote the electrochemical oxidation of fuels such as hydrogen or methane. The catalytic properties of the anode are necessary for the kinetics of fuel oxidation after the oxide ions pass through the solid electrolyte. The chemical and electrochemical reactions often take place preferentially at certain surface and interfacial sites or triple-phase boundaries (TPBs). The general requirement for anode to use in SOFC includes good chemical and thermal stability during cell fabrication and operation, high electronic conductivity under operating conditions, high catalytic activity on the oxidation of fuels, suitable thermal expansion coefficient with adjacent cell components.

### 1.2.3 Cathode for SOFC

Cathode material for solid oxide fuel cell should be porous for rapid mass transport of the reactant. Therefore it needs to have many properties including high electrical conductivity, high catalytic activity for oxygen reduction and compatibility with other cell components. In solid oxide fuel cell, the cathode is the material where pure oxygen or oxygen from air is reduced through the following electrochemical reaction.

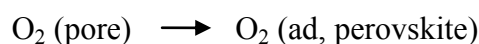


Where,  $\text{V}_\text{O}^{\bullet\bullet}$  is a vacant oxygen site, and  $\text{O}_\text{O}^x$  is oxygen ion on a regular oxygen site in the YSZ lattice. Above equation illustrates that the oxygen reduction process requires the presence of oxygen and electrons for generating oxide ions to be transported away from the reaction site into the bulk of the electrolyte. The reaction is occurred at the triple-phase boundaries (TPBs) between the electrode, electrolyte and oxidant gas. However, if the cathode materials have mix electronic and ionic conductivity, oxygen species may be transported through the bulk of electrode, so the reaction site could be extended. For mix electronic and ionic conducting cathode the oxygen reaction occurs as following mechanism:

1. Diffusion of  $\text{O}_2$  into the pore of the cathode



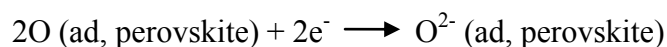
2. Adsorption of  $\text{O}_2$  onto the cathode surface



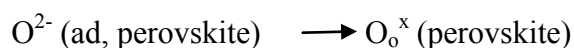
3. Dissociation of molecular adsorbed O



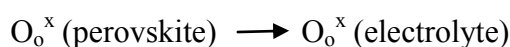
4. Charge-transfer process of O atom on cathode surface



5. Transfer process of  $\text{O}^{2-}$  from cathode surface to the bulk



6.  $\text{O}^{2-}$  transfer into the electrolyte



Moreover, under the certain condition the electronic conductivity may be induced the surface of electrolyte close to the TPB, which will also expand the reaction zone around the TPB, leading to the increase in energy of this system. In the earliest stages platinum was used as cathode since the other material were not available. However, platinum is expensive and it uses in commercial SOFC for power generation. Thus, the future needs to seek for a new material such as perovskite-type ( $\text{ABO}_3$ ) complex oxide which has sufficient superior mixed electronic-ionic conducting properties. That promising candidate material can be used as the cathode in solid oxide fuel cell in order to replace the high cost material.

#### 1.2.4 Interconnect

The position of the interconnect sites is between each of individual cell and has to carry electrical current from the electrochemical cell to the external circuit, therefore this material must have a good electrical conductivity. Both of ceramic and metallic materials can be used as the interconnect for SOFC. It should have chemically and mechanically stable for operating at high temperature for a longer period of time. Because interconnect is exposed to both oxidizing and reducing condition, this materials should not change property in any either temperature or oxygen partial pressure. In addition, the thermal expansion must be matched with the expansion of other fuel cell components. Ceramic interconnects usually made from semiconducting oxides, which have good stability in air and compatible with other

ceramic fuel cell components. Most metals have an excellent in electrical conductors, low cost and good fabrication thus the metallic interconnects are more widely used than ceramic interconnect.

### 1.3 Perovskite oxide

Perovskite oxide is the inorganic compound which can be used as the cathode in SOFC because it has required properties especially mix ionic and electronic conductivity. Normally, there are many kinds of perovskites such as perovskite oxide, carbide, halide and hydride. In nature, perovskite oxide in form of  $ABO_3$  as calcium titanium oxide ( $CaTiO_3$ ) was discovered in the Ural mountains of Russia by G. Rose in 1839 and named for Russian mineralogist, L. A. Perovskite (1792-1856). In 1969,  $LaCoO_3$  was tested by Tedmon et al. [2] for its initial performance in cells. However, severe degradation occurred with increasing the operation time because the reaction with YSZ electrolyte was observed. Then the trend was moved toward lanthanum manganite ( $LaMnO_3$ )-based materials [3]. Although the degradation not observed on  $LaMnO_3$ , it had some partial reactions with YSZ electrolyte. For intermediate temperature SOFC, a composite of cathode materials of Sr-doped  $LaMnO_3$  showed good performance [4] and  $LaSrCoFeO_3$  (LSCF) was developed [5] for using with ceria-based electrolyte. Then Wang et al. [6] found that LSCF 6482 membrane sintered at 1623 K 8 hrs. showed a fibroid structure that may provide high mechanical strength whereas membranes sintered at lower temperatures showed no such morphology. Since the thermal expansion coefficient (TEC) of LSCF is quite different from YSZ, the substitution of Ba in La site is useful for improving thermal property of material. Richer et al [7] found that BSCF showed low values of the critical radius and was a good oxygen ion conductor compared with other perovskites. Shao et al. [8] announced that  $Ba_{0.8}Sr_{0.2}Co_{0.8}Fe_{0.2}O_{3-\delta}$  could be used as the cathode for solid oxide fuel cell. Recently Zhou et al [9] proved that the optimum stoichiometry of BSCF is 5582 giving the highest electrical conductivity (about  $50 \text{ S}\cdot\text{cm}^{-1}$ ) when compared with A-site excess of BSCF. The substitution of another ion at A-site and B-site of BSCF could improve the physical properties and conductivity of primitive BSCF. This phenomenon was presented from the changing of microstructure to maintain a cubic



structure and valence state of B-site cation and the releasing of oxygen ion in the structure of BSCF to maintain the charge neutrality.

#### 1.4 Literature reviews

Shuyan et al. [10] studied the effect of La ion doped in A-site of  $\text{Ba}_{0.5}\text{Sr}_{0.5}\text{Co}_{0.8}\text{Fe}_{0.2}\text{O}_{3-\delta}$ . The result showed the cubic structure of BSCF after doped with 20 mol% of La ion and the electrical conductivity was increased from about  $50 \text{ S}\cdot\text{cm}^{-1}$  to  $376 \text{ S}\cdot\text{cm}^{-1}$  at  $392^\circ\text{C}$ . It may be resulted from the increase in concentration of charge carrier which was induced by La doping. However, the thermal expansion behavior of  $(\text{Ba}_{0.5}\text{Sr}_{0.5})_{1-x}\text{La}_x\text{Co}_{0.8}\text{Fe}_{0.2}\text{O}_{3-\delta}$  (BSLFCF) showed abnormal expansion at high temperature due to the losing lattice oxygen followed by the reduction of  $\text{Co}^{4+}$  and  $\text{Fe}^{4+}$ .

Tai et al. [11] explained the lattice expansion with the formation of oxygen vacancies in  $\text{La}_{0.8}\text{Sr}_{0.2}\text{Co}_{1-y}\text{Fe}_y\text{O}_3$ . The repulsion force arises between those mutually exposed cations when oxygen ions are extracted from the lattice. The increase in cation size due to the reduction of cobalt and iron ions from higher valences to lower valences, occur concurrently with the creation of oxygen vacancies in order to maintain electrical neutrality.

Tai et al. [12] studied the structure and electrical conductivity of  $\text{La}_{0.8}\text{Sr}_{0.2}\text{Co}_{1-y}\text{Fe}_y\text{O}_3$ , and investigated that the electrical conductivity of each component was decreased with increasing Fe content. Moreover, the maximum electrical conductivity peak shifted from around  $200^\circ\text{C}$  to  $920^\circ\text{C}$  after increasing the Fe content from  $y = 0$  to  $y = 0.7$ . The explanation for thermal expansion of materials may be concerned with thermal reduction of  $\text{Fe}^{4+}$ ,  $\text{Co}^{4+}$  and  $\text{Co}^{3+}$  to the lower valence states which contributed to promote the ionized oxygen vacancies. The most of oxygen vacancies led to the expansion on material when it was heated. In addition Baumann et al. 2006 [13], demonstrated that the surface exchange rate of BSCF cathode reached to  $5 \times 10^{-5} \text{ cm s}^{-1}$  at  $750^\circ\text{C}$  in air which was faster than LSCF of 100 times under the identical condition.

In 1998, Rim et al. [14] focused on characteristics of  $\text{Pr}_{1-x}\text{M}_x\text{MnO}_3$  ( $\text{M} = \text{Ca}$  and  $\text{Sr}$ ) as a cathode material in SOFC, basing on its electrical conductivity, cathodic polarization, thermal expansion coefficient, particle size distribution, reactivity with electrolyte. The dopants were varied in the range of 0, 10, 30, 50 and 70 mol% respectively. The optimum content of doping Ca and Sr was 30 mol%. The Ca doped  $\text{PrMnO}_3$  showed the better characteristic property than Sr doped in point of higher electrical conductivity, lower cathodic overpotential, non-reactivity and similar in thermal expansion coefficient with YSZ electrolyte.

In 2000, Mori et al. [15] studied on fabrication condition of dense sintered  $\text{La}_{0.6}\text{AEMnO}_3$  perovskite when  $\text{AE} = \text{Ca}$  and  $\text{Sr}$  40 mol%. After calcined at  $1100^\circ\text{C}$  for 1 hour the perovskite oxide powder showed the single phase. The higher density could be obtained after sintering at higher temperature and the best density of specimen reached more than 95% after  $\text{LaCaMnO}_3$  was sintered at  $1500^\circ\text{C}$  for 1 hour. This result indicated that doping of  $\text{Ca}^{2+}$  in A-site of  $\text{LaAEMnO}_3$  gave better property than doping  $\text{Sr}^{2+}$  in densification. Moreover, the shrinkage of specimens was observed. Sr-doped lanthanum manganites had a tendency to decrease shrinkage with increasing Sr substitution. On the other hand, the shrinkage of the Ca-doped lanthanum manganites decreased with increasing Ca content up to 30 mol%.

In 2003, Tan et al. [16] considered the influence of sintering condition on the crystal structure, microstructure and oxygen permeability of perovskite-related type  $\text{Ba}_{0.8}\text{Sr}_{0.2}\text{Co}_{0.8}\text{Fe}_{0.2}\text{O}_{3-\delta}$  membrane. The result showed that the dwell time and sintering temperature have influence on the microstructure of membrane. However, the oxygen permeation was not related with density.

In 2004, Shou et al. [17] was looking for a high performance cathode for the next generation of solid oxide fuel cell and the material which can reduce the operation temperature of SOFC to intermediate temperature ( $500\text{-}700^\circ\text{C}$ ). It was found that BSCF doped with ceria exhibited high power densities up to  $1010 \text{ mW cm}^{-2}$  at  $600^\circ\text{C}$  when operated in hydrogen fuel. Moreover, it also showed a lowest polarization resistant which benefits for transferring electron within the bulk of the electrode, leading to the increasing rate of the process.

Yamazoe et al. [18] reported the first oxygen TPD results from perovskites. The objective was to study the influence of partial substitution of  $\text{La}^{3+}$  by  $\text{Sr}^{2+}$  in  $\text{La}_{1-x}\text{Sr}_x\text{CoO}_3$  oxides on their surface and catalytic properties. Oxygen TPD peaks from perovskites appeared two oxygen desorption peaks after adsorption on  $\text{La}_{1-x}\text{Sr}_x\text{CoO}_3$  at 1023 K. The low-temperature peak ( $\alpha$ -type) was attributed to adsorbed oxygen, whereas the high-temperature peak ( $\beta$ -type) was ascribed to lattice oxygen. They also concluded that the amount of desorbed oxygen from  $\text{La}_{1-x}\text{Sr}_x\text{CoO}_3$  increased with increasing x-substitution. The A-site substitution with a divalent ion is well known to stimulate the formation of oxygen vacancies which benefits for ionic conduction.

In 2006, Wei B. et al. [19] examined the crystal structure, thermal expansion and electrical conductivity of  $\text{Ba}_x\text{Sr}_{1-x}\text{Co}_{0.8}\text{Fe}_{0.2}\text{O}_{3-\delta}$ . It was indicated that the cubic perovskite structure would be obtained when Ba content was  $\leq 0.6$  and the lattice parameter increased according to the Ba contents. However, the thermal expansion and electrical conductivity of specimen decreased following the increasing of Ba ion.

In the same year Wang C. et al. [20] studied the effect of Ca doping on the electrochemical properties of  $\text{LiNi}_{0.8}\text{Co}_{0.2}\text{O}_2$  cathode material. The powders of  $\text{LiNi}_{0.8}\text{Co}_{0.2}\text{O}_2$  and Ca doped  $\text{LiNi}_{0.8}\text{Co}_{0.2}\text{O}_2$  were prepared by rheological phase reaction method. It demonstrated that the Ca doping materials significantly improved the reversible capacity, cycling performance, thermal stability and rate capability. After doped with Ca, the particles were smooth and rock-shaped. Moreover, the Ca doped  $\text{LiNi}_{0.8}\text{Co}_{0.2}\text{O}_2$  induced smaller particle size and showed the lower particle size distribution in materials.

Guo L. [21] studied the effect of cation substitution in A-site of  $\text{La}(\text{AE})\text{CrO}_3$  (AE=Mg, Ca, Sr). The result revealed that the substitution of 15 mol% Ca ion showed the highest relative density and the lower thermal expansion when compared with the Sr ion substitution at the equivalent quantity.

Sun et al. [22] studied the effect of Ca doping on the electrochemical properties of  $\text{LiNi}_{0.8}\text{Co}_{0.2}\text{O}_2$  cathode material. The result showed that the optimum Ca content was 20 mol% and the material presented low particle size distribution.

Moreover, the performance of cell could be increased after doped with Ca 20 mol% and this cell could be operated for a long time.

In 2007, Su et al. [23] studied the substitution of La (5 to 20 mol%) in the structure of BSCF 5582 synthesized by citrate-EDTA. It was showed that the thermal expansion and electrical conductivity were increased with to the increasing of La ion content. Moreover, the doping of La ion had the lower resistant than BSCF around 34%.

In 2007 Ngampeunpis W., [24] studied the substitution of the Zn and Cu ions at B-site of  $\text{Ba}_{0.5}\text{Sr}_{0.5}\text{Co}_{0.8}\text{Fe}_{0.2}\text{O}_3$  (BSCF5582). It was indicated that the increasing of substitution of Zn and Cu ions in the position of Co and Fe at B-site of BSCF led to reduce the electrical conductivity of BSCF5582. However, the oxygen permeation of specimen was increased with substitution content of Zn and Cu.

Recently, Rajendran D.N. et al. [25] studied ionic conductivity of  $\text{NaAZrMO}_6$  (A = Ca or Sr; M = Nb or Ta). The orthorhombic structure (Pnma) was present after doping Ca ion in A-site of  $\text{NaAZrMO}_6$ . The doping of Sr ion would obtain the cubic perovskite structure (Pm3m). The conductivity was measured in the temperature range of 300 to 750°C in air, nitrogen and pure dry oxygen atmosphere. The electrical conductivity increased linearly with rising temperature and nearly the same in all three atmospheres at 600-750°C. When compared the substitutions of Ca and Sr ions, it was found that the higher conductivity was obtained in nitrogen atmosphere after doping Ca ions.

From the previous researches, it has been found the substitution of Ca ion in the other perovskite structures improved the properties of materials, but it has not been reported in the BSCF5582 perovskite structure. Thus, in this research we would like to focus on the substitution of Ca in A-site and the substitution of Ca and La ions in A-site of BSCF5582, basing on the assumption that Ca ions and La ions can improve the electrical conductivity of BSCF perovskite oxide. Moreover, the studies on the excess addition of cations such as Ca, Cu and Zn ions in BSCF5582 is also investigated since the previous research report, the excess addition of metal ion in the structure could increase the oxygen permeation in the perovskite materials.

## 1.5 The objectives of the thesis

**1.5.1 To synthesize the  $ABO_3$  perovskite structure by modified citrate method as below:**

**Substitution of Ca and La in A-site of BSCF**

- $(Ba_{0.5}Sr_{0.5})_{1-x}Ca_xCo_{0.8}Fe_{0.2}O_{3-\delta}$ , ( $x = 0 - 0.5$ )
- $(Ba_{0.5}Sr_{0.5})_{0.8}La_{0.2-x}Ca_xCo_{0.8}Fe_{0.2}O_{3-\delta}$ , ( $x = 0.05 - 0.15$ )

**The addition of Ca, Cu and Zn in BSCF**

- $(Ba_{0.5}Sr_{0.5})_{0.8}La_{0.2}Ca_xCo_{0.8}Fe_{0.2}O_{3-\delta}$  ( $x = 0.01 - 0.05$ )
- $Ba_{0.5}Sr_{0.5}Co_{0.8}Fe_{0.2}(Cu, Zn)_xO_{3-\delta}$  ( $x = 0.05 - 0.2$ )

**1.5.2 To prepare perovskite disc and characterize the structure by XRD and surface morphology by SEM.**

**1.5.3 To measure the thermal expansion properties, electrical properties and oxygen desorption ( $O_2$ -TPO) of all perovskites membranes as below:**

- $(Ba_{0.5}Sr_{0.5})_{1-x}Ca_xCo_{0.8}Fe_{0.2}O_{3-\delta}$ , ( $x = 0 - 0.5$ )
- $(Ba_{0.5}Sr_{0.5})_{0.8}La_{0.2-x}Ca_xCo_{0.8}Fe_{0.2}O_{3-\delta}$ , ( $x = 0.05 - 0.15$ )
- $(Ba_{0.5}Sr_{0.5})_{0.8}La_{0.2}Ca_xCo_{0.8}Fe_{0.2}O_{3-\delta}$  ( $x = 0.01 - 0.05$ )
- $Ba_{0.5}Sr_{0.5}Co_{0.8}Fe_{0.2}(Cu, Zn)_xO_{3-\delta}$  ( $x = 0.05 - 0.2$ )

## CHAPTER II

### THEORY

#### 2.1 Fuel cell

Fuel cell is an electrochemical device which directly converts the fuel into to electrical energy. When oxygen enters the cathode and combines with electrons from the input electrical circuit, the hydrogen are supplied at the anode site and hydrogen ion will diffuse through the electrolyte. Then, the chemical reaction occurs to generate electrons which are the electrical energy of this system and releases only water from the cell. The fuel cell can continuously churn out the electricity as long as raw material is supplied. This is the key difference between fuel cell and battery. The electrochemical reactions of fuel cells are shown in Table 2.1.

**Table 2.1** Electrochemical reactions in fuel cell systems [26]

Type of Fuel Cell	Anode Reaction	Cathode Reaction
<b>PEMFC</b>	$H_2 \rightarrow 2H^+ + 2e^-$	$\frac{1}{2}O_2 + 2H^+ + 2e^- \rightarrow H_2O$
<b>AFC</b>	$H_2 + 2(OH)^- \rightarrow 2H_2O + 2e^-$	$O_2 + 2H_2O + 4e^- \rightarrow 4OH^-$
<b>PAFC</b>	$H_2 \rightarrow 2H^+ + 2e^-$	$O_2(g) + 4 H^+ + 4e^- \rightarrow 2 H_2O$
<b>MCFC</b>	$H_2 + CO_3^{2-} \rightarrow H_2O + CO_2 + 2e^-$ $CO + CO_3^{2-} \rightarrow 2CO_2 + 2e^-$	$CO_2 + \frac{1}{2}O_2 + 2e^- \rightarrow CO_3^{2-}$ $O_2 + CO_2 + 2e^- \rightarrow CO_3^{2-}$
<b>SOFC</b>	$H_2 + O^{2-} \rightarrow 2H_2O + 2e^-$ $CO + O^{2-} \rightarrow CO_2 + 2e^-$ $CH_4 + 4O^{2-} \rightarrow 2H_2O + CO_2 + 8e^-$	$O_2 + 4e^- \rightarrow 2 O^{2-}$

## 2.2 Solid oxide fuel cell

The SOFC system consists of four main components as described in section 1. The operating of SOFC is illustrated in the Figure 2.1. Firstly, the porous cathode material allows the oxygen atoms from oxygen or air to be reduced at the cathode/electrolyte interface and being converted into oxygen ions by electrons from the electrical input current. Secondly, solid oxide electrolyte such as yttria-stabilised zirconia (YSZ), permits only the oxygen ions to migrate to the anode side. Thirdly, at the porous anode material where the fuel is supplied, oxide ion reacts with fuel such as hydrogen at the anode/electrolyte interface, giving off water, heat, and most importantly electrons to the external circuit. If carbon-containing fuels are involved, CO<sub>2</sub> gas will be produced. Finally, the interconnect which requires two interconnect wires to induce the current to go out of the system and to allow the electrons coming back to the cathode again in order to provide a source of useful electrical energy in an external circuit. These four parts are oftenly combined into a single material, which makes contact with others by the cathode on one side and the anode on the other side.

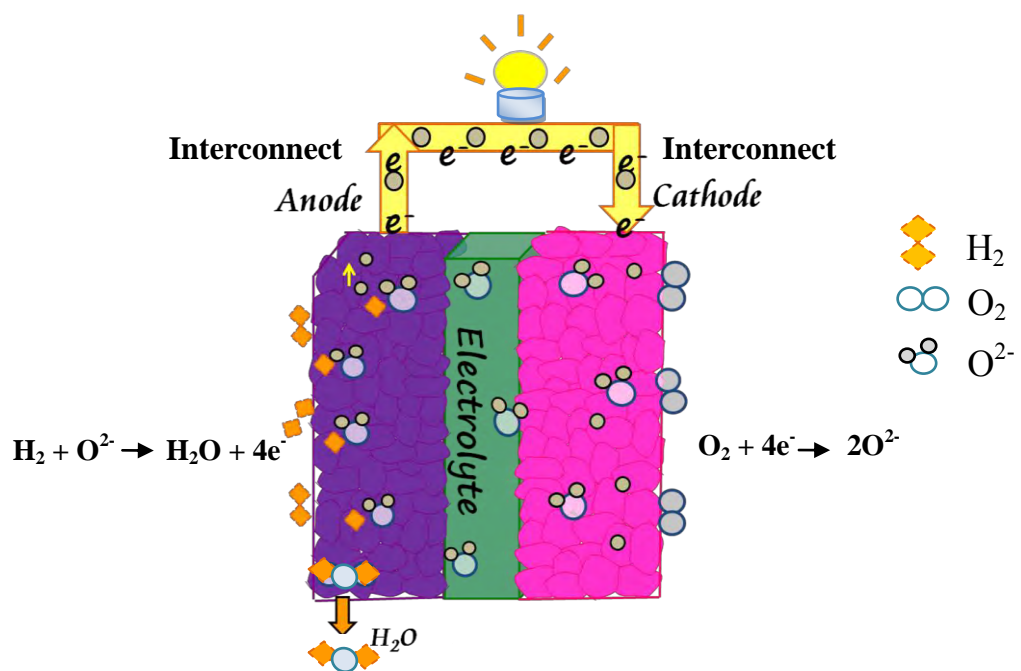


**Figure 2.1** A planar design of SOFC.

## 2.3 Perovskite oxide

### 2.3.1 Crystal structure of perovskite oxide [27]

The crystal structure of perovskite oxide has a general formula  $ABO_3$  with primitive cube. The lattice structure of perovskite  $ABO_3$  is shown in Figure 2.2. This oxide consists of three elemental ions, namely of the large ion is A site cation,  $A^{n+}$ , the small ion is B site cation,  $B^{(6-n)+}$  and the oxide anion,  $O^{2-}$  where n is the positive charge on the cation. A-site cations can be rare earth, alkaline earth or alkali ions and are coordinated with twelve oxide ions in the dodecahedral site of the framework. The B site cation can mostly be the transition metal ions and are surrounded by six oxide ions which occupy the octahedral site. However, in the recent work, Muller and Roy [28] proved that the ideal cubic perovskite structure does not occur as the  $A^{3+}B^{3+}O_3$  at room temperature but it does occur for the  $A^{2+}B^{4+}O_3$  and  $A^{1+}B^{5+}O_3$ .

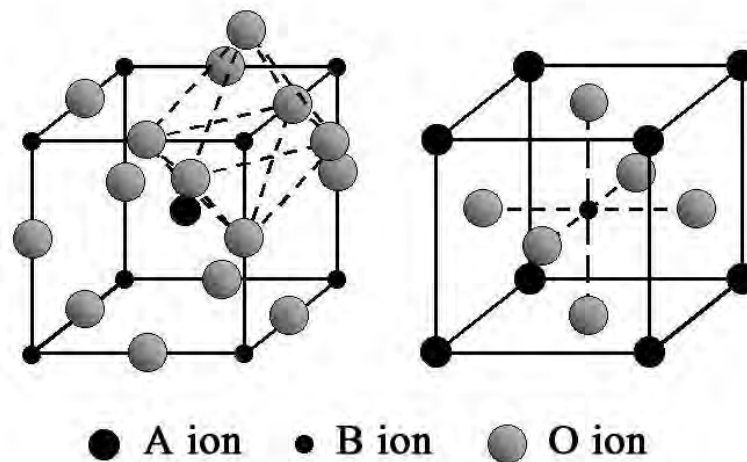


**Figure 2.2** Lattice structure of  $ABO_3$  perovskite.

Figure 2.2 represents the sharing of octahedron at the corner to form the skeleton of the  $ABO_3$  perovskite structure, in which the center position is occupied by the A cation. Furthermore, this structure can be viewed with the B cation placed in the center of the octahedron and the A cation is in the center of the cube.



The geometrical fitting of cations and anions of perovskite structure is measured by the Goldschmidt tolerance factor defined as follows:

$$t = \frac{(r_A + r_O)}{\sqrt{2}(r_B + r_O)} \quad (2.1)$$

where  $r_A$ ,  $r_B$  and  $r_O$  are the effective ionic radii of A, B and O ions, respectively. Usually, tolerance factor is evaluated from Shannon's ionic radii [29] for respective coordination numbers. When the tolerance factor of perovskite is nearly unity at high temperature, the structure is ideal cubic. However, the perovskite structure is mostly stable in the range of  $0.75 < t < 1.0$ , and becomes cubic in the range of  $t > 0.95$ . If this factor is not in  $0.75 < t < 1.0$ , orthorhombic or rhombohedral distortions can be occurred. Even in the range of  $t = 0.8-0.9$  which is the most favourable value for perovskites, deviations from the ideal structure are well known as orthorhombic, rhombohedral, tetragonal, monoclinic and triclinic symmetry. The distorted structure may exist at the normality but it transforms to the cubic structure at ambient temperature.

For the ideal perovskite structure, the size and coordination preferences of three or more ions need to be satisfied simultaneously by the structure. Nevertheless, it is rarely possible that all these can be accommodated perfectly structure. The relationship between the radii of the various ions in the perovskite structure can be illustrated in Figure 2.3.

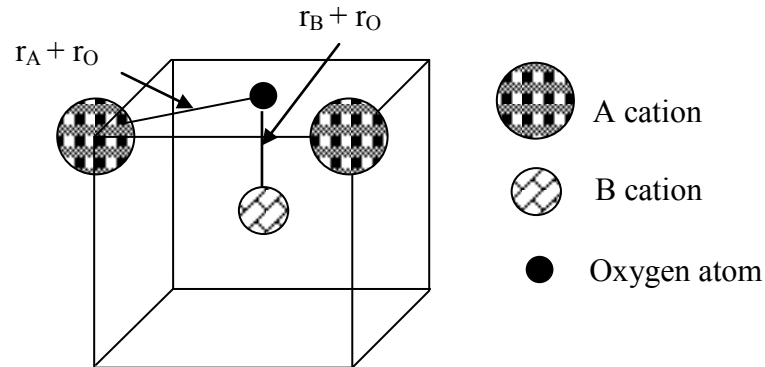


**Figure 2.3** The relationship of ionic radii in a unit cell of perovskite structure.

$$a = 2 \times B-O = 2 \times (r_B + r_O) \quad (2.2)$$

and

$$a = \frac{1}{\sqrt{2}} \times 2 \times A-O = \sqrt{2} \times (r_A + r_O) \quad (2.3)$$

hence,

$$2 \times (r_B + r_O) = \sqrt{2} \times (r_A + r_O) \quad (2.4)$$

Where, the atoms are touching one another, the B-O distance is equal to  $a/2$  ( $a$  is the cubic unit cell parameter) while the A-O distance is  $(a/\sqrt{2})$  and the relationship between the ionic radius ( $r$ ) are shown in Equation 2.4.

### 2.3.2 Oxygen nonstoichiometry

Mostly, the oxygen nonstoichiometry such as the oxygen-deficient in perovskite oxide results from the great flexibility of the perovskite framework. Normally it can be described on the basis of complex perovskite-related superstructures of general formula  $A_nB_nO_{3n-1}$ , in which the stacking manner depends on the size, electronic configurations, and coordination numbers of A and B cations. Oxygen vacancies are accomplished by substituting ions of similar size but different valence. For example, some of the  $La^{3+}$  ions in  $LaBO_3$  are replaced by  $Sr^{2+}$  to form  $La_{1-x}Sr_xBO_{3-\delta}$ , and therefore, oxygen vacancies are formed in the structure. This event is the cause of ionic compensation (most likely doubly ionized,  $V_O^{\bullet\bullet}$ ) in order to maintain charge neutrality of the materials.

### 2.4 Physical properties of perovskite

The attractive physical properties of perovskite oxide are necessary for choosing the material to use. Beside the essential property in ionic conductivity and electronic conductivity, it also presents the purpose properties such as superconductivity, colossal magnetoresistance, multitude dielectric properties of interest for thermistor applications, ferroelectricity, ferromagnetism, transport properties of interest for high temperature thermoelectric power and a fluorescence compatible with laser action.

### 2.4.1 Magnetic properties

In the ideal cubic perovskite structure, each oxygen is shared by two  $B^{3+}$  ions and formed a B-O-B angle of  $180^\circ$  in the lattice. Such a configuration is favorable for super exchange interactions between magnetic  $B^{3+}$  cations. This exchange usually results in antiparallel coupling of nearest neighbor magnetic moments. When the  $B^{3+}$  ions are in two sublattices ( $A_2BB'O_6$ ), spin arrangements are possible. If B' is a diamagnetic ion, the  $B^{3+}$  ions are aligned anti-ferromagnetically, and the most important exchange mechanism is believed to be a longer range super exchange interaction through two oxygens of the type B-O-B'-O-B. The B-B separation is now considerably longer than the 0.4 nm separation found in the ideal perovskite.

The  $\text{LnFeO}_3$  (Ln = lanthanide) perovskites are those that have attracted the most attention because of their possible applications as technological magnetic materials. These compounds show a weak spontaneous magnetic moment, which is attributed to a slight canting of the iron moments, which are otherwise antiferromagnetic aligned. In addition,  $\text{LnMnO}_3$  shows very interesting magnetic properties because these manganites containing mostly  $\text{Mn}^{3+}$  or  $\text{Mn}^{4+}$  ions show antiferromagnetic behavior. However, ferromagnetic behavior is observed in the range from 25 to 35%  $\text{Mn}^{4+}$ . A weak magnetic interaction was found between  $\text{Mn}^{3+}$  ions, together with a negative interaction between  $\text{Mn}^{4+}$  ions and a strong positive interaction between  $\text{Mn}^{3+}$  and  $\text{Mn}^{4+}$ . A similar kind of behavior was found for the combination of  $\text{Co}^{3+}$  and  $\text{Co}^{4+}$ , but the Cr and Fe compounds were found to be antiferromagnetic.

### 2.4.2 Electrical properties

Electrical conductivity or sometimes called specific conductance is a measure of a material ability to conduct an electric current. When an electrical potential difference is placed across a conductor, the movable charges flow when giving rise to an electric current. The important charge carriers for conduction of the perovskite oxide are in term of free electrons and another charge electronic

entity called holes, which also participate in electronic conduction. As the ensuing discussion reveals, the electrical conductivity is direct function of the numbers of free electrons and holes. These are presented from the charge compensation of ion in material for maintaining the electro-neutrality.

Ordinarily, materials are classified in three groups namely conductors, semiconductors and insulators. Metals are good conductors, typically having conductivities in the order of  $10^7 (\Omega\text{-m})^{-1}$ . The other materials which have very low conductivity ranging of  $10^{-10}$  to  $10^{-20} (\Omega\text{-m})^{-1}$ , are the electrical insulators. The material which be the semiconductors have an intermediate conductivity, generally from  $10^{-6}$  to  $10^4 (\Omega\text{-m})^{-1}$  [30]. However, the electrical conductivity of perovskites also show wide variations. Several compounds have been used for their dielectric properties, while others show metallic conductivity, although most are semiconductors. The charge carrier in term of free electron was separated into n-type extrinsic semiconductor and p-type extrinsic semiconductor.

#### **2.4.2.1 n-type extrinsic semiconductor [30]**

The n-type extrinsic conductor can be explained through the rearrangement in  $\text{BaSrCoFeO}_{3-\delta}$ . Such as the Ba and Sr atom have two electrons around each atom. If a dopant atom with valence 3 is doped as a substitutional impurity. Only two of three valence electrons of the impurity atom can participate in the bonding because there are only two possible bonds with neighboring atoms. The extra nonbonding electron is loosely bound to the region around the impurity atom by a weak electrostatic attraction. The energy binding of this electron is relatively small (on the order of 0.01eV), thus it is easily moved to be a free or conducting electron.

#### **2.4.2.2 p-type extrinsic semiconductor [30]**

The p-type extrinsic semiconductor is opposite effect which occurs by the addition of trivalent substitution impurities such as aluminum to silicon. One of the covalent bond around each of these atoms is deficient in an electron, thus it be presented a hole that is weakly bound to the impurity atom. This hole may be released

from the impurity atom concurrently with the transfer of electron from an adjacent bond. In essence, the electron and hole exchange position moreover a moving of hole is considered to be participates in the conduction process.

However, the electron is majority carriers by value of their density or concentration, and holes are the minority charge carriers. One of the important electrical characteristic of a solid material is the ease of transmission electric current. Ohm's law relates the current ( $I$ ) or time rate of charge passage to the applied voltage  $V$  as follows:

$$V = IR \quad (2.5)$$

Where  $R$  is the resistance of the material through with the current is passing. The units for  $V$ ,  $I$  and  $R$  are volts (J/C), ampere (C/s) and ohms (V/A), respectively.

The value of  $R$  is influenced by specimen configuration and for many materials is independent of current. The resistivity is independent of specimen geometry but related to  $R$  through the expression

$$\rho = \frac{RA}{l} \quad (2.6)$$

Where  $\rho$  is the electrical resistivity and the unit is ohm-meter ( $\Omega\text{-m}$ ),  $l$  is the distance between the two points at which the voltage is measured,  $A$  is the cross-sectional area perpendicular to the direction of the current. Normally, electrical conductivity  $\sigma$  is used to specify the electrical character of a material it is the reciprocal of the resistivity, as

$$\sigma = \frac{1}{\rho} \quad (2.7)$$

This factor indicates the ease of material which is capable of conducting an electric current. The unit for  $\sigma$  is reciprocal ohm-meter ( $\Omega\text{-m}$ )<sup>-1</sup>. In addition to Equation 2.7 Ohm's law may be expressed as

$$J = \sigma E \quad (2.8)$$

In which  $J$  is the current density, the current per unit of specimen area  $I/A$ , and  $E$  is the electric field intensity or the voltage difference between two points divided by the distance separating them that expressed as equation below.

$$E = \frac{V}{l} \quad (2.9)$$

The outermost electrons in perovskites affect the electrical behavior, which may be localized at specific atomic sites or may be collective. Since localized electrons may carry a spontaneous moment, there is a strong correlation between the electrical and magnetic properties of perovskites.

### 2.4.3 Mixed electronic-ionic conductors

Perovskite oxide exhibits the both of electronic and ionic conductivity. In the electronic conduction material, an electrical current results from the movement of electrically charge particle such as electrons or hole. In addition, the ionic conductivity also presents due to the high oxygen vacancy concentration occurred. Usually, both anion and cation in ionic materials possess an electric charge and as a consequence, are capable of migration or diffusion when an electric field is presented. Thus an electric current will result from the movement of these charge ions, which will be presented in addition to current due to any electron motion. The total conductivity of material ( $\sigma_{\text{total}}$ ) is equal to the summation of both electronic and ionic contributions, as follows:

$$\sigma_{\text{total}} = \sigma_{\text{electronic}} + \sigma_{\text{ionic}} \quad (2.10)$$

Either contribution may predominate depending on the material, its purity, and of course temperature. Moreover, the ionic contribution and the total conductivity increase with increasing temperature, as does the electronic

component. However, in spite of the two conductivity contributed, most ionic material remains insulative at elevated temperatures.

For example  $\text{La}_{1-x}\text{Sr}_x\text{BO}_{3-\delta}$  perovskite oxide when the B site ions can be mixed-valence state ions, the charge neutrality is maintained by both formations of oxygen vacancies and a change in the valence state of B site ions. The oxides may show both high oxygen ion conductivity due to the high oxygen vacancy concentration, and a high electronic conductivity due to the mixed-valence state ions [31]. The concentration of oxygen vacancies can also be increased by mild B-site ion substitution, such as Cu and Ni ions, which naturally take the divalent oxidation state [32].

#### 2.4.4 Thermal expansion

Mostly, solid materials will expand after heating and contract after cooling. The changing of temperature induces the length of the original material that may be expressed as follows:

$$\frac{l_f - l_0}{l_0} = \alpha_l (T_f - T_0) \quad (2.11)$$

or

$$\frac{\Delta l}{l_0} = \alpha_l \Delta T \quad (2.12)$$

where  $l_0$  and  $l_f$  represent as initial and final length of material, with the temperature changing from  $T_0$  to  $T_f$ . The parameter  $\alpha_l$  is the linear coefficient of thermal expansion which a material property indicates the extent of the material after heating and it relates with temperature. Thermal expansion is the resulting of increasing in the average distance between atoms in material and can be understood by considering the potential energy versus interatomic spacing of solid material. Thus, the heating of material to high temperature induces the vibration energy of atoms to higher energy so the expansion presented. However, if the potential energy is not significant change there would be no net change in interatomic separation, thus the thermal expansion is not difference. In this

research dilatometry was used for measurement and  $\text{Al}_2\text{O}_3$  has been used as the standard which has  $\alpha_1$  as  $(7.6^\circ\text{C})^{-1} \times 10^{-6}$ .

#### **2.4.5 Oxygen adsorption property**

Oxygen adsorption on perovskite oxides has been studied mainly because of these compounds as redox catalysts. Studying surface reactions based on temperature sweep, adsorption of oxygen molecules on the perovskite surfaces can be studied by using temperature-programmed desorption (TPD). The basic experiment is simple, involving the two steps as following:

1. Adsorption of one or more molecular species onto the sample surface at low temperature frequently as 300 K.
2. Heating of the sample in a control manner while monitoring the evolution of species from the surface back into the gas phase.

The data from an experiment consists of the intensity variation which relates on the concentration of the desorbed species as a function of time and temperature. Normally, the sensitivity of TPD technique is good with attainable detection limits below 0.1% of a monolayer adsorbate. Furthermore, there are some important points that should not be ignored as follow:

1. The area under a peak is proportional to the amount of original adsorbed species such as proportional to the surface coverage.
2. The kinetic of desorption gives information on the state of aggregation of the adsorbed species such as molecular.
3. The position of the peak (the peak temperature) is related to the enthalpy of adsorption such as the strength of binding to the surface.

#### **2.5 Perovskite synthesis**

The procedure for preparing perovskite oxide membrane consisted of three steps: powder synthesis, shaping and sintering. The fabrication procedure affects the microstructure of product including grain size, grain boundary and porosity.



In addition different procedures introduce various amounts of impurities in the product. Therefore, the electrical conductivity is affected by the fabrication procedure and the conductivity behavior depends on the characteristic of grain, grain boundary and porosity, as well as impurity level. There are many routes to synthesize perovskite oxide such as a conventional solid-state reaction, and solution preparation e.g. metal-EDTA, coprecipitation process and sol-gel process, etc.

### **2.5.1 Solid state reaction**

The most common procedure for synthesizing perovskite oxides is solid state reactions. It is widely used in synthesizing ceramics because it has high selectivity, high yields, no solvent used, and simplicity. However, this process also uses ball mill which can lead to contamination by the reagent or other impurities and results in the impurity forming at the grain boundary, that will reduce the ionic conduction. Therefore, the composition and structure of product often exhibit non-stoichiometry and non-homogeneous, leading to a decrease of grain conductivity. For example Zhan et al. [33] reported the worse performance of  $\text{Sm}_{0.2}\text{Ce}_{0.8}\text{O}_{1.9}$  with the low conductivity of  $9.4 \times 10^{-3} \text{ S}\cdot\text{cm}^{-1}$  at  $600^\circ\text{C}$  and activation energy of 1.01 eV after it was compared with the highest conductivity of  $12 \times 10^{-3} \text{ S}\cdot\text{cm}^{-1}$  at  $600^\circ\text{C}$  and the lowest activation energy of 0.85 eV in  $\text{Sm}_{0.2}\text{Ce}_{0.8}\text{O}_{1.9}$  reported by Balazs and Glass [34]. The phenomenon is presented due to the effect of grain boundary resistance on total resistance leading to low total conductivity. Sometimes it infers that a high impurity during process hinders oxygen ion migration through the grain boundary.

### **2.5.2 Solution preparation**

The solution preparation is a traditional method for making perovskite materials usually by mixing the constituent oxides, hydroxides and carbonates. This technique contributes the homogeneous of the solution and obtains the accurate stoichiometry in perovskite oxide. Moreover, perovskite oxide powders

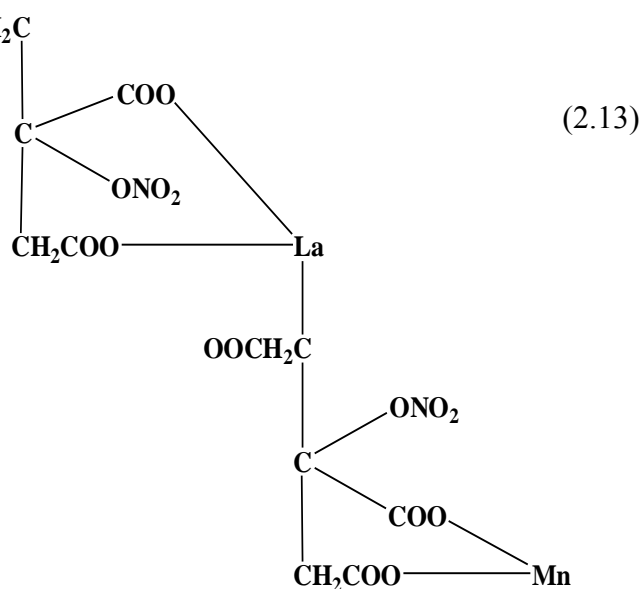
made from solution method are very fine particles, in order to overcome the disadvantages of low surface area and rarely present the agglomerate ion of powder, which facilitates for the densification process. The solution method is easily generated porous in material and enhances ability to control particle size. The popular procedures for synthesizing perovskite oxide are sol gel and coprecipitation method. The precursors generated by sol-gel preparations or co-precipitation of metal ions by precipitating agents such as hydroxide, cyanide, oxalate, carbonate, citrate ions etc., have been used.

A convenient way of classifying the methods is to consider the means used for solvent removal. There are two basic classes, firstly is based on precipitation with subsequent filtration, centrifugation, etc., to separate solid and liquid phases. The second basic method depends on thermal processes, evaporation, purification, combustion for removal the solvent. The latter method is preferred because of the possible contemporaneous conversion of the residue into the desired product.

#### **2.5.2.1 Sol gel method**

The sol gel method is one of the chemical synthesis methods. This process has been an important wet chemical route for synthesizing novel ceramic oxide composite materials, especially perovskite oxide. The most popular method of sol gel powder preparation involves four steps as follows: sol preparation, network formation in gelation where the basic factors e.g. pH, temperature, speed of mixing and condensation kinetic are investigated for controlling the gel formation. Gel dryness is a process to obtain a desired microstructure by controlling temperature condition for drying gel. And the final step is gel combustion. The gel is heated at high temperature to occur the spontaneous combustion. Generally, it is very easy to obtain stoichiometric powder with high homogeneity and single phase when using the sol gel method. Although the properties of materials produced by sol gel method are usually better than of material produced by solid state reaction, it is not always the case.

In this research, sol-gel process was performed using the citric acid as chelating agent and metal nitrate in order to produce the precursor before the chelating agent are released by thermal decomposition. The formation of metal oxide framework consists of the metal centers and oxygens that called oxo (M-O-M) or hydroxo (M-OH-M) bridges. Recently, Baythoun and Sale reported the production of Sr-substituted  $\text{LaMnO}_3$  perovskite powder prepared by the amorphous citrate process. The manganese citrate-nitrate precursor may be represented as in Equation 2.1 [35].



In this complex, the hydrogen of three  $-\text{COOH}$  groups was replaced by lanthanum, OH or  $-\text{COOH}$  groups are triply charged and replaced in one case (as in normal citrate formation). However, if the amount of citric acid not appropriate with metal ion, the formation of the precursor will be in the different framework.

In addition, the calcination temperature should be higher than 800°C to avoid the segregation of Sr(NO<sub>3</sub>)<sub>2</sub> during precursor preparation and the production of SrCO<sub>3</sub> during precursor decomposition. Moreover, Singh K.A. et al. [36] indicated that the suitable temperature for combustion of citrate-nitrate solution for preparation of nano-crystalline cubic YSZ powder was around 260°C. The DSC plot revealed an exothermic peak at 260°C. It means that the exothermic heat generated in the combustion and governed by the thermally induced redox reaction of citrate and nitrate in the precursor.

#### **2.5.2.2 Co-precipitation process**

Ordinarily, the co-precipitation is used for synthesis of nano-particles material. This process is concerned on (a) the precipitation of product which formed under high super saturation condition, and (b) the nucleation which is the key step of precipitation process that depends on the condition and the large number of small particle formed. However the secondary process such as ripening and aggregation will also affect on the size, morphology and properties of products. The advantage of co-precipitation method is to obtain stoichiometric fine powder through direct reaction in the solution. Thus, the fine particles facilitate in sinterability of product and have affected on the grain boundary conductivity. For example, Christies et al. [37] demonstrated that the small grain size showed very low grain resistance and associated with a decrease in electrode polarization resistance, so the conductivity also increased.

### **2.6 Powder sizing**

Powder particles have an influence on compacting and sintering of a dense membrane. Mostly, the objective of the pressing step is to achieve maximum particles in packing and uniformity, so that minimum shrinkage and retained porosity will present during densification. However a single particle size of material does not suitable for producing a good packing; for example, the optimum packing of particles with the same size results in over 30% void space. Adding particles of an equivalent

size to the largest voids will reduce the void to 23%. Therefore, to achieve maximum particle packing, a range of particle sizes is required.

Hard and dense agglomerates in ceramic powders usually result in large interagglomerate pores after sintering. Thus the small particle size is very important because it facilitates to produce the high strength of the disc and contributes in the sintering process. The primary driving force for densification of a compact powder at high temperature is the change in surface free energy. Due to high surface areas of very small particles, the high surface free energy and strong thermodynamic driving force are decreased by bonding the particle together. The particle with approximate sizes of 1  $\mu\text{m}$  or less can be compacted into a porous shape and sintered at high temperature to near-theoretical density [38]. Typically, the finer the powder has, the greater in surface area, the lower temperature and the shorter time for densification are obtained. Long time of sintering temperature causes the increase of grain growth and lowering the material strength. Normally, the calcined powder is not usually available with the optimum particle size distribution, thus it needs to use some techniques for making the desired particle size of powder such as ball milling and screening techniques.

### **2.6.1 Powder compacting by uniaxial pressing**

Uniaxial pressing is used to produce the material into a disc form. It is accomplished by placing the powder into a rigid die and applying pressure through the material along single axial direction by a rigid plunger, or piston to achieve a compacting disc. Pressing results in the direct contact of particles, reduces the average distance between particles, and changes the shape of particles. The apparent density of a compact disc is controlled by properly mixing of various particles size fractions.

To enhance the compacting, before pressing, the powder should be disaggregated by mixing the powder with solvent such as isopropanol in the ultrasonic bath or adding a couple drop of acetone to reduce the surface tension.

## 2.7 Sintering [39]

The sintering process is the thermal treatment of powder or compact disc at temperature below the melting point of the main component, for the purpose of increasing its strength by bonding together of the particles. The sintering in polycrystalline materials are considerably more complex than those in viscous sintering of amorphous materials due to the availability of several matter transport paths and the presence of grain boundaries. Matter transport in solid-state sintering can occur by at least six different paths which defines the mechanisms of sintering. However, the most important consequence of the grain boundaries is the occurrence of grain growth and pore growth during the sintering. This process normally refers to as coarsening, that provides an alternative route for the free energy of powder system to be reduced therefore, it also reduces the driving force for densification. The interplay between the two processes refers to as a competition between sintering and coarsening. Commonly, the model of sintering assumed uniform packing of spherical particles, the occurrence of mass transport mechanism, and no grain growth.

### 2.7.1 Mechanism of sintering

Sintering of polycrystalline materials occurs by the diffusion of matter along definite paths. The matter is transported from regions of higher chemical potential (the source of matter) to lower chemical potential (the sink). Normally, there are six mechanisms of sintering in polycrystalline materials, as shown in Figure 2.4. Three particles are bonding and growth of necks between the particles leads to the strength of the powder compact increased. This phenomenon leads to the particle shrinkage or densification. Surface diffusion, lattice diffusion from the particle surfaces to the neck and vapor transport (mechanism 1, 2 and 3) lead to the neck growth without densification, that is referred to nondensifying. Grain boundary diffusion and lattice diffusion from the grain boundary to the pore (mechanism 4 and 5) are the most important densifying mechanisms in polycrystalline. The diffusion of grain boundary to the pore permits the neck growth as well as densification. Then, the plastic flow by dislocation motion (mechanism 6) also leads to neck growth and densification but is

more common in the sintering of metal powders. However, the nondensifying mechanism cannot be ignored because it reduces the curvature of the neck surface such as the driving force for sintering and also reduces the rate of the densification mechanisms. In addition to the alternative mechanisms, there are additional complications arising from the diffusion of the different ionic species making up the compound. The flux of the different ionic species depends on the stoichiometry and electroneutrality of the compound.

For amorphous materials (glasses), grain boundaries, neck growth, and densification do not occur by viscous flow involving deformation of the particles.

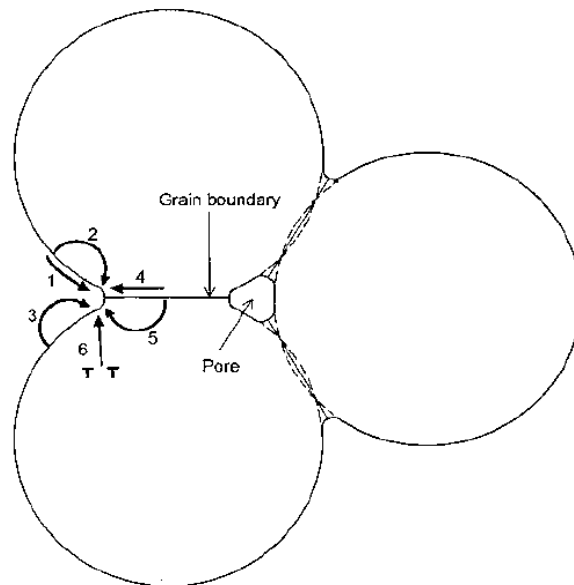


**Figure 2.4** The mechanisms of sintering in crystalline particles model.

Normally, sintering is thought to be occurred in three sequential stages referred to 1) initial stage, 2) intermediate stage, and 3) final stage. Polycrystalline materials show the geometrically ideal structures that were proposed by Coble [40] as the representative of the three stages.

Initial stage consists of the interparticle neck growth by diffusion, vapor transport, and plastic flow. For a powder system consisting of spherical particles, the initial stage is represented as the transition between Figure.2.5a and 2.5b. An initial density of a powder system is 0.5-0.6 of the theoretical density, that corresponds to a linear shrinkage of 3 to 5% or increase in density to 0.65 of the theoretical when the densifying mechanism is dominated.

Intermediate stage is presented when the pores have reached their equilibrium shapes as order by the surface and interfacial tensions. The structure of the sintering model is usually idealized in terms of a spaghetti-like array of porosity sitting along the grain edges as illustrated in Figure. 2.5c. Densification is assumed to occur by the shrinkage of pores to reduce their cross section. Finally, the pores become unstable and pinch off, leaving isolated pores. The intermediate stage normally covers the major part of the sintering process and it is taken to end when the density achieves around 0.9 of the theoretical one.

In the final stage, the microstructure can develop in many ways. In one of the simplest descriptions, the final stage begins when the pores pinch off and become isolated at the grain boundary, as shown by the ideal structure in Figure.2.5d. In this stage the pores are assumed to shrink continuously and may be disappeared altogether, the porosity has been achieved in the sintering of real powder systems.

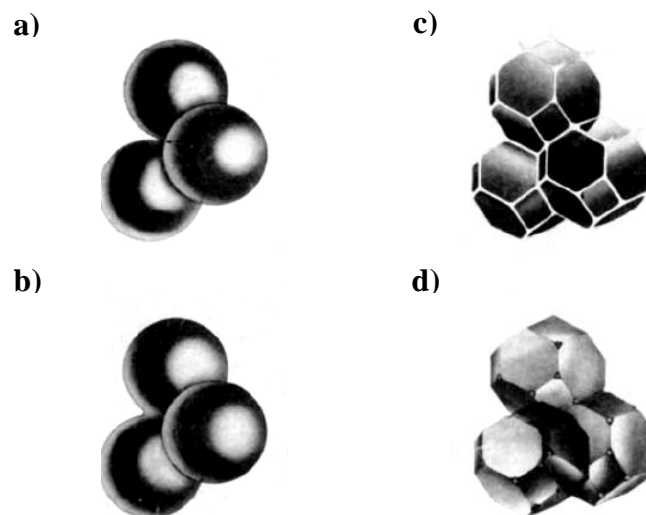


**Figure 2.5** The idealized models for the three stages of sintering a) Initial stage b) End of the initial stage c) Intermediate stage d) Final stage.



## 2.8 Electrical measurement

### 2.8.1 DC 4-probes technique

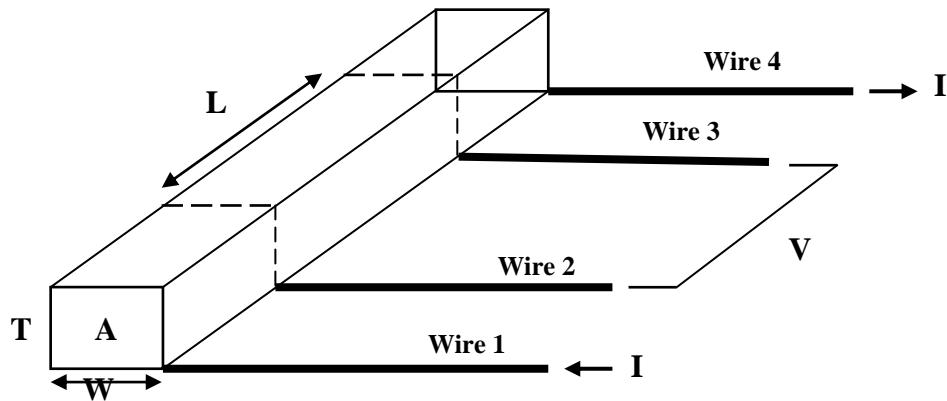


**Figure 2.6** DC 4-probes measurement.

The DC 4-probes technique is used for measured the resistance of material by using 4 wire probes which are contacted on each side of the specimen as shown in Figure 2.6. Normally the wire can be platinum or gold because these conductors have low resistance.

The measurement starts with the input of a current,  $I$ , through the outer wires 1 and 4 and measures the voltage drop off between the inner wire 2 and 3 by using a very high Ohmic measurement device, so that the current flows through the wire 2 and 3 nearly zero. In this case, the individual, additional contact resistance does not play a role because it has negligible resistance, thus it can be cut out of the equation. To study the behavior of the structure an  $I/V$  curve is generated, typically in the  $\mu\text{A}$  to the  $\text{mA}$  range. If assume the resistance of a material to be  $R$ , the following equation applied:

$$R = \frac{\rho L}{A} \quad (2.14)$$

With  $L$  = the length of the structure (m)

$A$  = the area (width x thickness) of the cross section ( $\text{m}^2$ )

$\rho$  = the specific resistivity ( $\Omega\cdot\text{m}$  of the practical unit  $\mu\Omega\cdot\text{cm}$ )

# CHAPTER III

## EXPERIMENTAL

The chemicals, synthesis, characterization procedures and measurement methods of perovskite oxides are described as below:

### 3.1 Chemicals

The chemicals listed in Table 3.1, were used without further purification.

**Table 3.1** Chemical and reagents for synthesis of perovskite oxide

Reagents	Formula Weight	Purity%	Company
Ba(NO <sub>3</sub> ) <sub>2</sub>	261.53	99.0	Fluka
Sr(NO <sub>3</sub> ) <sub>2</sub>	211.63	99.0	Fluka
Co(NO <sub>3</sub> ) <sub>2</sub> ·6H <sub>2</sub> O	291.03	≥98	Fluka
Fe(NO <sub>3</sub> ) <sub>3</sub> ·9H <sub>2</sub> O	404.00	98.0-101	Fluka
La(NO <sub>3</sub> ) <sub>3</sub> ·6H <sub>2</sub> O	433.02	≥99	Fluka
Ca(NO <sub>3</sub> ) <sub>2</sub>	236.15	99.0	SD fine-chem
Cu(NO <sub>3</sub> ) <sub>2</sub> ·3H <sub>2</sub> O	241.6	99–104	Fluka
Zn(NO <sub>3</sub> ) <sub>2</sub> ·6H <sub>2</sub> O	297.48	99.0	Fluka
C <sub>6</sub> H <sub>8</sub> O <sub>7</sub>	192.13	99.5	Riedel-deHaën
HNO <sub>3</sub>	63.01	65	Merck
NH <sub>3</sub> ·H <sub>2</sub> O	35.05	25	Merck
C <sub>2</sub> H <sub>5</sub> OH	46.07	≥99.9	Merck

### 3.2 Synthesis of perovskite oxide powder by modified citrate method

All compositions in Table 3.2 were synthesized in basic solution.

**Table 3.2** The components of all samples

Doped	Replaced	Components	Abbreviation
-	-	$\text{Ba}_{0.5}\text{Sr}_{0.5}\text{Co}_{0.8}\text{Fe}_{0.2}\text{O}_{3-\delta}$	BSCF
Ca in A site	Ba and Sr	$(\text{Ba}_{0.45}\text{Sr}_{0.45})_{0.9}\text{Ca}_{0.1}\text{Co}_{0.8}\text{Fe}_{0.2}\text{O}_{3-\delta}$	BSCa <sub>0.1</sub> CF
		$(\text{Ba}_{0.4}\text{Sr}_{0.4})_{0.8}\text{Ca}_{0.2}\text{Co}_{0.8}\text{Fe}_{0.2}\text{O}_{3-\delta}$	BSCa <sub>0.2</sub> CF
		$(\text{Ba}_{0.35}\text{Sr}_{0.35})_{0.7}\text{Ca}_{0.3}\text{Co}_{0.8}\text{Fe}_{0.2}\text{O}_{3-\delta}$	BSCa <sub>0.3</sub> CF
		$(\text{Ba}_{0.3}\text{Sr}_{0.3})_{0.6}\text{Ca}_{0.4}\text{Co}_{0.8}\text{Fe}_{0.2}\text{O}_{3-\delta}$	BSCa <sub>0.4</sub> CF
		$(\text{Ba}_{0.3}\text{Sr}_{0.3})_{0.6}\text{Ca}_{0.5}\text{Co}_{0.8}\text{Fe}_{0.2}\text{O}_{3-\delta}$	BSCa <sub>0.5</sub> CF
La in A site	Ba and Sr	$(\text{Ba}_{0.4}\text{Sr}_{0.4})_{0.8}\text{La}_{0.2}\text{Co}_{0.8}\text{Fe}_{0.2}\text{O}_{3-\delta}$	BSLCF
La, Ca in A site	Ba and Sr	$(\text{Ba}_{0.5}\text{Sr}_{0.4})_{0.8}\text{La}_{0.15}\text{Ca}_{0.05}\text{Co}_{0.8}\text{Fe}_{0.2}\text{O}_{3-\delta}$	BSLa <sub>0.15</sub> Ca <sub>0.05</sub> CF
		$(\text{Ba}_{0.5}\text{Sr}_{0.4})_{0.8}\text{La}_{0.1}\text{Ca}_{0.1}\text{Co}_{0.8}\text{Fe}_{0.2}\text{O}_{3-\delta}$	BSLa <sub>0.1</sub> Ca <sub>0.1</sub> CF
		$(\text{Ba}_{0.5}\text{Sr}_{0.4})_{0.8}\text{La}_{0.05}\text{Ca}_{0.15}\text{Co}_{0.8}\text{Fe}_{0.2}\text{O}_{3-\delta}$	BSLa <sub>0.05</sub> Ca <sub>0.15</sub> CF
La 0.2, Ca excess in A site	Ba and Sr	$(\text{Ba}_{0.5}\text{Sr}_{0.4})_{0.8}\text{La}_{0.2}\text{Ca}_{0.01}\text{Co}_{0.8}\text{Fe}_{0.2}\text{O}_{3-\delta}$	BSLCFCa <sub>0.01</sub>
		$(\text{Ba}_{0.5}\text{Sr}_{0.4})_{0.8}\text{La}_{0.2}\text{Ca}_{0.02}\text{Co}_{0.8}\text{Fe}_{0.2}\text{O}_{3-\delta}$	BSLCFCa <sub>0.02</sub>
		$(\text{Ba}_{0.5}\text{Sr}_{0.4})_{0.8}\text{La}_{0.2}\text{Ca}_{0.03}\text{Co}_{0.8}\text{Fe}_{0.2}\text{O}_{3-\delta}$	BSLCFCa <sub>0.03</sub>
		$(\text{Ba}_{0.5}\text{Sr}_{0.4})_{0.8}\text{La}_{0.2}\text{Ca}_{0.04}\text{Co}_{0.8}\text{Fe}_{0.2}\text{O}_{3-\delta}$	BSLCFCa <sub>0.04</sub>
		$(\text{Ba}_{0.5}\text{Sr}_{0.4})_{0.8}\text{La}_{0.2}\text{Ca}_{0.05}\text{Co}_{0.8}\text{Fe}_{0.2}\text{O}_{3-\delta}$	BSLCFCa <sub>0.05</sub>
Cu addition in B site	Addition	$\text{Ba}_{0.5}\text{Sr}_{0.5}\text{Co}_{0.8}\text{Fe}_{0.2}\text{Cu}_{0.05}\text{O}_{3-\delta}$	BSCFCu <sub>0.05</sub>
		$\text{Ba}_{0.5}\text{Sr}_{0.5}\text{Co}_{0.8}\text{Fe}_{0.2}\text{Cu}_{0.1}\text{O}_{3-\delta}$	BSCFCu <sub>0.1</sub>
		$\text{Ba}_{0.5}\text{Sr}_{0.5}\text{Co}_{0.8}\text{Fe}_{0.2}\text{Cu}_{0.15}\text{O}_{3-\delta}$	BSCFCu <sub>0.15</sub>
		$\text{Ba}_{0.5}\text{Sr}_{0.5}\text{Co}_{0.8}\text{Fe}_{0.2}\text{Cu}_{0.2}\text{O}_{3-\delta}$	BSCFCu <sub>0.2</sub>
Zn addition in B site	Addition	$\text{Ba}_{0.5}\text{Sr}_{0.5}\text{Co}_{0.8}\text{Fe}_{0.2}\text{Zn}_{0.05}\text{O}_{3-\delta}$	BSCFZn <sub>0.05</sub>
		$\text{Ba}_{0.5}\text{Sr}_{0.5}\text{Co}_{0.8}\text{Fe}_{0.2}\text{Zn}_{0.1}\text{O}_{3-\delta}$	BSCFZn <sub>0.1</sub>
		$\text{Ba}_{0.5}\text{Sr}_{0.5}\text{Co}_{0.8}\text{Fe}_{0.2}\text{Zn}_{0.15}\text{O}_{3-\delta}$	BSCFZn <sub>0.15</sub>
		$\text{Ba}_{0.5}\text{Sr}_{0.5}\text{Co}_{0.8}\text{Fe}_{0.2}\text{Zn}_{0.2}\text{O}_{3-\delta}$	BSCFZn <sub>0.2</sub>

The modified citrate method was employed for preparation of perovskite powder. The precursor chemicals in the analytical grades were  $\text{Ba}(\text{NO}_3)_2$ ,  $\text{Sr}(\text{NO}_3)_2$ ,  $\text{Ca}(\text{NO}_3)_2$ ,  $\text{La}(\text{NO}_3)_3 \cdot 6\text{H}_2\text{O}$ ,  $\text{Fe}(\text{NO}_3)_3 \cdot 9\text{H}_2\text{O}$ ,  $\text{Co}(\text{NO}_3)_2 \cdot 6\text{H}_2\text{O}$ ,  $\text{Cu}(\text{NO}_3)_2 \cdot 3\text{H}_2\text{O}$  and  $\text{Zn}(\text{NO}_3)_2 \cdot 6\text{H}_2\text{O}$ . Stoichiometric amounts of corresponding high purity metal nitrates were dissolved in nitric solution (65% v/v) to prepare the metal solution and stirred at room temperature for 6 hrs. Citric acid with high purity grade (>99.5%) was used as a chelating agent, an appropriate amount of citric acid (citric acid: metal ion ratio of 2:1) was dissolved in de-ionized water and poured into the metal solution. The mixture solution was then stirred at room temperature for 24 hrs before the pH of solution was adjusted to be about 9 and the solution color changed to brown color. The solution was then heated around  $250^\circ\text{C}$  on a hot plate stirrer until the spontaneous combustion was occurred and the black product was obtained. The product was then transferred into a muffle furnace for calcination at  $900\text{-}1000^\circ\text{C}$  for 5 hrs in air with the heating rate of  $6.5^\circ\text{C}/\text{min}$  to produce the perovskite oxide phase.

A dense membrane disc was prepared by milling the perovskite oxide powder in mortar for three times using ethanol as solvent. Then, pressing the fine powder into a pellet (15 mm in diameter and 1.5 mm in thickness) under pressure of 2 tons for 20 minutes and sintering in a muffle furnace at  $900\text{-}1100^\circ\text{C}$ , depending on the material composition for 10 hrs with heating rate of  $6.5^\circ\text{C}/\text{min}$  in order to obtain a dense membrane disc. The disc was cut into a rectangular shape (5.5 x 12 mm.) for measuring electrical conductivity and thermal expansion coefficient (TEC). Phase identification and lattice parameter of BSCF samples in both powder and dense membrane disc were examined by X-ray diffraction (XRD) analysis. Morphology and elemental component of the sintered bodies were observed by scanning electron microscope (SEM) and electron probe micro analyzer (EPMA), respectively. The elemental mapping analysis was investigated by energy dispersive X-ray spectroscopy (EDX). Relative densities of the disc samples were determined by Archimedes method. The perovskite oxide disc obtained after sintering were milled into powder again and measured for the oxygen adsorption property by using the Temperature-program desorption (TPD). The electrical conductivity was conducted in air by the DC four-probe technique.

### **3.3 Characterization Techniques**

#### **3.3.1 X-Ray Diffractometry (XRD)**

The phase formation of perovskite oxide was taken by using Rigaku, DMAX 2002 Ultima Plus X-Ray powder diffractometer equipped with a monochromator and a Cu–target X-ray tube (40 kV, 30 mA). The analysis angles were performed at  $2\theta$  range from 20-70 degree (step time 0.5 sec, scan step 0.020 degree) at Department of Chemistry, Faculty of Science, Chulalongkorn University.

#### **3.3.2 Scanning Electron Microscopy (SEM)**

The morphology and chemical composition of the sintered discs were characterized by a JEOL JSM-5800LV scanning electron microscopy and energy dispersive x-ray spectrometry (EDX), Oxford Instrument (Link ISIS series 300) at the Scientific and Technological Research Equipment Center (STREC), Chulalongkorn University. This instrument uses X-rays or electrons back scattered from the surface “illuminated” by restored electron beam to generate an image with remarkable three-dimensional qualities.

#### **3.3.3 Electron Probe Micro Analyzer (EPMA)**

The morphology and elemental components of sinter discs were also observed by the electron microprobe analyzer (Shimadzu EPMA-1600), Oxford Instrument at the Analysis center of Nagaoka University of Technology, Japan. The accelerate voltage and beam current for measuring was 15 kV and 0.2 nA. The sample were sputtered with Au for 500 Å in thickness. The chemical composition on a surface of perovskite discs was analyzed using the principle of back scattered electrons (BSE).

### **3.3.4 Relative density**

The relative density of perovskite disc was determined by the Archimedes immersion method using DI water as a medium, on Precisa Gravimetrics AG (model R 2055M-DR), at Department of Environmental System Engineering, Nagaoka University of Technology, Niigata, Japan.

The specimen was boiled in the DI water at 150°C for 5 hrs for releasing air in pores of the specimen. The specimen was then weighed in dry and wet condition and calculated for the relative density.

### **3.3.5 Temperature Program Desorption (TPD)**

The perovskite oxide capability of oxygen adsorption was measured by oxygen Temperature-program desorption (O<sub>2</sub>-TPD) model CHEMBET-3000 at Analysis center, Nagaoka University of Technology, Japan.

A 100-mg of sample powder obtained after milled the sintered disc was loaded in a U-shape quartz tube (cell). Then, the cell of perovskite sample was placed in the mantle bag and heated from room temperature to 350°C in the N<sub>2</sub> atmosphere for 1 hr under the flow rate of 120 ml/min. After the cell was cooled down to room temperature, high purity of O<sub>2</sub> gas (99.99% purity) was purged into the cell instead of N<sub>2</sub> gas for 10 min at room temperature for adsorption. After that the N<sub>2</sub> gas line was switched off and the cell was transferred to the analysis part. Then the sample was heated from room temperature to 800°C with a heating rate of 20°C/min in He flow to eliminate the physically adsorbed O<sub>2</sub> from the surface of perovskite. The TCD detector was used for detecting the amount of desorbed oxygen from the perovskite sample.

### **3.3.6 Electrical Conductivity Measurement**

The electrical conductivity of perovskite specimen was investigated by DC four - probe technique. The DC method is usually based on a combination of two types of measurement; ohmic contribution by current interruption, and the

measurement of electrode overpotentials using reference electrodes. In this experiment, the first scenario was performed at Department of Environmental system engineering, Nagaoka University of Technology, Niigata, Japan. The electrical furnace and multi-meter (Keithley 2000) were used for input the currents to the specimen through the outer gold wires. The sintered perovskite discs were cut into a rectangular shape (5 mm in width  $\times$  12 mm in length  $\times$  1.5 mm in thickness) and wrapped with the Au-wire electrodes on four sides of the specimen and bonded with Au paste as shown in Figure 3.1. The samples were heated at 850°C for 1 hr with heating rate of 3.3°C/min to allow complete adhesion between the electrodes and specimen. The conductivity of specimens was performed in a tubular furnace and used Au wires in alumina tubes to connect with four wires of the specimen.

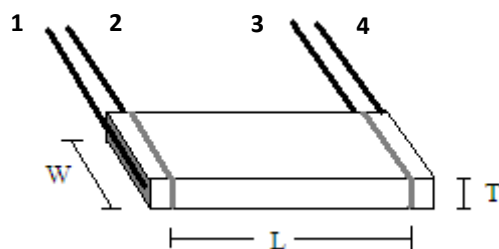


**Figure 3.1** The rectangular sample wrapped with gold (Au) wire when  $W$  = width  
 $L$  = length  $T$  = thickness

The electrical conductivity measurements were started as a given current (0.1 to 200 mA) was issued through the outer wires (no. 1 and 4 in Figure 3.1). The voltage between the inner wires at distance  $L$  (2 and 3) was measured every increasing temperature of 50°C. The measurements were performed from room temperature to 800°C with a heating rate of 3.33°C/min.

The electrical conductivity was calculated by the equation:

$$S = (I/V) * (L / (W * T)) \dots \dots \dots (2.1)$$

S = electrical conductivity

I = input current (A)

V = resulting potential (V)

L = length between Pt (cm)

T = thickness of membrane (cm)

W = width of membrane (cm)

### **3.3.7 Dilatometer**

The sintered perovskite discs were cut into a rectangular shape similar to the specimen prepared for the electrical conductivity measurement. The thermal expansion coefficients were measured from room temperature to 800°C in air with a heating rate 10 K/min by dilatometer (NETZSCH DIL 402C) at Department of Materials Science, Faculty of Science, Chulalongkorn University.



## CHAPTER IV

### RESULTS AND DISCUSSION

In this work, perovskite oxide powders were synthesized by modified citrate method and studied the effect of dopant content in substitution of A-site (Ba and Sr) and B-site (Co and Fe) in primitive BSCF.

#### **4.1 Preparation and properties of $(\text{Ba}_{0.5}\text{Sr}_{0.5})_{1-x}\text{Ca}_x\text{Co}_{0.8}\text{Fe}_{0.2}\text{O}_{3-\delta}$ (BSCCF), $(0 \leq x \leq 0.5)$ perovskite oxide.**

##### **4.1.1 Phase formation of $(\text{Ba}_{0.5}\text{Sr}_{0.5})_{1-x}\text{Ca}_x\text{Co}_{0.8}\text{Fe}_{0.2}\text{O}_{3-\delta}$ perovskite**

The x-ray diffraction patterns of  $(\text{Ba}_{0.5}\text{Sr}_{0.5})_{1-x}\text{Ca}_x\text{Co}_{0.8}\text{Fe}_{0.2}\text{O}_{3-\delta}$  (BSCCF) perovskites after calcined are shown in Figure 4.1. The BSCCF samples ( $0 \leq x \leq 0.4$ ) showed a cubic phase of  $\text{ABO}_3$ -perovskite structure with a space group of  $Pm\bar{3}m$  (221). The partial substitution of  $\text{Ca}^{2+}$  ions in A-site with the composition of 30 mol % or greater ( $x \geq 0.3$ ) exhibited a weak reflection line of primitive cubic perovskite and the impurity phase of CaO. The weak reflection could be caused by the distortion of the cubic phase to form a new phase structure. The reflection patterns of BSCCF phase shifted to the higher angles with increasing  $\text{Ca}^{2+}$  ion content, suggesting a decrease of  $d$ -spacing due to the substitution of lower ionic radius of  $\text{Ca}^{2+}$  (134 pm) ions for the higher ionic radius cations such as  $\text{Ba}^{2+}$  (161 pm) and  $\text{Sr}^{2+}$  (144 pm) ions. This substitution leads to the shrinkage in the lattice parameter and a decrease of the crystallite size, as summarized in Table 4.1. However, the substitution of  $\text{Ca}^{2+}$  ion in BSCF more than 40 mol% composition presented the complete phase transformation from  $\text{ABO}_3$  structure to  $\text{K}_2\text{NiF}_4$  structure.

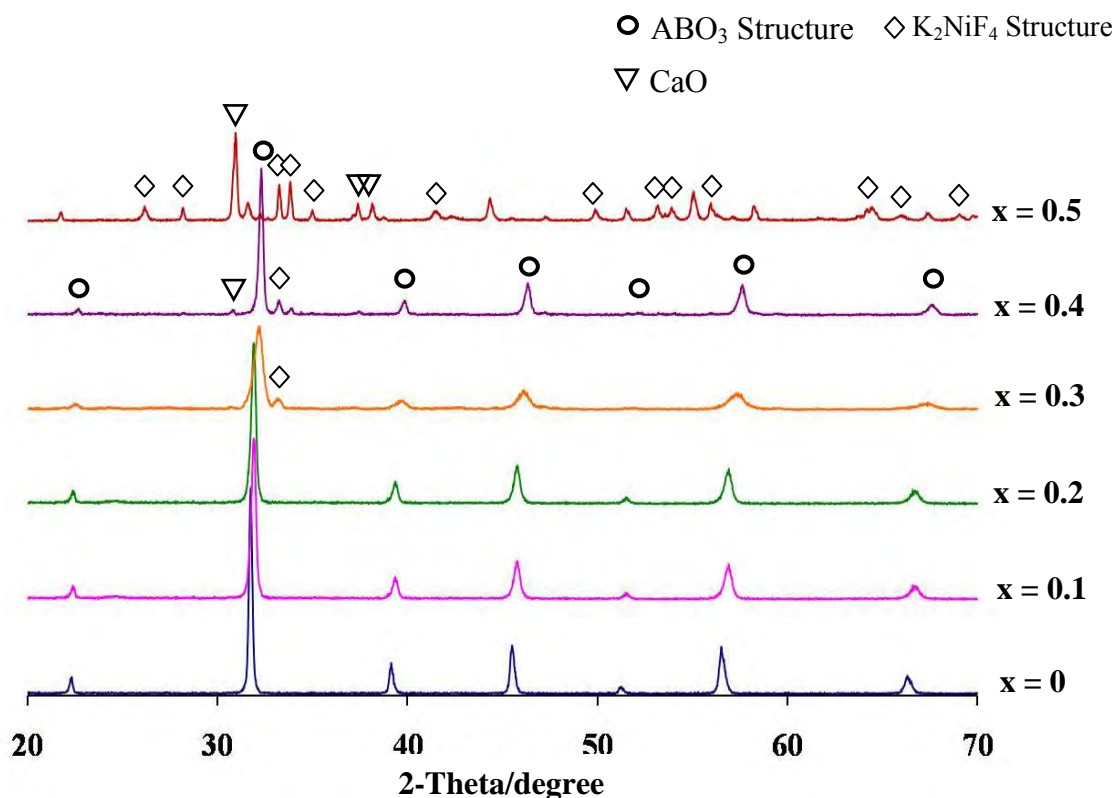


**Figure 4.1** XRD patterns of  $(\text{Ba}_{0.5}\text{Sr}_{0.5})_{1-x}\text{Ca}_x\text{Co}_{0.8}\text{Fe}_{0.2}\text{O}_{3-\delta}$ , ( $0 \leq x \leq 0.5$ ) powder

after calcined at 1000°C for 5 hrs.

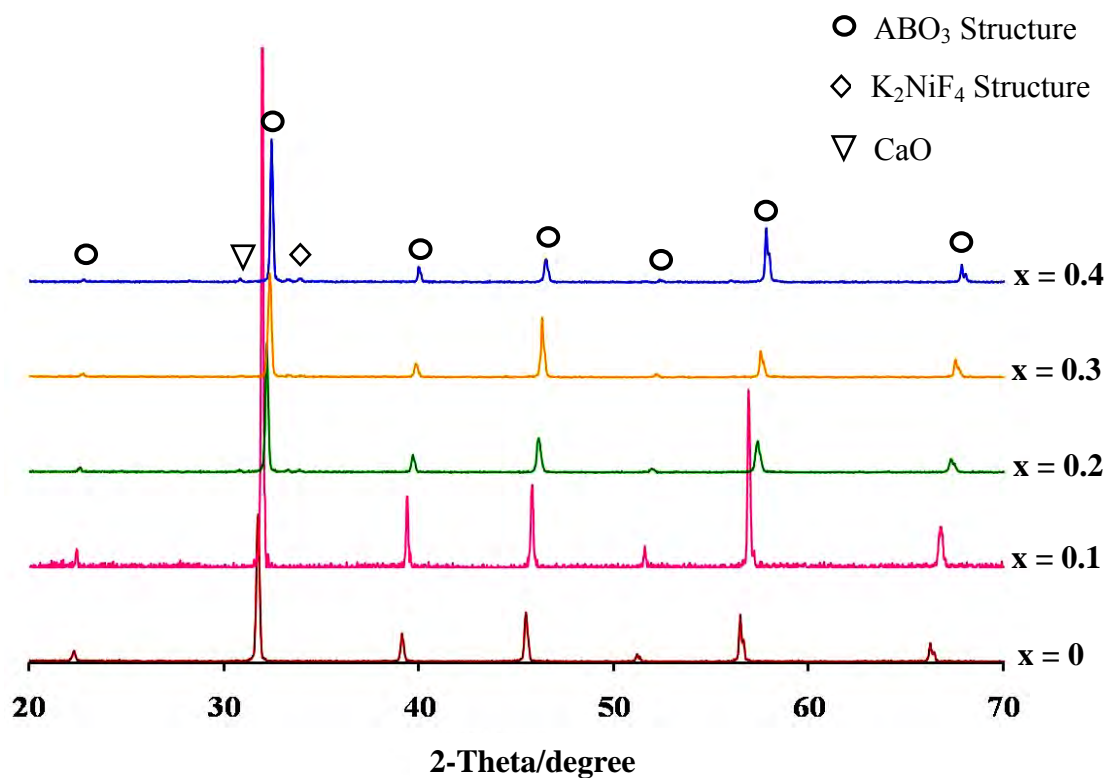


**Figure 4.2** XRD patterns of  $(\text{Ba}_{0.5}\text{Sr}_{0.5})_{1-x}\text{Ca}_x\text{Co}_{0.8}\text{Fe}_{0.2}\text{O}_{3-\delta}$ , ( $0 \leq x \leq 0.4$ ) membranes

after sintered at 1100°C for 10 hrs.

**Table 4.1** Lattice parameters of  $(\text{Ba}_{0.5}\text{Sr}_{0.5})_{1-x}\text{Ca}_x\text{Co}_{0.8}\text{Fe}_{0.2}\text{O}_{3-\delta}$  ( $0 \leq x \leq 0.4$ ) powder after calcined at  $1000^\circ\text{C}$  for 5 hrs

<b>Samples</b>	<b>Lattice Parameter (nm)</b>
x = 0.0	0.398(5)
x = 0.1	0.396(8)
x = 0.2	0.395(2)
x = 0.3	0.394(1)
x = 0.4	0.392(0)

In Figure 4.2, X-ray diffraction patterns of BSCCF perovskites discs after sintered at  $1100^\circ\text{C}$  also showed the single phase of cubic perovskite structure. The main peak of BSCCF shifted to the high angle indicating that the lattice parameter was decreased according to the increasing of  $\text{Ca}^{2+}$  ions content. Moreover, the increasing of temperature in sintering process would facilitate the formation of the single phase of perovskite oxide, which can be seen in the sample doping with 30 mol%  $\text{Ca}^{2+}$  ions that easily dissolved and substituted in the cubic structure. However in the case of 40 mol%  $\text{Ca}^{2+}$  ions, the structure still exhibited a weak reflection line of the primitive cubic perovskite structure and a small CaO phase.

#### **4.1.2 The surface morphology of $(\text{Ba}_{0.5}\text{Sr}_{0.5})_{1-x}\text{Ca}_x\text{Co}_{0.8}\text{Fe}_{0.2}\text{O}_{3-\delta}$ , ( $0 \leq x \leq 0.4$ )**

Figure 4.3 shows the surface morphology of specimens, which were partially substituted by  $\text{Ca}^{2+}$  ions in the A-site of BSCF. With increasing  $\text{Ca}^{2+}$  ions content, the dense microstructure with few isolated pores and small grain sizes were obtained.

Because the partial substitution of higher melting point dopants of  $\text{Ca}^{2+}$  ion led to the faster in the nucleation process, the increase in  $\text{Ca}^{2+}$  ion content would obtain the small particle sizes. In addition, it can increase the sintering ability which related to the relative density of specimen, as shown in Table 4.2. However, the doping of  $\text{Ca}^{2+}$  ions at 40 mol% presented small grains along the grain boundary of the sintered sample, which corresponding to the XRD analysis, suggesting the solid-solubility limit of  $\text{Ca}^{2+}$  ions in the cubic perovskite structure.

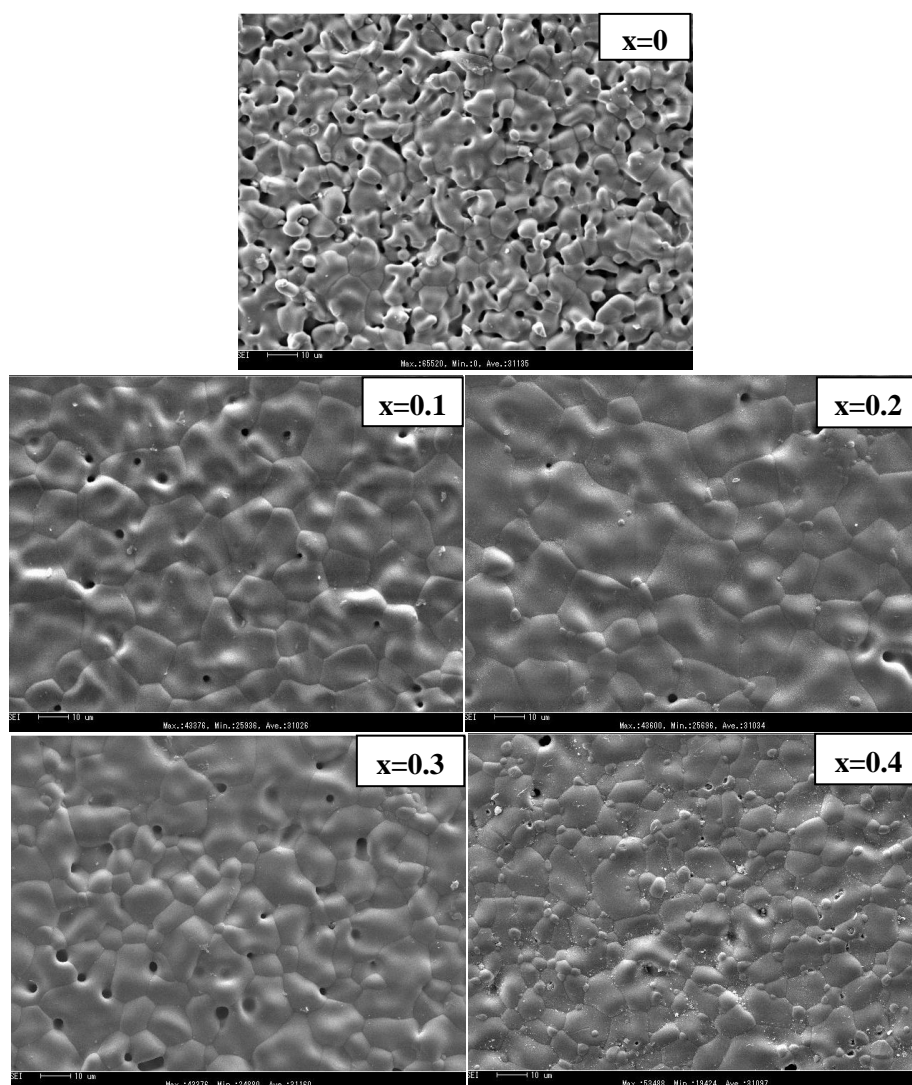


**Figure 4.3** SEM micrographs of  $(\text{Ba}_{0.5}\text{Sr}_{0.5})_{1-x}\text{Ca}_x\text{Co}_{0.8}\text{Fe}_{0.2}\text{O}_{3-\delta}$ , ( $0 \leq x \leq 0.4$ ) after sintered at 1100°C for 10 hrs.

Figure 4.4 shows the homogeneous distribution of  $\text{Ca}^{2+}$  ion in BSCCF, which confirms that the  $\text{Ca}^{2+}$  ions could substitute in the BSCF perovskite oxide.

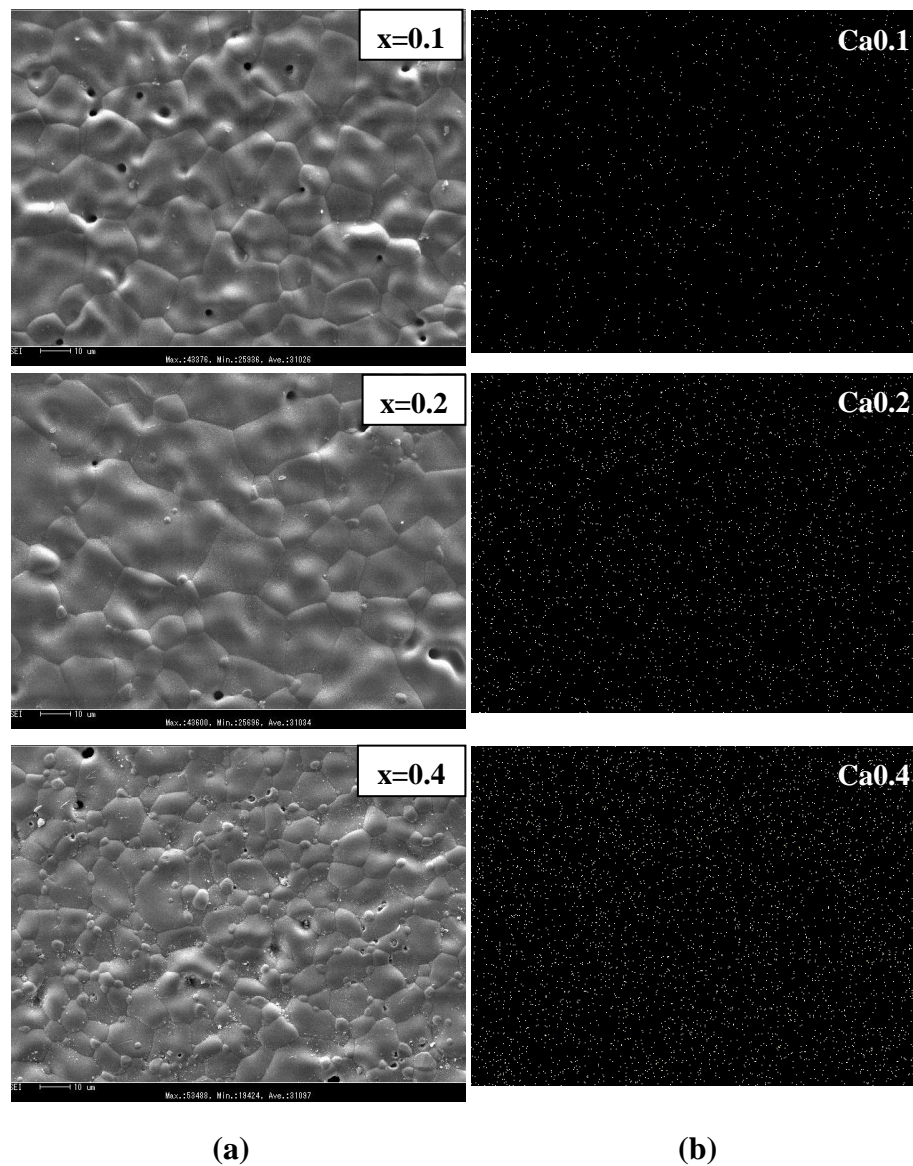


**Figure 4.4** Surface morphology (a) and elemental mapping (b) of  $(\text{Ba}_{0.5}\text{Sr}_{0.5})_{1-x}\text{Ca}_x\text{Co}_{0.8}\text{Fe}_{0.2}\text{O}_{3-\delta}$ , ( $x = 0.1, 0.2, 0.4$ ) discs.

**Table 4.2** The relative density of  $(\text{Ba}_{0.5}\text{Sr}_{0.5})_{1-x}\text{Ca}_x\text{Co}_{0.8}\text{Fe}_{0.2}\text{O}_{3-\delta}$  ( $0 \leq x \leq 0.4$ )

membrane after sintered at 1100°C

Samples	Relative density
	(%)
x = 0.0	84.00
x = 0.1	94.37
x = 0.2	95.33
x = 0.3	95.52
x = 0.4	95.20

#### 4.1.1 Electrical Conductivity of $(\text{Ba}_{0.5}\text{Sr}_{0.5})_{1-x}\text{Ca}_x\text{Co}_{0.8}\text{Fe}_{0.2}\text{O}_{3-\delta}$ , ( $0 \leq x \leq 0.4$ )

Figure 4.5 illustrates the electrical conductivity of the  $\text{Ca}^{2+}$  ion substituted in the A-site of BSCF specimens measured at 300-750°C. The electrical conductivity increased with increasing amount of the  $\text{Ca}^{2+}$  substitution; the dense microstructure can contribute to an increase of the bulk conductivity. Furthermore, the increasing of  $\text{Ca}^{2+}$  ion gave the small lattice parameter leading to the fast migration of the electron between cation and oxygen ion in the lattice [41]. Thus the electrical conductivity was increased. The maximum conductivity was  $96 \text{ S}\cdot\text{cm}^{-1}$  at 650°C for BSCCF with  $x = 0.3$ . However, the composition of  $\text{Ca}^{2+}$  ion-substitution greater than  $x = 0.3$  presented a decrease in the electrical conductivity, which could be caused by the distortion in the perovskite structure and/or the appearance of the second phase. The electrical conductivity values were summarized in Table 4.3.

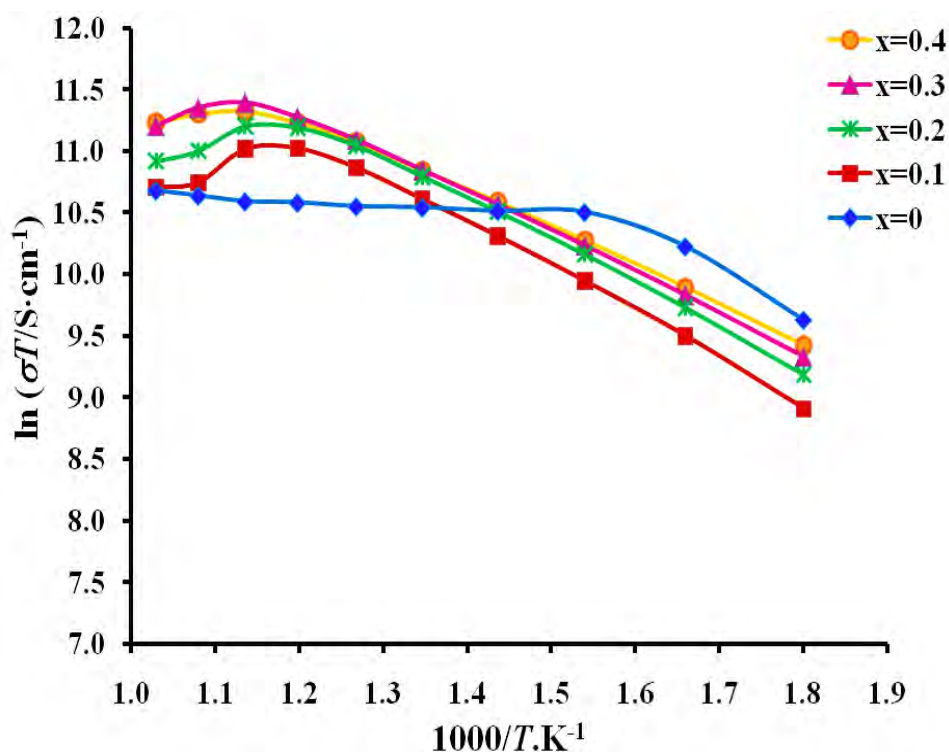


**Figure 4.5** The electrical conductivity of  $(\text{Ba}_{0.5}\text{Sr}_{0.5})_{1-x}\text{Ca}_x\text{Co}_{0.8}\text{Fe}_{0.2}\text{O}_{3-\delta}$ , ( $0 \leq x \leq 0.4$ ) at 300°C to 750°C.

**Table 4.3** The electrical conductivity values of  $(\text{Ba}_{0.5}\text{Sr}_{0.5})_{1-x}\text{Ca}_x\text{Co}_{0.8}\text{Fe}_{0.2}\text{O}_{3-\delta}$ , ( $0 \leq x \leq 0.4$ ) at various temperatures

Sample	Temperature (°C)						$\sigma_{\text{max.}}$ $\text{S}\cdot\text{cm}^{-1}$ (°C)
	300	400	500	600	700	800	
x = 0.0	26.57	54.28	49.04	45.19	42.89	42.47	54.28 (400)
x = 0.1	23.70	45.48	59.30	70.66	53.34	49.87	79.48 (600)
x = 0.2	17.05	38.62	63.25	83.36	61.79	53.02	83.36 (600)
x = 0.3	19.75	41.47	66.50	90.49	87.75	68.74	96.44 (650)
x = 0.4	21.64	43.29	66.46	86.54	83.34	70.32	89.99 (650)

#### 4.1.4 Temperature program desorption of $(\text{Ba}_{0.5}\text{Sr}_{0.5})_{1-x}\text{Ca}_x\text{Co}_{0.8}\text{Fe}_{0.2}\text{O}_{3-\delta}$ , ( $0 \leq x \leq 0.4$ )

Figure 4.6 shows the desorption of oxygen on the perovskite membranes at various temperature. It has been known that there are three type of oxygen desorption: oxygen desorption on the surface ( $<300^\circ\text{C}$ ,  $\alpha\text{-O}_2$ ), oxygen in oxygen vacancy ( $400\text{-}600^\circ\text{C}$ ,  $\beta\text{-O}_2$ ) and oxygen lost from the lattice of perovskite ( $600\text{-}800^\circ\text{C}$ ,  $\gamma\text{-O}_2$ ). Peak areas of oxygen desorption are summarized in Table 4.4. It was found that BSCF was mainly composed of  $\beta\text{-O}_2$  and minor in  $\gamma\text{-O}_2$ . After substituted the  $\text{Ca}^{2+}$  ions in A-site, BSCCF was still mainly presented  $\beta\text{-O}_2$  but also slightly increased in  $\gamma\text{-O}_2$ . The results may be explained by the substitution of  $\text{Ca}^{2+}$  ion in  $\text{Ba}^{2+}$  and  $\text{Sr}^{2+}$  ions giving the smaller lattice that can induced the attractive force between the A-site cation and the oxygen ion in the lattice to increase. Thus, the attractive force between the B-site cations and oxygen ions were decreased, causing the loss of oxygen ions bonded with the B-site cations from the lattice structure. In addition, at the 40 mol% of  $\text{Ca}^{2+}$  ion, the peak area was decreased, suggesting the effect of impurity phase that present in the materials.

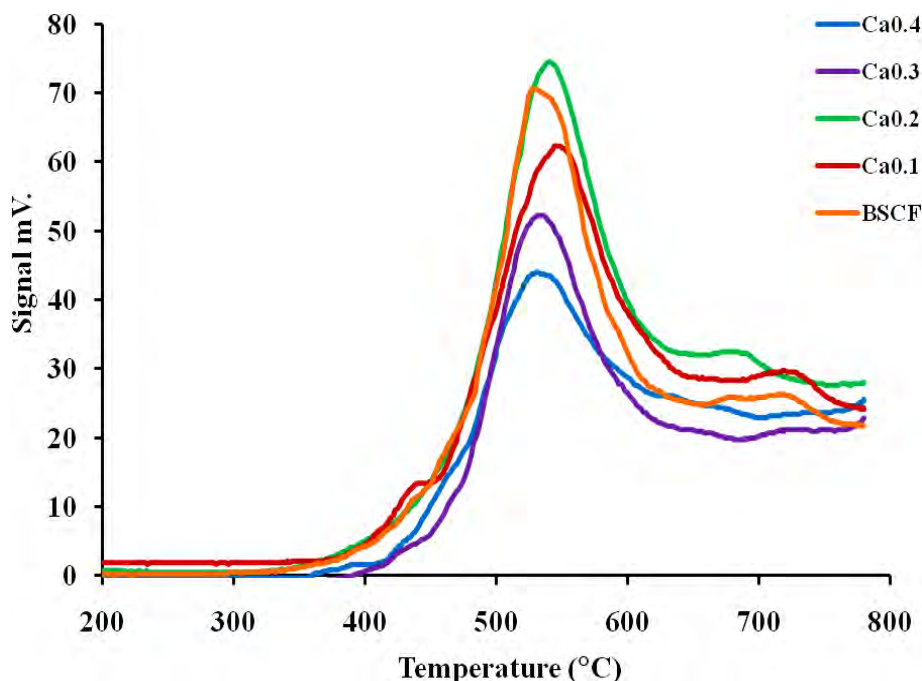


**Figure 4.6** Oxygen temperature programmed desorption curves of  $(\text{Ba}_{0.5}\text{Sr}_{0.5})_{1-x}\text{Ca}_x\text{Co}_{0.8}\text{Fe}_{0.2}\text{O}_{3-\delta}$ , ( $0 \leq x \leq 0.4$ ) at  $200^\circ\text{C}$  to  $800^\circ\text{C}$ .



**Table 4.4** Oxygen desorption peak area of  $(\text{Ba}_{0.5}\text{Sr}_{0.5})_{1-x}\text{Ca}_x\text{Co}_{0.8}\text{Fe}_{0.2}\text{O}_{3-\delta}$ ,  
( $0 \leq x \leq 0.4$ )

Samples	Peak area(/0.1g)
x = 0.0	46,242
x = 0.1	52,515
x = 0.2	55,233
x = 0.3	61,755
x = 0.4	38,292

#### 4.1.5 Thermal expansion of $(\text{Ba}_{0.5}\text{Sr}_{0.5})_{1-x}\text{Ca}_x\text{Co}_{0.8}\text{Fe}_{0.2}\text{O}_{3-\delta}$ , ( $0 \leq x \leq 0.4$ )

The expansion curves of the partial substitution of  $\text{Ca}^{2+}$  ion in A-site of BSCF are shown in Figure 4.7. The thermal expansion of primitive BSCF was increased with the increasing of the temperature. With the partial substitution of dopant ( $\text{Ca}^{2+}$  ion) in the A-site structure there were no differences in thermal expansion of BSCCF. It was because the partial substitution of the  $\text{Ca}^{2+}$  ions which has the same valence state did not make the difference in the attractive force in the lattice. The TEC values of BSCCF were calculated from the slope of the curves as be summarized in Table 4.5. However at the high content of  $\text{Ca}^{2+}$  ion (40 mol%), the abnormal curve was observed at high temperature (600°C-700°C), indicating a distortion of perovskite structure.

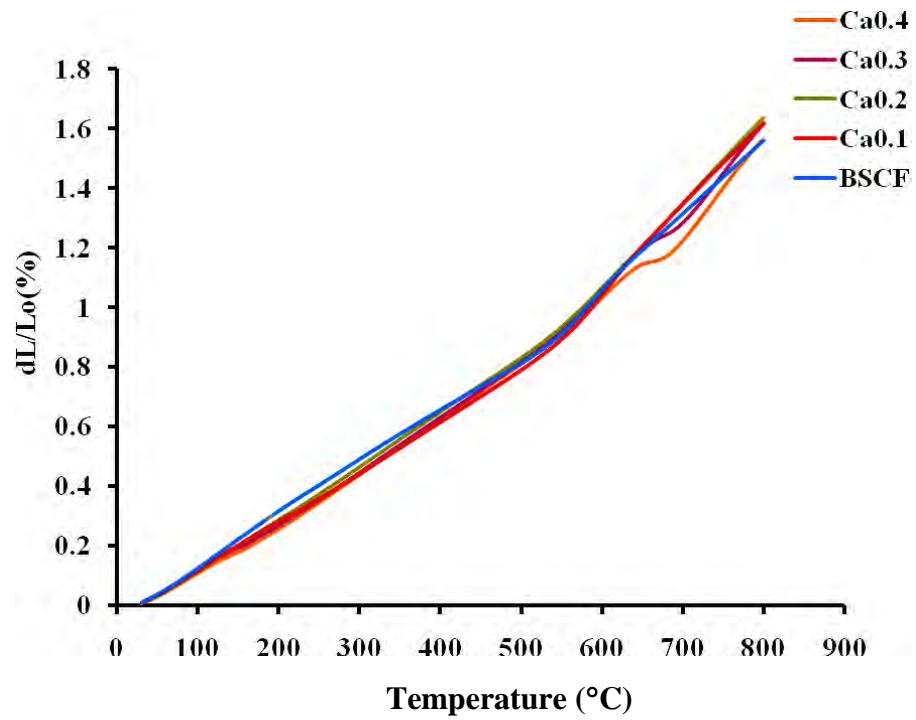


**Figure 4.7** Thermal expansion curves of Ca-doped A-site of  $(\text{Ba}_{0.5}\text{Sr}_{0.5})_{1-x}\text{Ca}_x\text{Co}_{0.8}\text{Fe}_{0.2}\text{O}_{3-\delta}$  ( $0 \leq x \leq 0.4$ ) at  $50^\circ\text{C}$  to  $800^\circ\text{C}$ .

**Table 4.5** Thermal expansion coefficients of BSCCF specimens at  $50^\circ\text{C}$ - $800^\circ\text{C}$

Samples	TEC ( $\times 10^{-6} \cdot ^\circ\text{C}^{-1}$ )
x = 0.0	20.375
x = 0.1	21.122
x = 0.2	21.459
x = 0.3	21.115
x = 0.4	20.478

## 4.2 Preparation and properties of $(\text{Ba}_{0.5}\text{Sr}_{0.5})_{0.8}\text{La}_{0.2-x}\text{Ca}_x\text{Co}_{0.8}\text{Fe}_{0.2}\text{O}_{3-\delta}$ (BSLCCF), $(0 \leq x \leq 0.15)$ perovskite oxide.

### 4.2.1 Phase formation of $(\text{Ba}_{0.5}\text{Sr}_{0.5})_{0.8}\text{La}_{0.2-x}\text{Ca}_x\text{Co}_{0.8}\text{Fe}_{0.2}\text{O}_{3-\delta}$ perovskite

In the case of concurrent doping of  $\text{Ca}^{2+}$  and  $\text{La}^{3+}$  ions in the A-site of BSCF, the XRD patterns of powder and sintered samples are shown in Figures 4.8 and 4.9, respectively. The calcined and sintered compounds showed the pure single phase of cubic  $\text{ABO}_3$  perovskite-type structure with a space group of  $Pm\bar{3}m$ . The incorporation of  $\text{La}^{3+}$  ions in the A- site of BSCF resulted in a gradual shift of the reflection peak of BSLCF to the higher angle, corresponding to a shrinkage in the crystal structure due to the substitution of the lower ionic radius of  $\text{La}^{3+}$  ion (0.136 nm) in the  $\text{Ba}^{2+}$  ion (0.161 nm) and  $\text{Sr}^{2+}$  ion (0.144 nm). On the other hand, the increasing substitution of  $\text{Ca}^{2+}$  ions in  $\text{La}^{3+}$  ion site in BSCF made the XRD patterns of these samples gradually moved to the lower angle. This phenomenon was the cause of the expansion of the lattice parameter and crystallite size in Table 4.6. The results can be explained by the lower valence state of  $\text{Ca}^{2+}$  ion having the ionic force lower than that of  $\text{La}^{3+}$  ion, then the distances between the cations and the oxide ions in the lattice are longer causing the expansion of crystal.

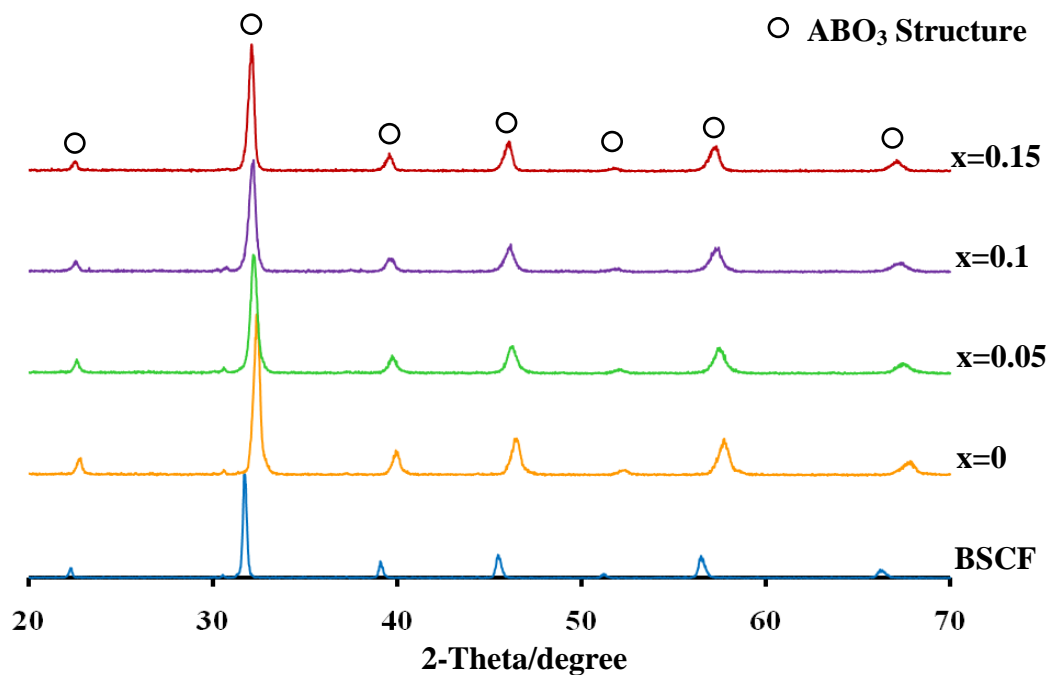


**Figure 4.8** XRD patterns of  $(\text{Ba}_{0.5}\text{Sr}_{0.5})_{0.8}\text{La}_{0.2-x}\text{Ca}_x\text{Co}_{0.8}\text{Fe}_{0.2}\text{O}_{3-\delta}$ , ( $0 \leq x \leq 0.15$ ) powder after calcined at  $1000^\circ\text{C}$  for 5 hrs.

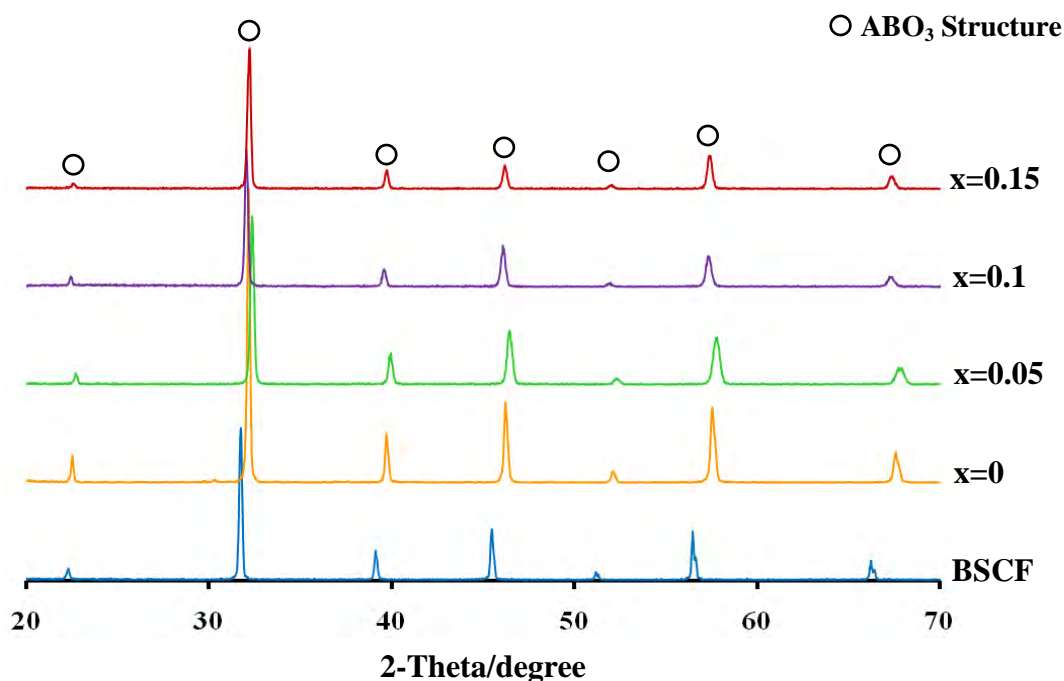


**Figure 4.9** XRD patterns of  $(\text{Ba}_{0.5}\text{Sr}_{0.5})_{0.8}\text{La}_{0.2-x}\text{Ca}_x\text{Co}_{0.8}\text{Fe}_{0.2}\text{O}_{3-\delta}$ , ( $0 \leq x \leq 0.15$ ) membranes after sintered at  $1100^\circ\text{C}$  for 10 hrs.

**Table 4.6** Lattice parameters of  $(\text{Ba}_{0.5}\text{Sr}_{0.5})_{0.8}\text{La}_{0.2-x}\text{Ca}_x\text{Co}_{0.8}\text{Fe}_{0.2}\text{O}_{3-\delta}$  ( $0 \leq x \leq 0.15$ ) powder after calcined

<b>Samples</b>	<b>Lattice Parameter (nm)</b>
x = 0.00	0.392 (1)
x = 0.05	0.393 (3)
x = 0.10	0.393 (7)
x = 0.15	0.394 (3)

#### **4.2.2. The surface morphology of $(\text{Ba}_{0.5}\text{Sr}_{0.5})_{0.8}\text{La}_{0.2-x}\text{Ca}_x\text{Co}_{0.8}\text{Fe}_{0.2}\text{O}_{3-\delta}$ , BSLCF ( $0 \leq x \leq 0.15$ )**

Figure 4.10 shows the surface morphology of BSLCCF specimens partially substituted by  $\text{Ca}^{2+}$  and  $\text{La}^{2+}$  ions. The dense microstructure of the samples was obtained with the increasing of  $\text{Ca}^{2+}$  ion content and concurrently decreasing of  $\text{La}^{3+}$  ion content. It can be attributed to the increasing of crystallite size resulting in bigger grain size of specimens. In addition the homogeneous distribution of  $\text{La}^{3+}$  and  $\text{Ca}^{2+}$  ions were observed by EDX technique, as shown in Figure 4.11. The relative density was measured by Archimedes method and progressively increased with the increasing of  $\text{Ca}^{2+}$  ion content, as summarized in Table 4.7.

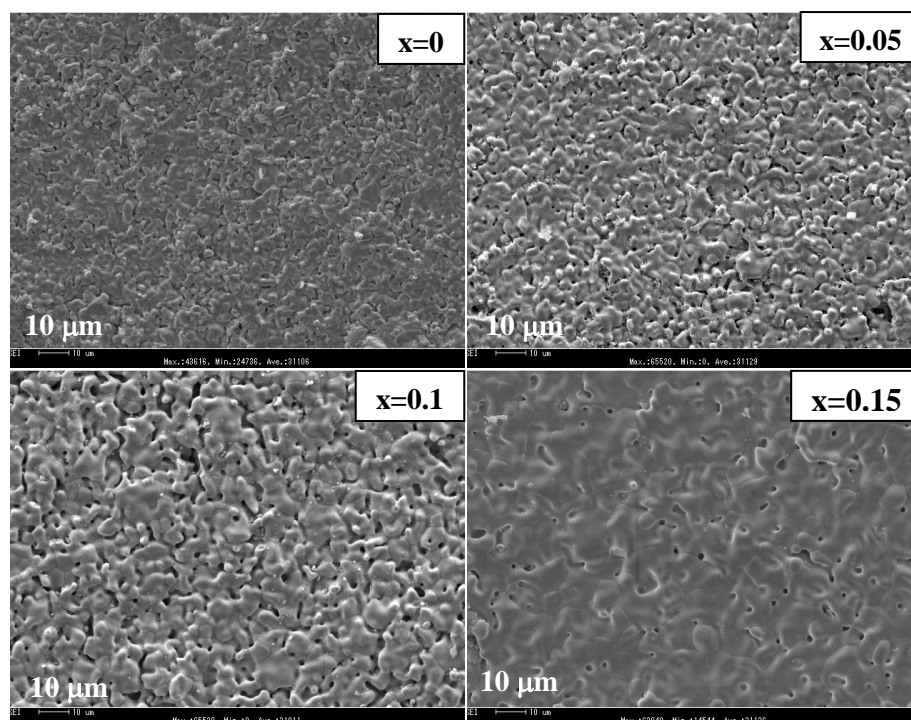


**Figure 4.10** SEM micrographs of  $(\text{Ba}_{0.5}\text{Sr}_{0.5})_{0.8}\text{La}_{0.2-x}\text{Ca}_x\text{Co}_{0.8}\text{Fe}_{0.2}\text{O}_{3-\delta}$ , ( $0 \leq x \leq 0.15$ ) after sintered at  $1100^\circ\text{C}$  for 10 hrs.

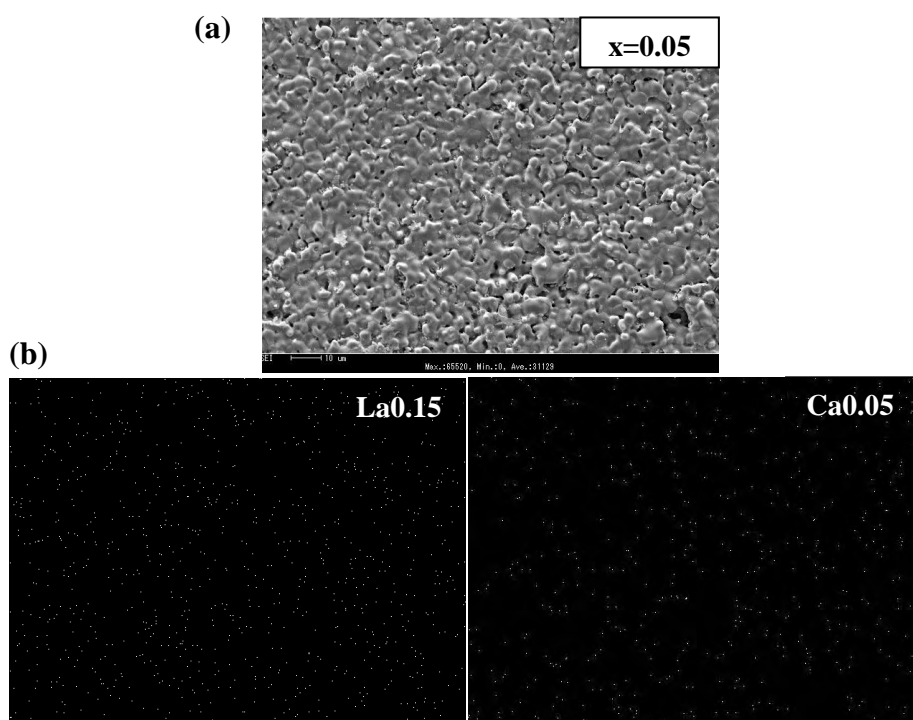


**Figure 4.11** Surface morphology (a) and elemental mapping (b) of  $(\text{Ba}_{0.5}\text{Sr}_{0.5})_{0.8}\text{La}_{0.2-x}\text{Ca}_x\text{Co}_{0.8}\text{Fe}_{0.2}\text{O}_{3-\delta}$ , ( $0.05 \leq x \leq 0.15$ ) discs.

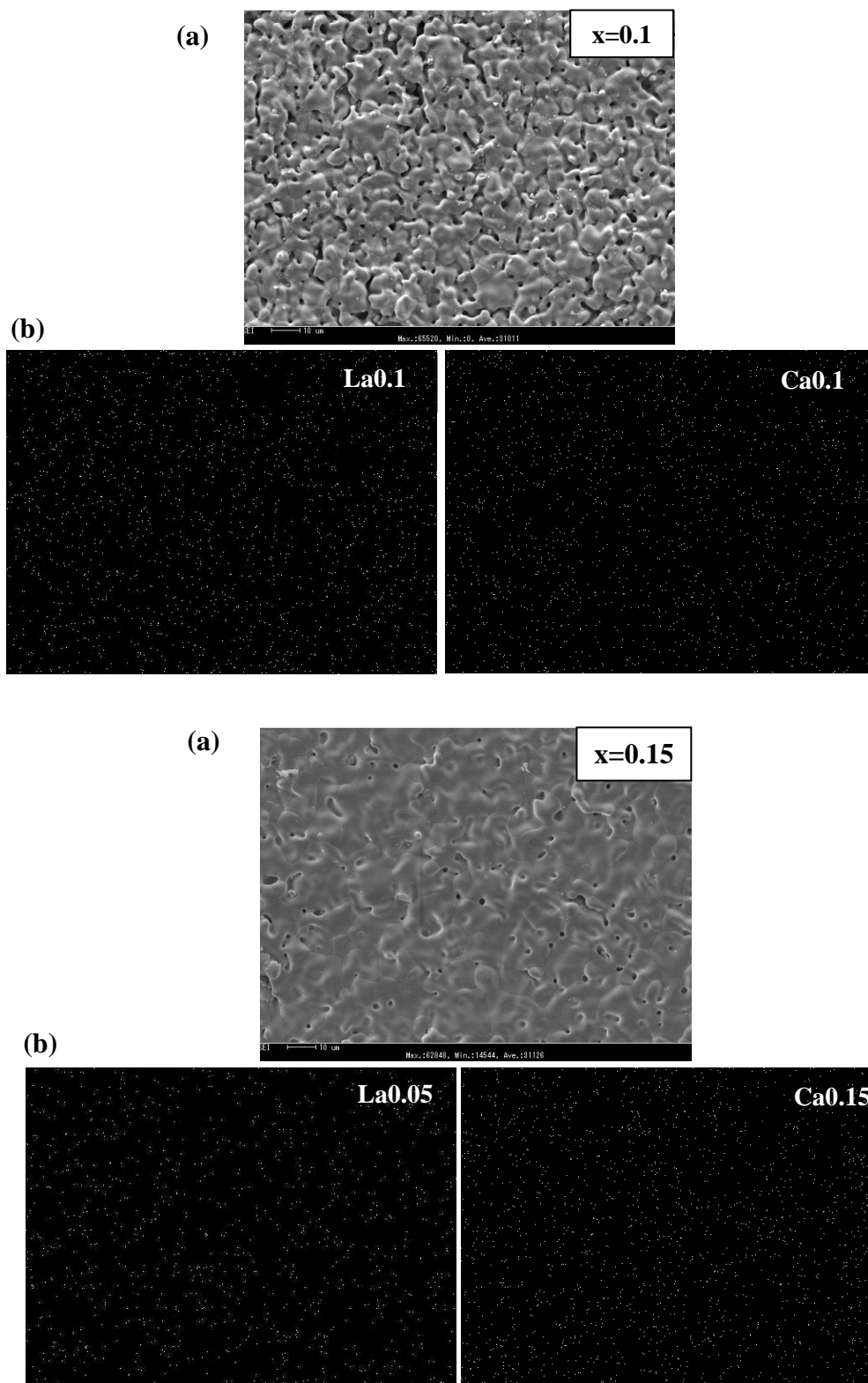


**Figure 4.11 cont.** Surface morphology (a) and elemental mapping (b) of  $(\text{Ba}_{0.5}\text{Sr}_{0.5})_{0.8}$

$\text{La}_{0.2-x}\text{Ca}_x\text{Co}_{0.8}\text{Fe}_{0.2}\text{O}_{3-\delta}$ , ( $0.05 \leq x \leq 0.15$ ) discs

**Table 4.7** The relative density of  $(\text{Ba}_{0.5}\text{Sr}_{0.5})_{0.8}\text{La}_{0.2-x}\text{Ca}_x\text{Co}_{0.8}\text{Fe}_{0.2}\text{O}_{3-\delta}$ ,  
( $0 \leq x \leq 0.15$ )

<b>Samples</b>	<b>Relative density (%)</b>
BSLCCF ( $x = 0.00$ )	76.70
$x = 0.05$	78.98
$x = 0.10$	87.23
$x = 0.15$	98.41

**4.2.3 Electrical Conductivity of  $(\text{Ba}_{0.5}\text{Sr}_{0.5})_{0.8}\text{La}_{0.2-x}\text{Ca}_x\text{Co}_{0.8}\text{Fe}_{0.2}\text{O}_{3-\delta}$ ,  
( $0 \leq x \leq 0.15$ )**

Figure 4.12 reveals the electrical conductivity of BSLCCF at 300°C to 750°C. The electrical conductivity of BSLCCF decreased with increasing  $\text{Ca}^{2+}$  ion content. Although the substitution of  $\text{Ca}^{2+}$  ions led to higher densities of the sintered samples, the reducing of  $\text{La}^{3+}$  ion content might play a role for a decrease of electrical conductivity. It is because doping of  $\text{La}^{3+}$  ions in the A-site not only promotes the n-type small polarons but also promotes the oxygen vacancy from the charge compensation of Co and Fe ions at the B-site which benefits to the increase in the ionic conductivity. The trend of the electrical conductivity was summarized in Table 4.8.



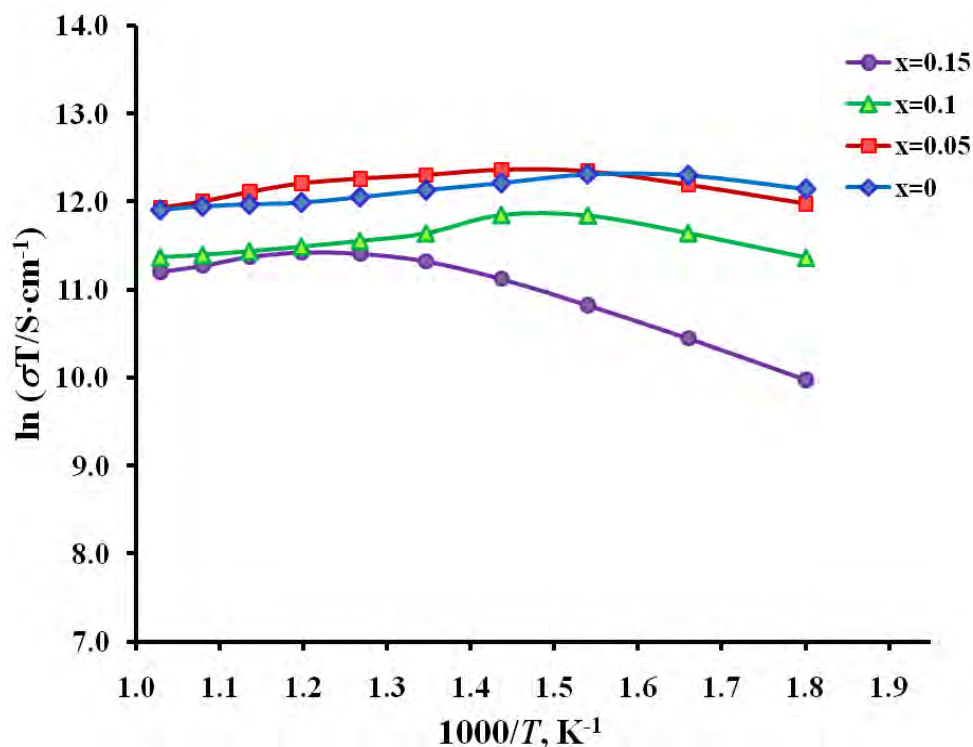


**Figure 4.12** The electrical conductivity of  $(\text{Ba}_{0.5}\text{Sr}_{0.5})_{0.8}\text{La}_{0.2-x}\text{Ca}_x\text{Co}_{0.8}\text{Fe}_{0.2}\text{O}_{3-\delta}$ , ( $0 \leq x \leq 0.15$ ) at 300°C to 750°C.

**Table 4.8** The electrical conductivity of  $(\text{Ba}_{0.5}\text{Sr}_{0.5})_{0.8}\text{La}_{0.2-x}\text{Ca}_x\text{Co}_{0.8}\text{Fe}_{0.2}\text{O}_{3-\delta}$ , ( $0 \leq x \leq 0.15$ ) at various temperatures

Sample	Temperature (°C)						$\sigma_{\text{max.}}$ $\text{S}\cdot\text{cm}^{-1}$ (°C)
	300	400	500	600	700	800	
BSCF	26.57	54.28	49.04	45.19	42.89	42.47	54.28 (400)
x = 0.00	329.14	330.86	240.77	185.29	159.42	133.03	352.98 (350)
x = 0.05	278.37	341.05	284.83	229.44	167.78	135.79	341.05 (400)
x = 0.10	150.30	207.96	147.31	111.89	91.30	79.28	207.96 (400)
x = 0.15	37.62	74.67	107.27	104.89	80.92	67.88	109.79 (550)

#### 4.2.4 Temperature programmed desorption of $(\text{Ba}_{0.5}\text{Sr}_{0.5})_{0.8}\text{La}_{0.2-x}\text{Ca}_x\text{Co}_{0.8}\text{Fe}_{0.2}\text{O}_{3-\delta}$ , $(0 \leq x \leq 0.15)$

The oxygen desorption of the concurrently doped  $\text{Ca}^{2+}$  ion and  $\text{La}^{3+}$  ion in site of BSCF samples was shown in Figure 4.13. The oxygen desorption of doping the  $\text{La}^{3+}$  ion in A-site of BSCF still mainly presented the  $\beta\text{-O}_2$  from the oxygen vacancies that was the same trend in the primitive BSCF. However, the substitution of  $\text{La}^{3+}$  ion in A-site of BSCF induced the increasing of  $\gamma\text{-O}_2$  in the lattice because the B-site cations ( $\text{Co}^{4+}$  and  $\text{Fe}^{4+}$  ions) were reduced by the charge compensation of  $\text{La}^{3+}$  ion. Thus the oxygen ions in the lattice easily lost from the lattice higher than in BSCF. In addition, the substitution of  $\text{Ca}^{2+}$  ion in  $\text{La}^{3+}$  ion still presented the majority in  $\beta\text{-O}_2$  but the  $\gamma\text{-O}_2$  was decreased followed the increasing of  $\text{Ca}^{2+}$  ion content. The result was affected from the reducing of  $\text{La}^{3+}$  ion content, led to the reduction of B-site cation so the oxygen ion loss from the lattice were decreased. Consequently, the ionic conductivity of material was decreased which was corresponding to the electrical conductivity results. The peak areas of the increasing  $\text{Ca}^{2+}$  ion content in BSLCF were shown in Table 4.9.

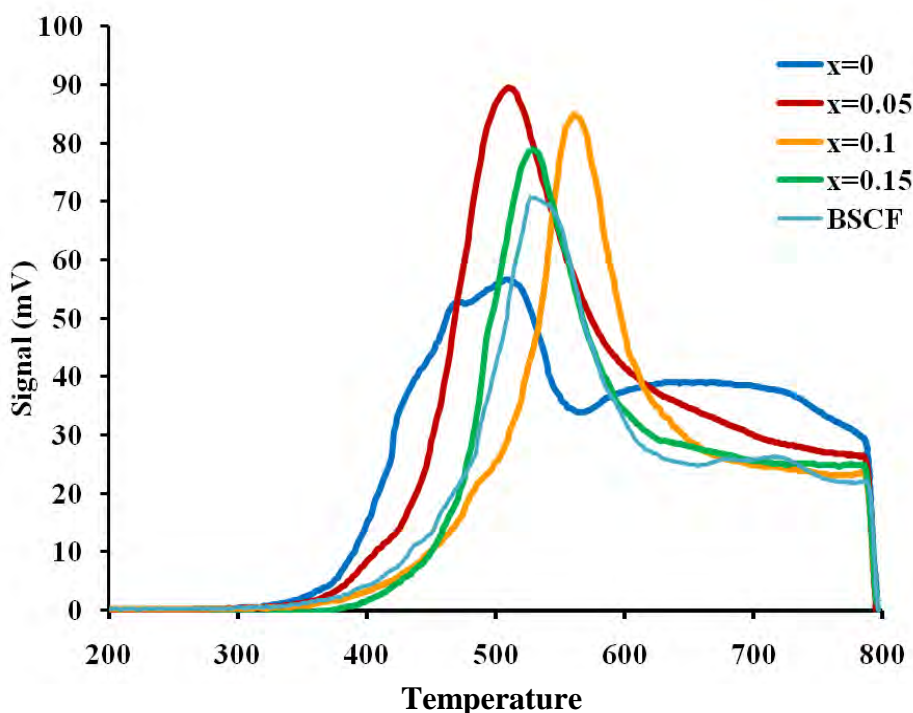


**Figure 4.13** Oxygen temperature programmed desorption curves of  $(\text{Ba}_{0.5}\text{Sr}_{0.5})_{0.8}\text{La}_{0.2-x}\text{Ca}_x\text{Co}_{0.8}\text{Fe}_{0.2}\text{O}_{3-\delta}$ ,  $(0 \leq x \leq 0.15)$  at 200°C to 800°C.

**Table 4.9** Oxygen desorption peak area of BSCF,  $(\text{Ba}_{0.5}\text{Sr}_{0.5})_{0.8}\text{La}_{0.2-x}\text{Ca}_x\text{Co}_{0.8}\text{Fe}_{0.2}\text{O}_{3-\delta}$ , ( $0 \leq x \leq 0.15$ )

<b>Samples</b>	<b>Peak area (/0.1g)</b>
BSCF	46,242
x = 0.00	63,185
x = 0.05	58,631
x = 0.10	58,574
x = 0.15	38,966

**4.2.5 Thermal expansion of  $(\text{Ba}_{0.5}\text{Sr}_{0.5})_{0.8}\text{La}_{0.2-x}\text{Ca}_x\text{Co}_{0.8}\text{Fe}_{0.2}\text{O}_{3-\delta}$ , ( $0 \leq x \leq 0.15$ )**

Figure 4.14 shows the thermal expansion of BSCF after substituted with  $\text{La}^{3+}$  and  $\text{Ca}^{2+}$  ions in A-site. It was found that the substitute ion of  $\text{La}^{3+}$  made the thermal expansion increased because the substitution of  $\text{La}^{3+}$  ion promoted the oxygen vacancies by charge compensation of  $\text{Co}^{4+}$  and  $\text{Fe}^{4+}$  ions at B-site to the lower valence state ( $\text{Co}^{3+}$  and  $\text{Fe}^{3+}$  ions). Thus, oxygen vacancies were a cause of expansion in the materials when they were heated. In addition, the substitution of  $\text{La}^{3+}$  ion by  $\text{Ca}^{2+}$  ion would decreased the reduction of B-site cations ( $\text{Co}^{4+}$  and  $\text{Fe}^{4+}$  ions) to the lower valence state, then the oxygen vacancies were decreased leading to the decreasing of thermal expansion in material, as summarized in Table 4.10. The TEC values were calculated from slopes of the thermal expansion curves.

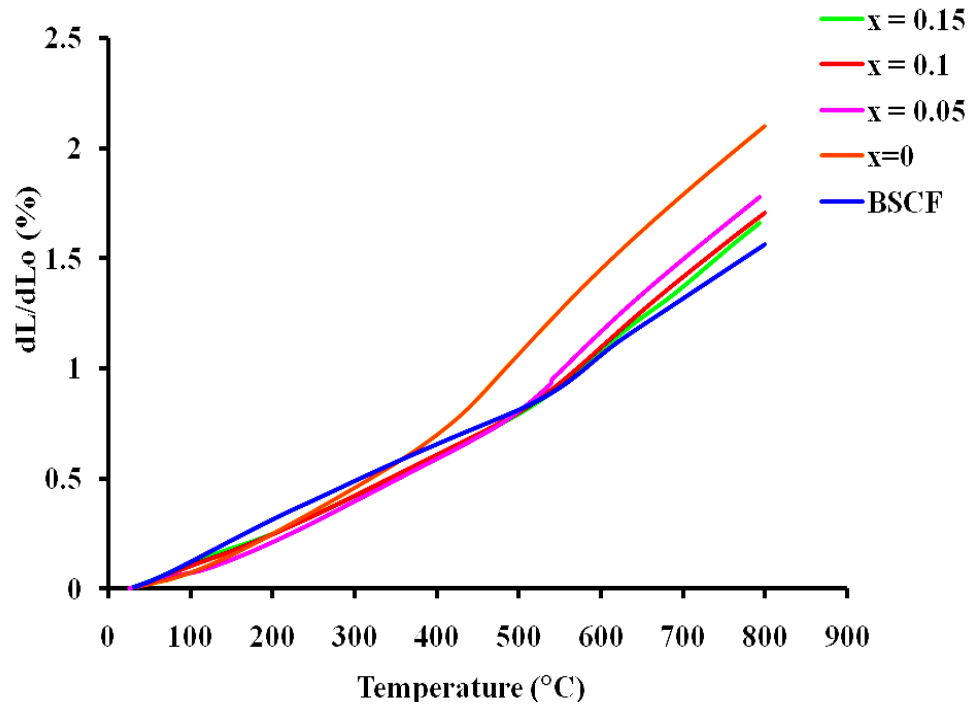


**Figure 4.14** Thermal expansion curves of  $(\text{Ba}_{0.5}\text{Sr}_{0.5})_{0.8}\text{La}_{0.2-x}\text{Ca}_x\text{Co}_{0.8}\text{Fe}_{0.2}\text{O}_{3-\delta}$  ( $0 \leq x \leq 0.15$ ) at  $50^\circ\text{C}$  to  $800^\circ\text{C}$ .

**Table 4.10** Thermal expansion coefficients of BSLCCF specimens at  $50^\circ\text{C}$  to  $800^\circ\text{C}$

Samples	TEC ( $\times 10^{-6} \cdot ^\circ\text{C}^{-1}$ )
x = 0.00	27.746
x = 0.05	23.628
x = 0.10	22.313
x = 0.15	21.906

### 4.3 Preparation and properties of $(\text{Ba}_{0.5}\text{Sr}_{0.5})_{0.8}\text{La}_{0.2}\text{Co}_{0.8}\text{Fe}_{0.2}\text{Ca}_x\text{O}_{3-\delta}$ (BSLFCa), $(0 \leq x \leq 0.05)$ perovskite oxide.

#### 4.3.1 Phase formation of $(\text{Ba}_{0.5}\text{Sr}_{0.5})_{0.8}\text{La}_{0.2}\text{Co}_{0.8}\text{Fe}_{0.2}\text{Ca}_x\text{O}_{3-\delta}$ perovskite.

Figure 4.15 indicates the XRD patterns of the addition of  $\text{Ca}^{2+}$  ion in BSLCF not only incorporated the single phase of perovskite structure but the lattice parameter also slightly increased without the structural change [9]. The position of the reflection peaks did not change indicating that the  $\text{Ca}^{2+}$  ion could incorporate into interstitial site in the lattice structure and maintained the cubic structure by expanding the lattice parameter as shown in Table 4.11. However for the  $\text{Ca}^{2+}$  ion content higher than 1 mol%, the reflection peaks of material were broad, which may be caused by distortion of perovskite structure when the  $\text{Ca}^{2+}$  ions were added in BSLCF. After sintering, the 1 mol%  $\text{Ca}^{2+}$  ion sample showed the single phase of cubic perovskite structure as shown in Figure 4.16.

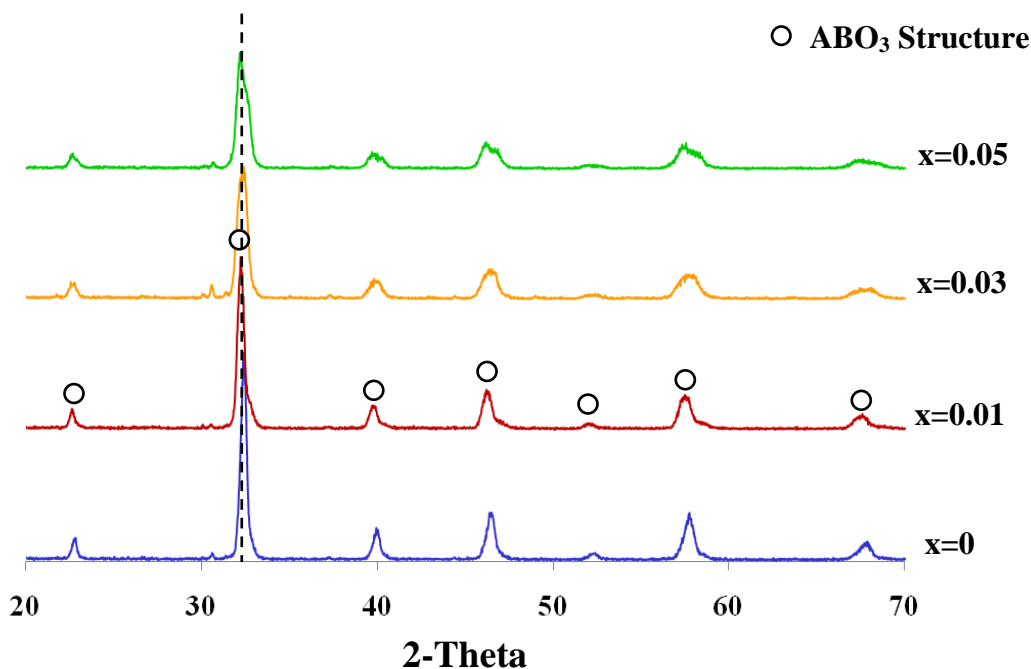


**Figure 4.15** XRD patterns of  $(\text{Ba}_{0.5}\text{Sr}_{0.5})_{0.8}\text{La}_{0.2}\text{Co}_{0.8}\text{Fe}_{0.2}\text{Ca}_x\text{O}_{3-\delta}$ ,  $(0 \leq x \leq 0.05)$  powder after calcined at  $1000^\circ\text{C}$  for 5 hrs.

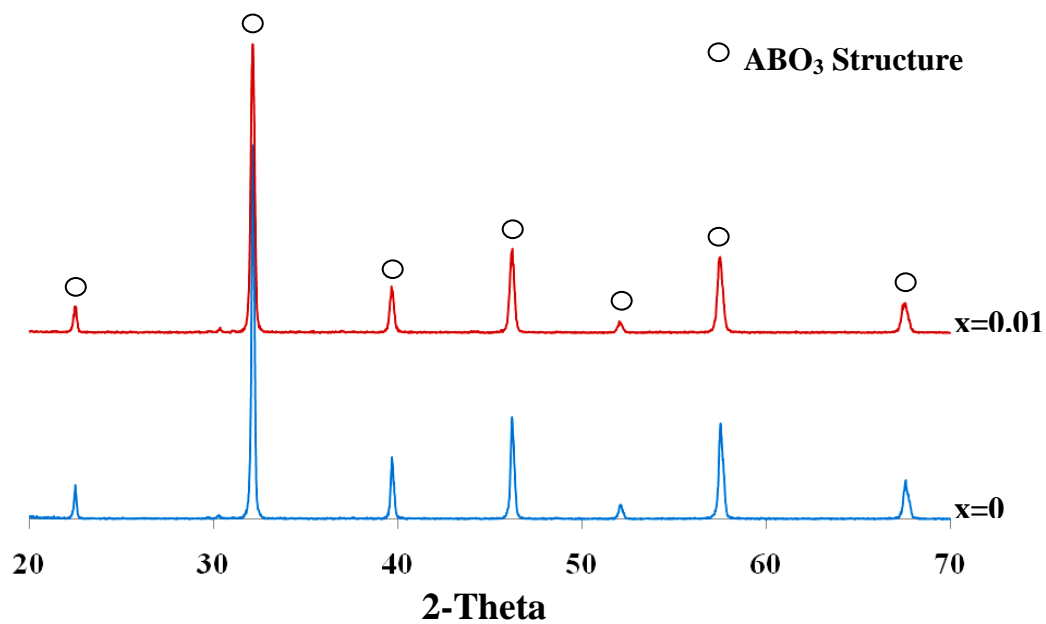


**Figure 4.16** XRD patterns of  $(\text{Ba}_{0.5}\text{Sr}_{0.5})_{0.8}\text{La}_{0.2}\text{Co}_{0.8}\text{Fe}_{0.2}\text{Ca}_x\text{O}_{3-\delta}$ , and  $(\text{Ba}_{0.5}\text{Sr}_{0.5})_{0.8}\text{La}_{0.2}\text{Co}_{0.8}\text{Fe}_{0.2}\text{Ca}_x\text{Ca}_{0.01}\text{O}_{3-\delta}$  ( $0 \leq x \leq 0.05$ ) disc after sintered at  $1100^\circ\text{C}$  for 10 hrs.

**Table 4.11** Lattice parameter of  $(\text{Ba}_{0.5}\text{Sr}_{0.5})_{0.8}\text{La}_{0.2}\text{Co}_{0.8}\text{Fe}_{0.2}\text{Ca}_x\text{O}_{3-\delta}$ ,  $x = 0$  and  $0.01$  after calcined at  $1000^\circ\text{C}$  for 5 hrs

Samples	Lattice Parameter (nm)
$x = 0.00$	0.391(5)
$x = 0.01$	0.392(4)

### 4.3.2. The surface morphology of $(\text{Ba}_{0.5}\text{Sr}_{0.5})_{0.8}\text{La}_{0.2}\text{Co}_{0.8}\text{Fe}_{0.2}\text{Ca}_x\text{O}_{3-\delta}$ , BSLCFCa ( $x = 0$ and $0.01$ )

The surface morphology in Figure 4.17 reveals that the addition of  $\text{Ca}^{2+}$  ions in A-site of BSLCF gave bigger grain size that according to the increasing of crystallite size from XRD result and the density was also increased as shown in Table 4.12. However, the  $\text{Ca}^{2+}$  ion in the material could be confirmed by the elemental mapping analysis which indicated the presence of homogeneous distribution of  $\text{Ca}^{2+}$  ion in the BSCCF as shown in Figure 4.18. Moreover, the higher density was the advantage of material for electrons hopping in the bulk of material, thus the electronic conductivity of material was increased.

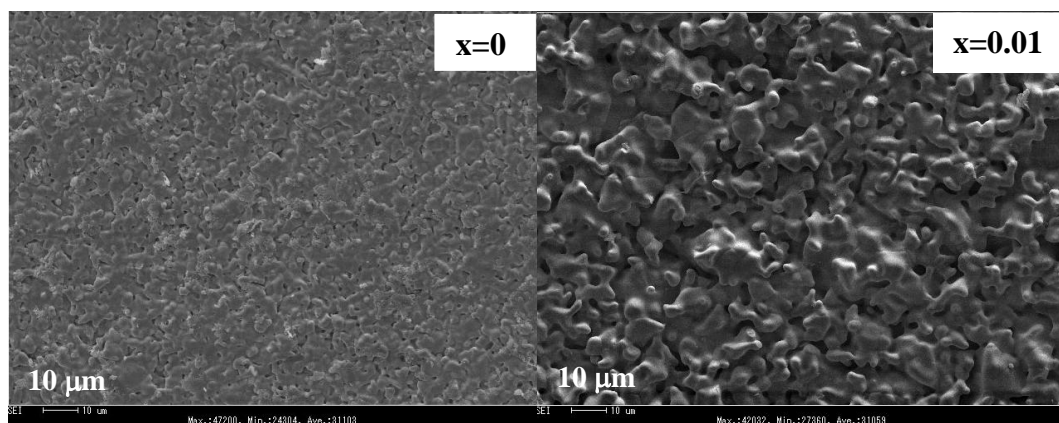


**Figure 4.17** SEM micrographs of  $(\text{Ba}_{0.5}\text{Sr}_{0.5})_{0.8}\text{La}_{0.2}\text{Co}_{0.8}\text{Fe}_{0.2}\text{Ca}_x\text{O}_{3-\delta}$ , ( $x = 0$  and  $0.01$ ) after sintered at  $1100^\circ\text{C}$  for 10 hrs.

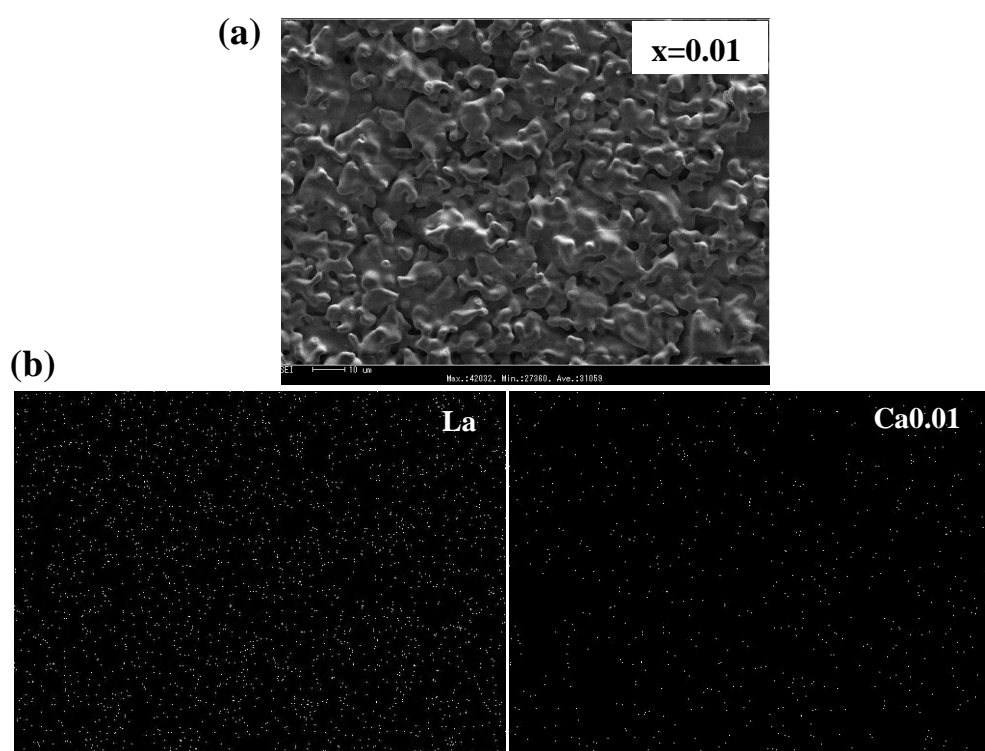


**Figure 4.18** Surface morphology (a) and elemental mapping (b) of  $(\text{Ba}_{0.5}\text{Sr}_{0.5})_{0.8}\text{La}_{0.2-x}\text{Ca}_x\text{Co}_{0.8}\text{Fe}_{0.2}\text{O}_{3-\delta}$  disc,  $x = 0.01$

**Table 4.12** Relative density of  $(\text{Ba}_{0.5}\text{Sr}_{0.5})_{0.8}\text{La}_{0.2}\text{Co}_{0.8}\text{Fe}_{0.2}\text{Ca}_x\text{O}_{3-\delta}$ , ( $x = 0$  and  $0.01$ )

Samples	Relative density
	(%)
$x = 0.00$	76.70
$x = 0.01$	91.48



### 4.3.3 Electrical Conductivity of $(\text{Ba}_{0.5}\text{Sr}_{0.5})_{0.8}\text{La}_{0.2}\text{Co}_{0.8}\text{Fe}_{0.2}\text{Ca}_x\text{O}_{3-\delta}$ , ( $x = 0$ and $0.01$ )

For the incorporation of  $\text{Ca}^{2+}$  ions in the A-site of BSLCF in Figure 4.19 and the electrical conductivity values that shown in Table 4.13, the conductivity was found to be increased from around  $353 \text{ S}\cdot\text{cm}^{-1}$  of BSLCF to the maximum conductivity about  $593 \text{ S}\cdot\text{cm}^{-1}$  at  $350^\circ\text{C}$ . Moreover, the addition of  $\text{Ca}^{2+}$  ions in BSLCF resulted in the expansion of the lattice volume which benefits for oxygen to transfer through the lattice, thus the reduction of oxygen to oxide ion was increased and the electrical conductivity was increased.

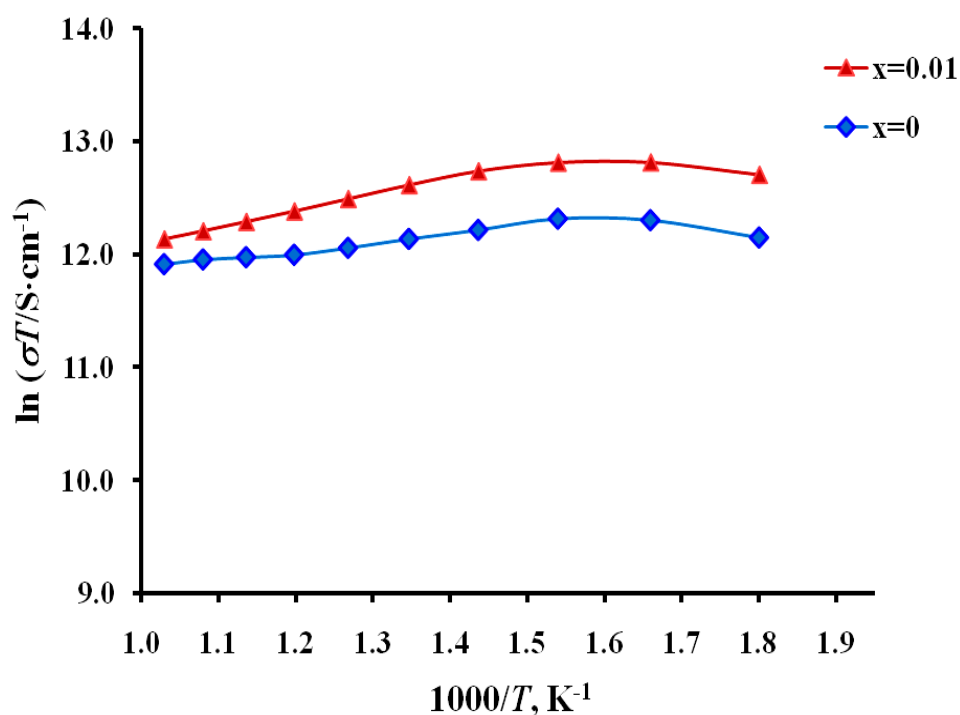


**Figure 4.19** The electrical conductivity of  $(\text{Ba}_{0.5}\text{Sr}_{0.5})_{0.8}\text{La}_{0.2}\text{Co}_{0.8}\text{Fe}_{0.2}\text{Ca}_x\text{O}_{3-\delta}$ ,  
( $x = 0$  and  $0.01$ ) at  $300^\circ\text{C}$  to  $750^\circ\text{C}$ .

**Table 4.13** The electrical conductivity of  $(\text{Ba}_{0.5}\text{Sr}_{0.5})_{0.8}\text{La}_{0.2}\text{Co}_{0.8}\text{Fe}_{0.2}\text{Ca}_x\text{O}_{3-\delta}$ ,  
( $x = 0$  and  $0.01$ ) at various temperature

Sample	Temperature (°C)						$\sigma_{\text{max.}}$ $\text{S}\cdot\text{cm}^{-1}$ (°C)
	300	400	500	600	700	800	
$x = 0.00$	329.14	330.86	240.77	185.29	159.42	133.03	352.98 (350)
$x = 0.01$	577.55	547.80	390.14	273.24	205.38	163.29	592.65 (350)

#### 4.3.3 Temperature programmed desorption of $(\text{Ba}_{0.5}\text{Sr}_{0.5})_{0.8}\text{La}_{0.2}\text{Co}_{0.8}\text{Fe}_{0.2}\text{Ca}_x\text{O}_{3-\delta}$ , ( $x = 0$ and $0.01$ )

In Figure 4.20, the oxygen desorption of BSLCF and the  $\text{Ca}^{2+}$  ion added in BSLCF showed the major oxygen desorption in  $\beta\text{-O}_2$  which relates to the oxygen vacancy and the minor in of  $\gamma\text{-O}_2$  which is the oxygen lost from the lattice when the  $\text{Ca}^{2+}$  ions was added into the interstitial sites of BSLCF, the positive charge in the lattice was increased so the attractive force between cation and oxide ion was increased leading to the change in oxidation state at the B-site. Therefore, the losing of oxygen ion from the lattice were decreased. The peak areas of BSLCF incorporated with  $\text{Ca}^{2+}$  ion were concluded in Table 4.14.

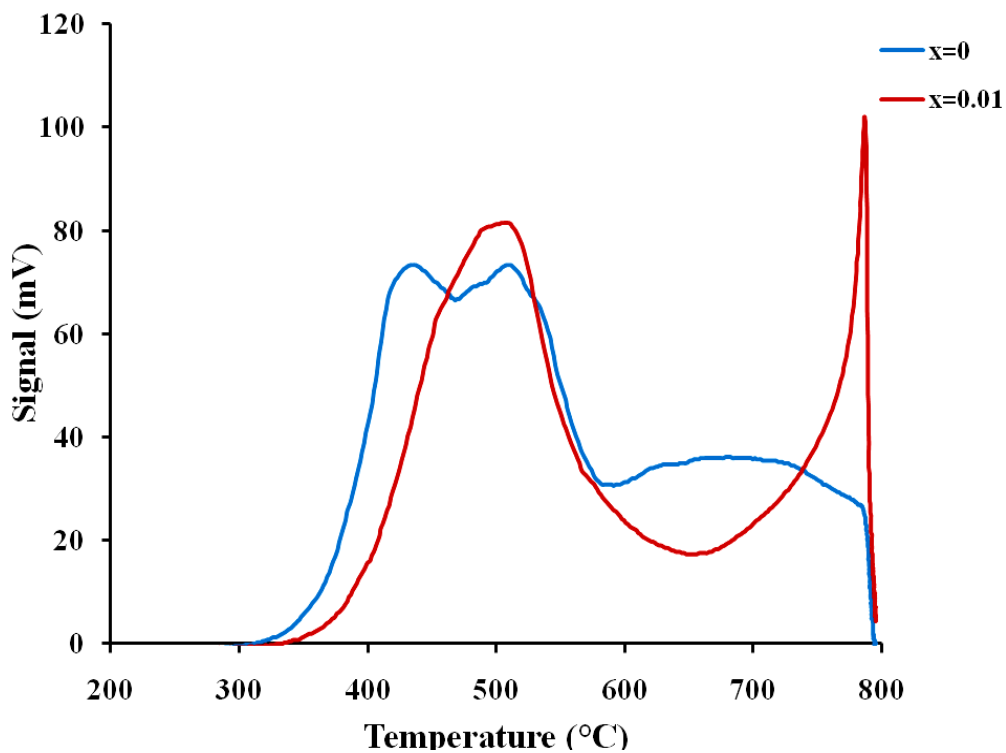


**Figure 4.20** Oxygen temperature programmed desorption curves of  $(\text{Ba}_{0.5}\text{Sr}_{0.5})_{0.8}\text{La}_{0.2}\text{Co}_{0.8}\text{Fe}_{0.2}\text{Ca}_x\text{O}_{3-\delta}$  ( $x = 0$  and  $0.01$ ) at  $200^\circ\text{C}$  to  $800^\circ\text{C}$ .

**Table 4.14** Oxygen desorption peak area of  $\text{Ba}_{0.5}\text{Sr}_{0.5}\text{La}_{0.2}\text{Co}_{0.8}\text{Fe}_{0.2}\text{Ca}_x\text{O}_{3-\delta}$  ( $x = 0$  and  $0.01$ )

Samples	Peak area (/0.1g)
$x = 0.00$	63,185
$x = 0.01$	68,545

### 4.3.3 Thermal expansion of $(\text{Ba}_{0.5}\text{Sr}_{0.5})_{0.8}\text{La}_{0.2}\text{Co}_{0.8}\text{Fe}_{0.2}\text{Ca}_x\text{O}_{3-\delta}$ , ( $x = 0$ and $0.01$ )

For  $\text{Ca}^{2+}$  addition in BSLCF, the thermal expansion of material was shown in Figure 4.21. The expansion of material was slightly decreased after addition of  $\text{Ca}^{2+}$  ion in BSLCF because the addition of positive charge of  $\text{Ca}^{2+}$  ions in the interstitial site made a stronger electrostatic attraction force between  $\text{Ca}^{2+}$  cation and oxygen anion in the lattice. Thus, the expansion of  $\text{Ca}^{2+}$  addition material was less than BSLCF as reveals in Table 4.15.

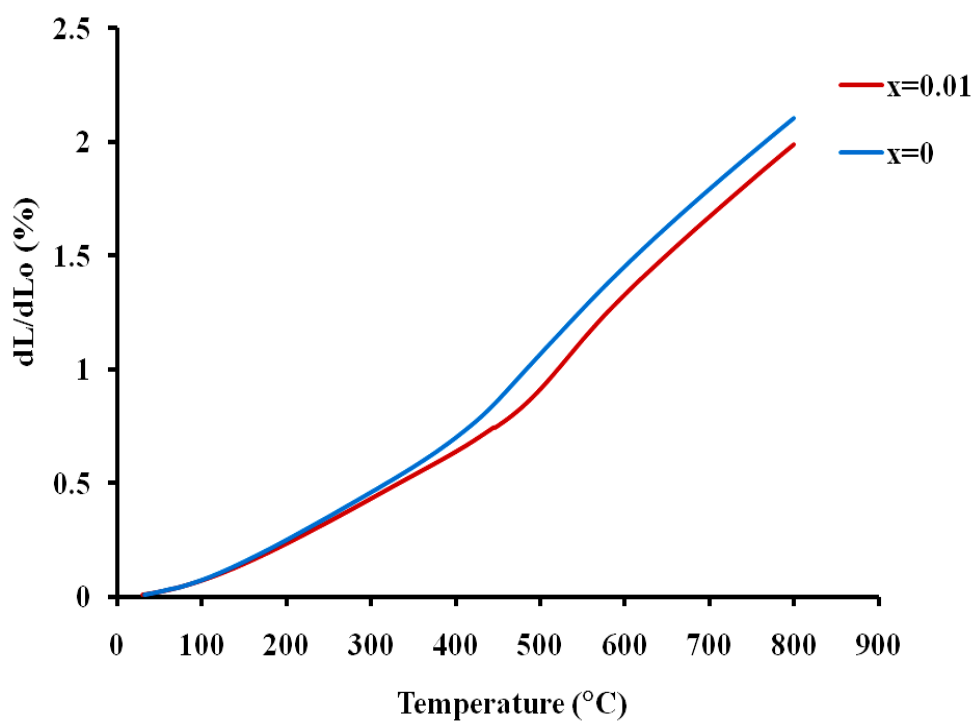


**Figure 4.21** Thermal expansion curves of  $(\text{Ba}_{0.5}\text{Sr}_{0.5})_{0.8}\text{La}_{0.2}\text{Co}_{0.8}\text{Fe}_{0.2}\text{Ca}_x\text{O}_{3-\delta}$ ,  
( $x = 0$  and  $0.01$ ) at  $50^\circ\text{C}$  to  $800^\circ\text{C}$ .

**Table 4.15** Thermal expansion coefficients of BSLCFCa<sub>0.01</sub> specimens at 50°C to 800°C

Samples	TEC ( $\times 10^{-6} \cdot ^\circ\text{C}^{-1}$ )
x = 0.00	27.746
x = 0.01	26.236

#### 4.4 Preparation and properties of Ba<sub>0.5</sub>Sr<sub>0.5</sub>Co<sub>0.8</sub>Fe<sub>0.2</sub>Cu<sub>x</sub>O<sub>3- $\delta$</sub> (BSCFCu), (0 ≤ x ≤ 0.2) perovskite oxide.

##### 4.4.1 Phase formation of Ba<sub>0.5</sub>Sr<sub>0.5</sub>Co<sub>0.8</sub>Fe<sub>0.2</sub>Cu<sub>x</sub>O<sub>3- $\delta$</sub> perovskite

The addition of Cu<sup>2+</sup> ion by non-stoichiometry in BSCF showed the single phase of cubic perovskite structure both after calcined and sintered, and no secondary phase was found as illustrated in Figure 4.22 and Figure 4.23, respectively. It could be postulated that the Cu<sup>2+</sup> ion may incorporate into the interstitial site of perovskite lattice because the position of the reflection peaks did not change and the calculated lattice parameters in Table 4.16 were not different. The results are similar to the study of Ga excess in Pr<sub>2</sub>NiO<sub>4</sub> (K<sub>2</sub>NiF<sub>4</sub>-structure) reported by Ishihara et al [42]. They believed that Ga was incorporated into the Pr<sub>2</sub>NiO<sub>4</sub> lattice by filling up the interstitial position, where it is the most reasonable position in the structure. However, the investigation in other properties such as the electrical property, thermal property and oxygen desorption of these materials were also required.

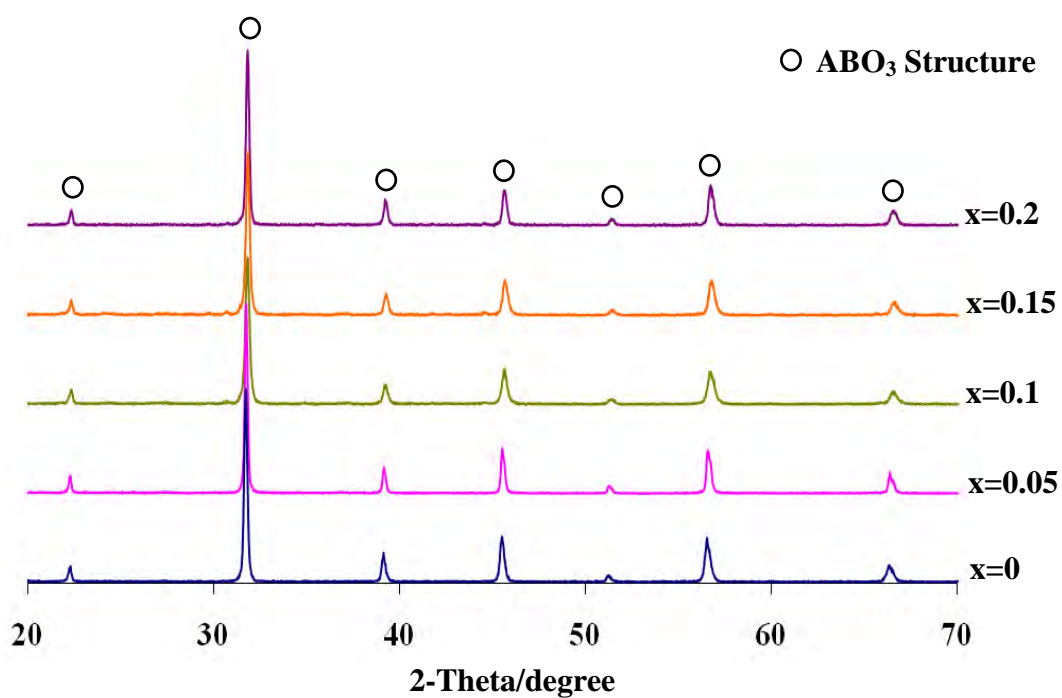


**Figure 4.22** XRD patterns of  $\text{Ba}_{0.5}\text{Sr}_{0.5}\text{Co}_{0.8}\text{Fe}_{0.2}\text{Cu}_x\text{O}_{3-\delta}$ , ( $0 \leq x \leq 0.2$ ) powder after calcined at  $900^\circ\text{C}$  for 5 hrs.

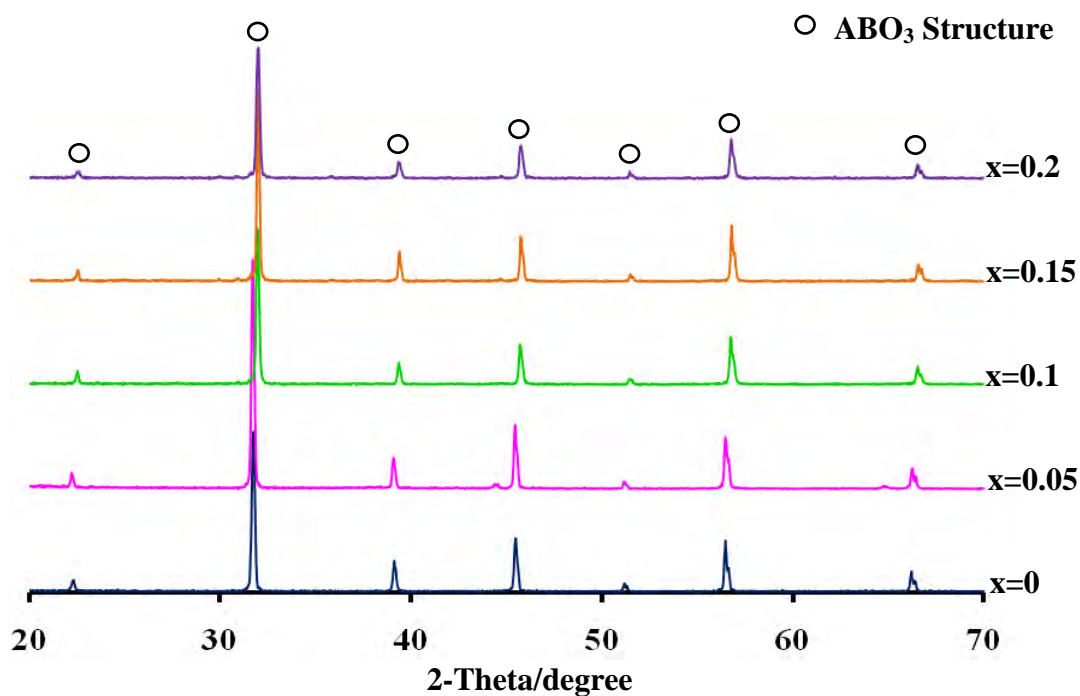


**Figure 4.23** XRD patterns of  $\text{Ba}_{0.5}\text{Sr}_{0.5}\text{Co}_{0.8}\text{Fe}_{0.2}\text{Cu}_x\text{O}_{3-\delta}$ , ( $0 \leq x \leq 0.2$ ) discs after sintered at  $1000^\circ\text{C}$  for 10 hrs.

**Table 4.16** Lattice parameters of  $\text{Ba}_{0.5}\text{Sr}_{0.5}\text{Co}_{0.8}\text{Fe}_{0.2}\text{Cu}_x\text{O}_{3-\delta}$  ( $0 \leq x \leq 0.2$ ) powder after calcined

<b>Samples</b>	<b>Lattice Parameter (nm)</b>
x = 0.00	0.398(5)
x = 0.05	0.397(3)
x = 0.10	0.397(5)
x = 0.15	0.397(1)
x = 0.20	0.397(3)

#### **4.4.2. The surface morphology of $\text{Ba}_{0.5}\text{Sr}_{0.5}\text{Co}_{0.8}\text{Fe}_{0.2}\text{Cu}_x\text{O}_{3-\delta}$ , BSCFCu ( $0 \leq x \leq 0.2$ )**

The surface morphology of BSCFCu were shown in Figure 4.24. The decreasing of pore was presented in these materials according to the increasing of  $\text{Cu}^{2+}$  ions. The result could be explained that the addition of  $\text{Cu}^{2+}$  ions (m.p.~1201°C), reduced the melting point of primitive BSCF perovskite oxide (m.p.~1933). Thus, the grain boundaries of BSCFCu were smaller and denser. However, the  $\text{Cu}^{2+}$  ions in the materials could be confirmed by the elemental mapping analysis which indicated the presence of homogeneous distribution of  $\text{Cu}^{2+}$  ion in the BSCFCu as shown in Figure 4.25. After the measuring of a relative density, the BSCFCu showed the increasing of relative density following the  $\text{Cu}^{2+}$  ion content, as summarized in Table 4.17.

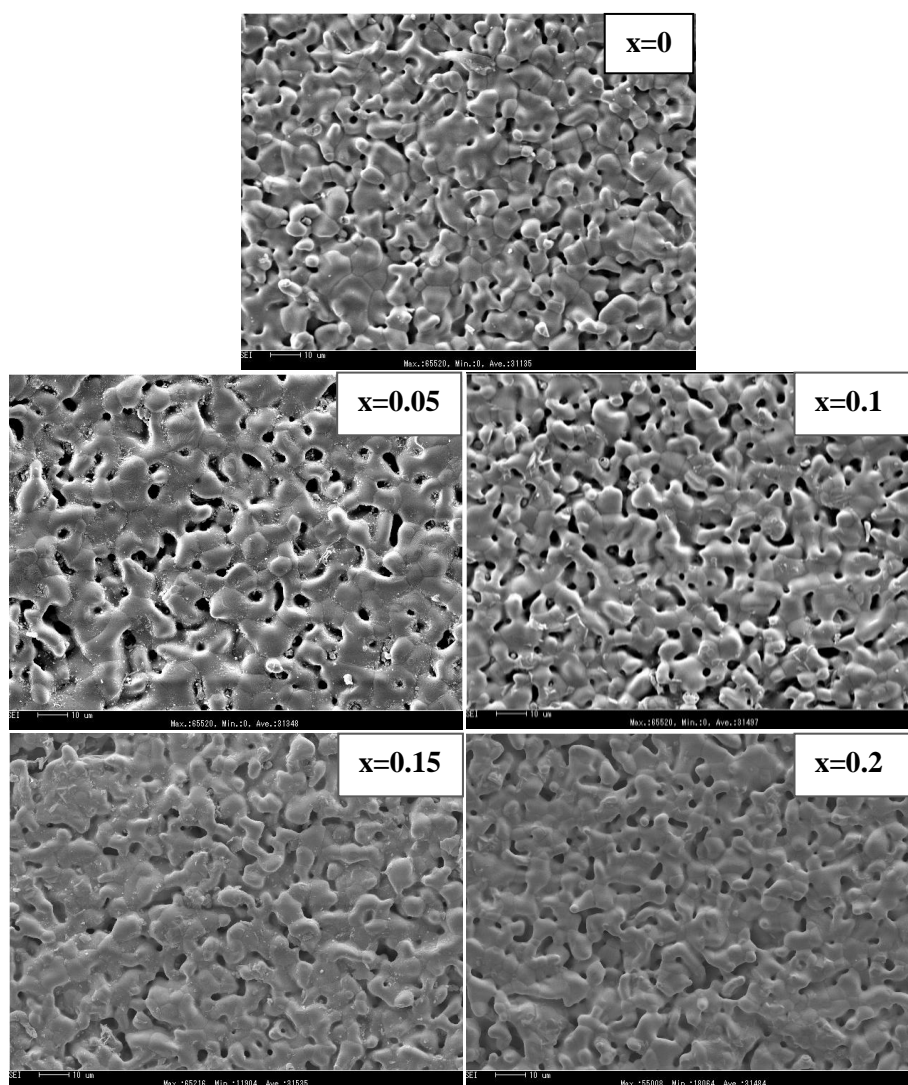


**Figure 4.24** SEM micrographs of  $\text{Ba}_{0.5}\text{Sr}_{0.5}\text{Co}_{0.8}\text{Fe}_{0.2}\text{Cu}_x\text{O}_{3-\delta}$ , ( $0 \leq x \leq 0.2$ )

after sintered at  $1000^\circ\text{C}$  for 10 hrs.



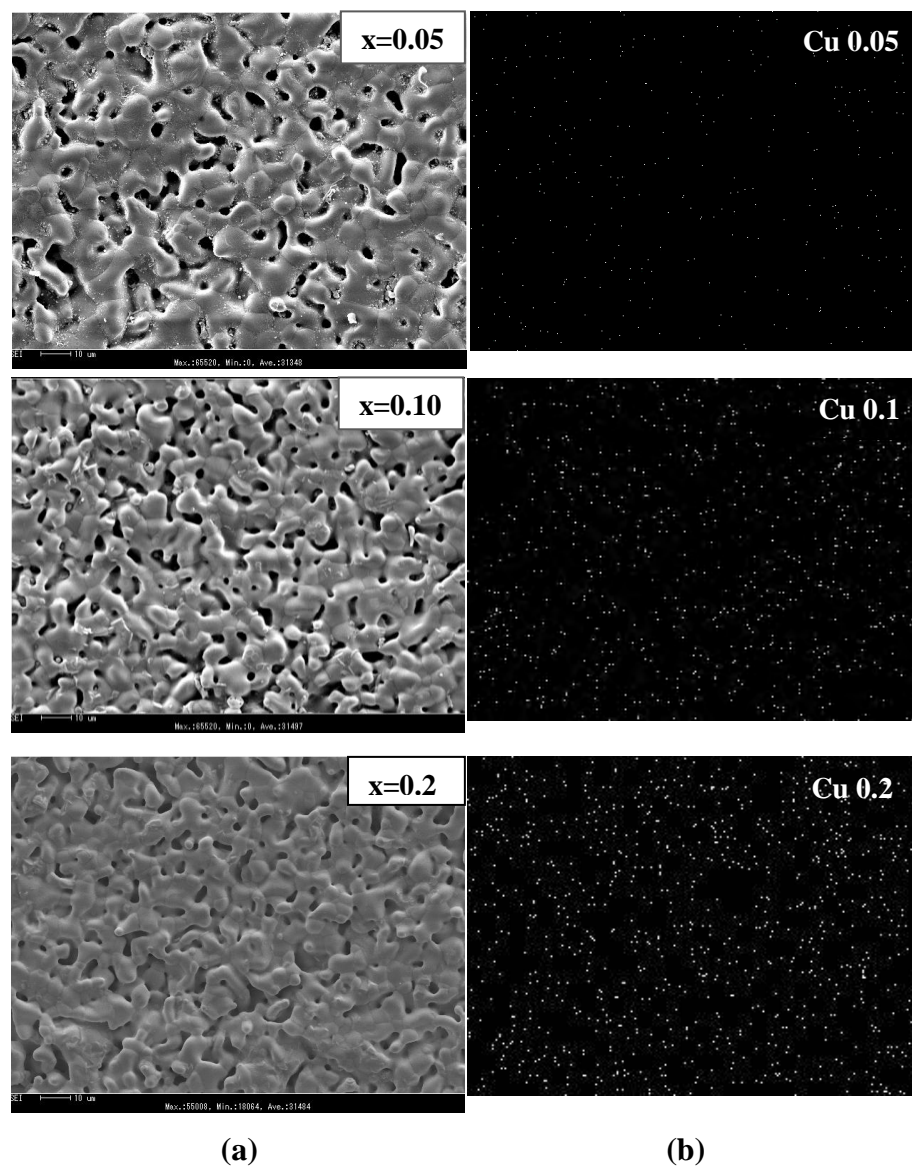


**Figure 4.25** Surface morphology (a) and elemental mapping (b) of  $\text{Ba}_{0.5}\text{Sr}_{0.5}\text{Co}_{0.8}\text{Fe}_{0.2}\text{Cu}_x\text{O}_{3-\delta}$  discs.

**Table 4.17** Relative density of  $\text{Ba}_{0.5}\text{Sr}_{0.5}\text{Co}_{0.8}\text{Fe}_{0.2}\text{Cu}_x\text{O}_{3-\delta}$ , ( $0 \leq x \leq 0.2$ )

<b>Samples</b>	<b>Relative density (%)</b>
x = 0.00	76.70
x = 0.05	72.50
x = 0.10	74.73
x = 0.15	79.30
x = 0.20	86.40

#### 4.4.3 Electrical Conductivity of $\text{Ba}_{0.5}\text{Sr}_{0.5}\text{Co}_{0.8}\text{Fe}_{0.2}\text{Cu}_x\text{O}_{3-\delta}$ , ( $0 \leq x \leq 0.2$ )

Figure 4.26 reveals the electrical conductivity of the addition of  $\text{Cu}^{2+}$  ion in BSCF. It has been seen that BSCFCu showed no significant difference in the electrical conductivity when increasing the  $\text{Cu}^{2+}$  ions content. The conductivity values were summarized in Table 4.18. It could be indicated that the  $\text{Cu}^{2+}$  ions in the interstitial sites of perovskite lattice did not have significant impact on the electrical conductivity.

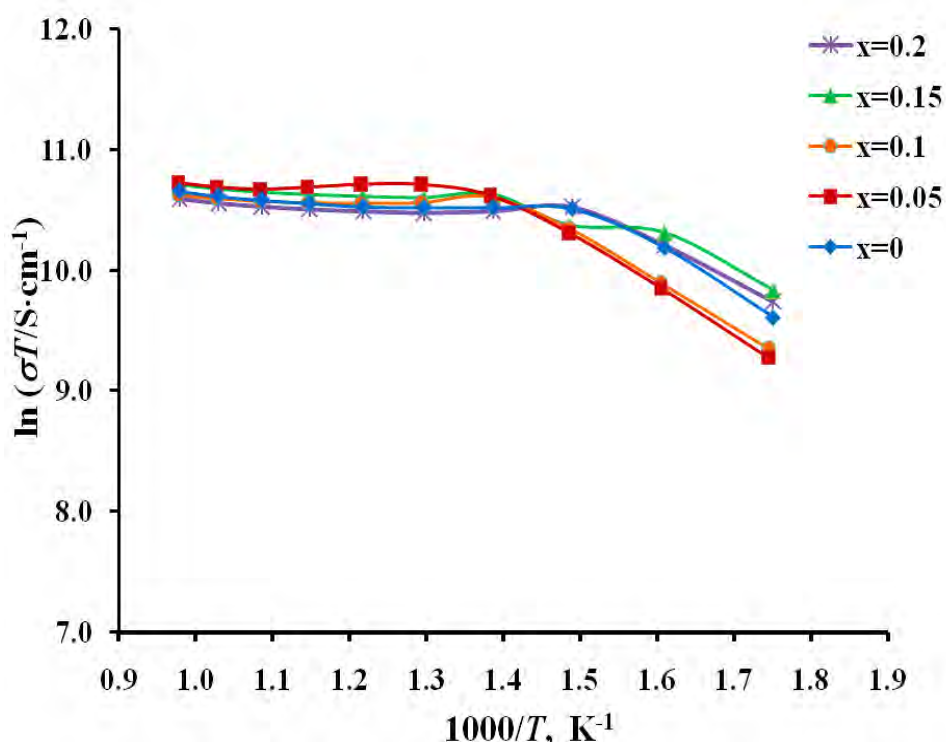


**Figure 4.26** The electrical conductivity of  $\text{Ba}_{0.5}\text{Sr}_{0.5}\text{Co}_{0.8}\text{Fe}_{0.2}\text{Cu}_x\text{O}_{3-\delta}$ , ( $0 \leq x \leq 0.2$ ) at 300°C to 750°C.

**Table 4.18** The electrical conductivity of  $\text{Ba}_{0.5}\text{Sr}_{0.5}\text{Co}_{0.8}\text{Fe}_{0.2}\text{Cu}_x\text{O}_{3-\delta}$ , ( $0 \leq x \leq 0.2$ ) at various temperature

Sample	Temperature (°C)						$\sigma_{\text{max.}}$ S·cm <sup>-1</sup> (°C)
	300	400	500	600	700	800	
x = 0.00	26.57	54.28	49.04	45.19	42.89	42.47	54.28 (400)
x = 0.05	18.59	44.67	58.03	50.20	45.15	44.32	58.03 (500)
x = 0.10	22.70	47.67	47.34	42.09	39.19	38.03	52.64 (450)
x = 0.15	32.54	62.08	51.84	47.04	44.23	43.25	62.08 (400)
x = 0.2	29.58	55.27	45.90	41.82	39.49	38.76	55.27 (400)

#### 4.4.4 Temperature programmed desorption of $\text{Ba}_{0.5}\text{Sr}_{0.5}\text{Co}_{0.8}\text{Fe}_{0.2}\text{Cu}_x\text{O}_{3-\delta}$ , ( $0 \leq x \leq 0.2$ )

Figure 4.27 shows the oxygen desorption of the addition of  $\text{Cu}^{2+}$  ion in BSCF. They were mainly composed of  $\beta\text{-O}_2$  and minor of  $\gamma\text{-O}_2$ . The small amount of  $\text{Cu}^{2+}$  ion increased the desorption of oxygen in the oxygen vacancy because the addition of  $\text{Cu}^{2+}$  induced the positive charge in the lattice. Thus, the attractive force in the lattice was increased leading to the increase in  $\beta\text{-O}_2$ . In addition, at high amount of  $\text{Cu}^{2+}$  ion, the decreasing of  $\beta\text{-O}_2$  was obtained whereas the  $\gamma\text{-O}_2$  was increased due to the reduction of B-site cation for maintaining the charge neutrality. From the  $\text{O}_2$ -TPD results, it was confirmed that the  $\text{Cu}^{2+}$  ion could be incorporated in the interstitial site of the lattice. Table 4.19 shows the total peak areas increased with the increasing of  $\text{Cu}^{2+}$  ion content.

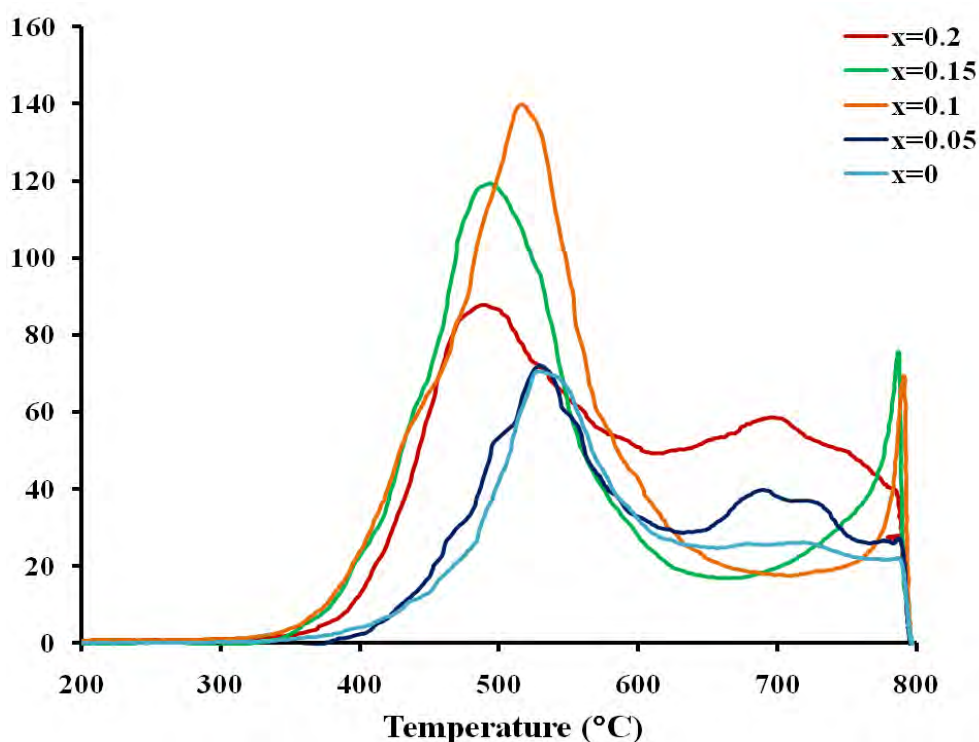


**Figure 4.27** Oxygen temperature programmed desorption curves of  $(\text{Ba}_{0.5}\text{Sr}_{0.5})_{0.8}\text{Co}_{0.8}\text{Fe}_{0.2}\text{Cu}_x\text{O}_{3-\delta}$ , ( $0 \leq x \leq 0.2$ ) at  $200^\circ\text{C}$  to  $800^\circ\text{C}$ .

**Table 4.19** Oxygen desorption peak area of  $\text{Ba}_{0.5}\text{Sr}_{0.5}\text{Co}_{0.8}\text{Fe}_{0.2}\text{Cu}_x\text{O}_{3-\delta}$ ,  
( $0 \leq x \leq 0.2$ )

<b>Samples</b>	<b>Peak area (/0.1g)</b>
x = 0.00	46,242
x = 0.05	52,200
x = 0.10	87,200
x = 0.15	83,330
x = 0.20	87,515

#### 4.4.5 Thermal expansion of $\text{Ba}_{0.5}\text{Sr}_{0.5}\text{Co}_{0.8}\text{Fe}_{0.2}\text{Cu}_x\text{O}_{3-\delta}$ , ( $0 \leq x \leq 0.2$ )

Figure 4.28 shows the thermal expansion curves of BSCFCu as a function of temperature. The thermal expansion of BSCFCu specimens were increased with the rising of the temperature. However, the doping of  $\text{Cu}^{2+}$  ions it did not show the difference in thermal expansion of BSCFCu. Since  $\text{Cu}^{2+}$  ion (EN = 2.00) had the electronegativity values nearly the B-site cations ( $\text{Co}^{3+}$  and  $\text{Fe}^{3+}$ , EN = 1.88 and 1.96, respectively) [43], the attraction force between  $\text{Cu}^{2+}$  ion and oxygen ion in the lattice was not different from the host B-site cation. Thus, the thermal expansions of the specimens were not changed. The TEC values were calculated from the slope of these curve and be summarized in Table 4.20.

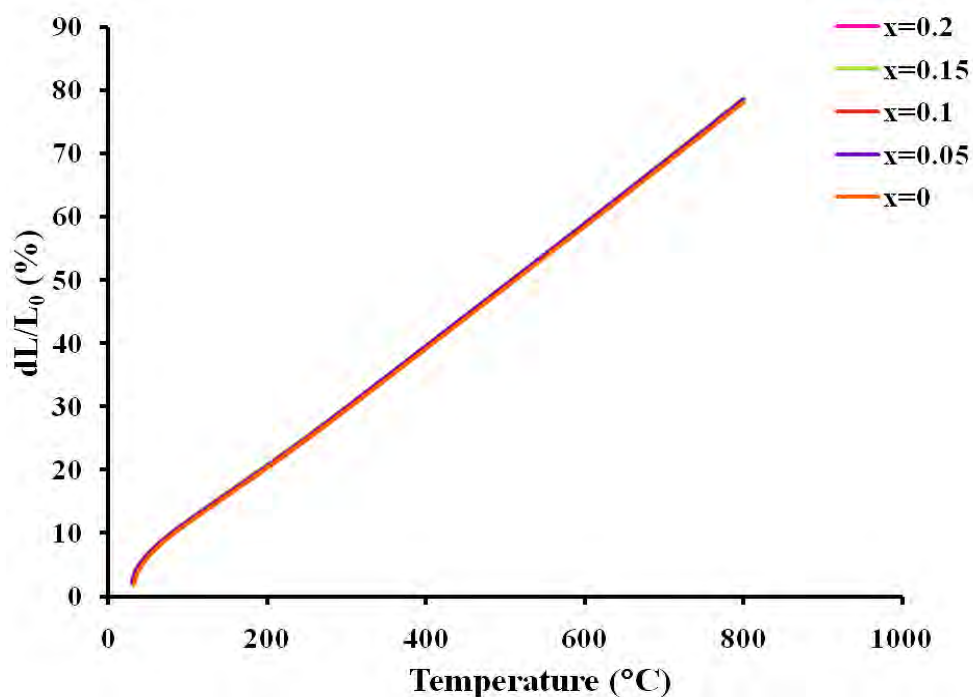


**Figure 4.28** Thermal expansion curves of  $\text{Ba}_{0.5}\text{Sr}_{0.5}\text{Co}_{0.8}\text{Fe}_{0.2}\text{Cu}_x\text{O}_{3-\delta}$ , ( $0 \leq x \leq 0.2$ ) at  $50^\circ\text{C}$  to  $800^\circ\text{C}$ .

**Table 4.20** Thermal expansion coefficients of  $\text{Ba}_{0.5}\text{Sr}_{0.5}\text{Co}_{0.8}\text{Fe}_{0.2}\text{Cu}_x\text{O}_{3-\delta}$  specimens at  $50^\circ\text{C}$  to  $800^\circ\text{C}$

Samples	TEC ( $\times 10^{-6} \cdot ^\circ\text{C}^{-1}$ )
$x = 0.00$	20.375
$x = 0.05$	20.068
$x = 0.10$	20.334
$x = 0.15$	19.531
$x = 0.20$	20.423

## 4.5 Preparation and properties of $\text{Ba}_{0.5}\text{Sr}_{0.5}\text{Co}_{0.8}\text{Fe}_{0.2}\text{Zn}_x\text{O}_{3-\delta}$ (BSCFZn), ( $0 \leq x \leq 0.2$ ) perovskite oxide.

### 4.5.1 Phase formation of $\text{Ba}_{0.5}\text{Sr}_{0.5}\text{Co}_{0.8}\text{Fe}_{0.2}\text{Zn}_x\text{O}_{3-\delta}$ perovskite

The x-ray diffraction patterns of  $\text{Ba}_{0.5}\text{Sr}_{0.5}\text{Co}_{0.8}\text{Fe}_{0.2}\text{Zn}_x\text{O}_{3-\delta}$  ( $0 \leq x \leq 0.2$ ) (BSCFZn) perovskites both after calcined and sintered showed a single phase of cubic perovskite structure and no secondary phase was found, as illustrated in Figure 4.29 and Figure 4.30. It could be postulated that the  $\text{Zn}^{2+}$  ion may also incorporate into the interstitial site of perovskite lattice as  $\text{Cu}^{2+}$  ion because the position of the refraction peaks did not change and the calculate lattice parameters that summarized in Table 4.21 were not different. Moreover, the addition of  $\text{Zn}^{2+}$  ion was noticed on the change in surface morphology of BSCFZn materials as shown in Figure 4.31.

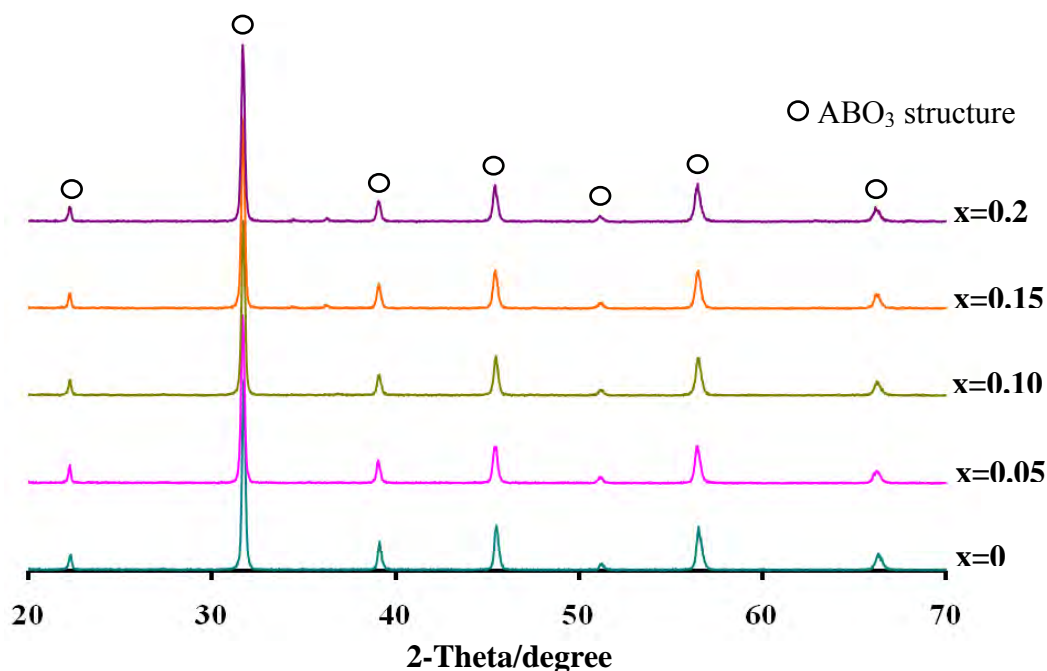


**Figure 4.29** XRD patterns of  $\text{Ba}_{0.5}\text{Sr}_{0.5}\text{Co}_{0.8}\text{Fe}_{0.2}\text{Zn}_x\text{O}_{3-\delta}$ , ( $0 \leq x \leq 0.2$ ) powder after calcined at  $1000^\circ\text{C}$  for 5 hrs.

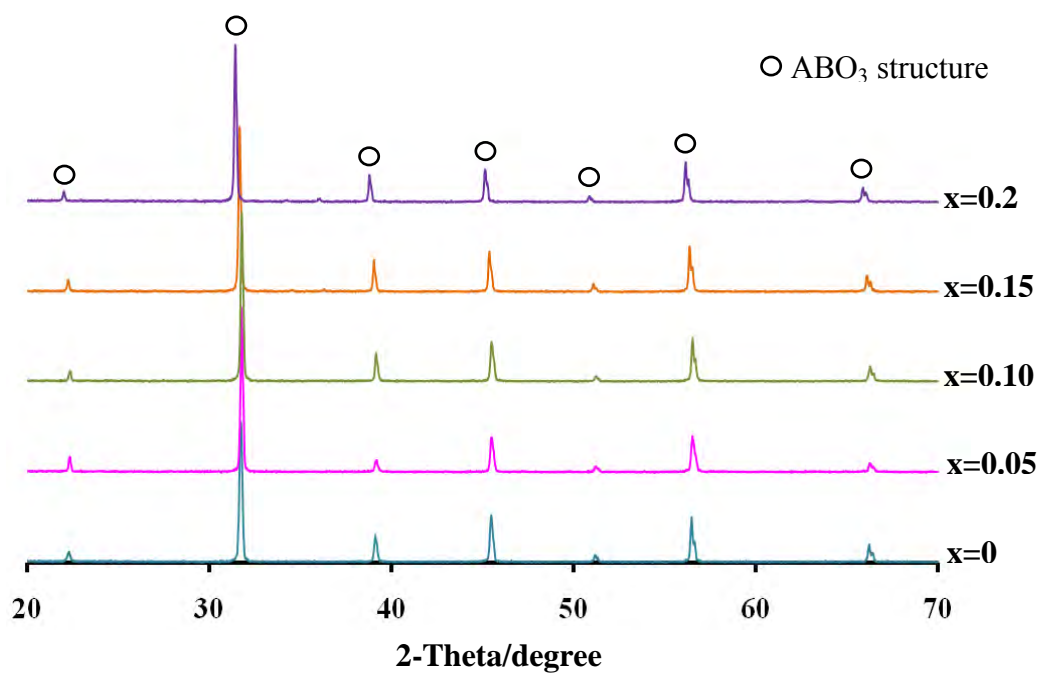


**Figure 4.30** XRD patterns of  $\text{Ba}_{0.5}\text{Sr}_{0.5}\text{Co}_{0.8}\text{Fe}_{0.2}\text{Zn}_x\text{O}_{3-\delta}$ , ( $0 \leq x \leq 0.2$ ) membrane after sintered at  $1100^\circ\text{C}$  for 10 hrs.

**Table 4.21** Lattice parameters of  $\text{Ba}_{0.5}\text{Sr}_{0.5}\text{Co}_{0.8}\text{Fe}_{0.2}\text{Zn}_x\text{O}_{3-\delta}$  ( $0 \leq x \leq 0.2$ ) powder after calcined

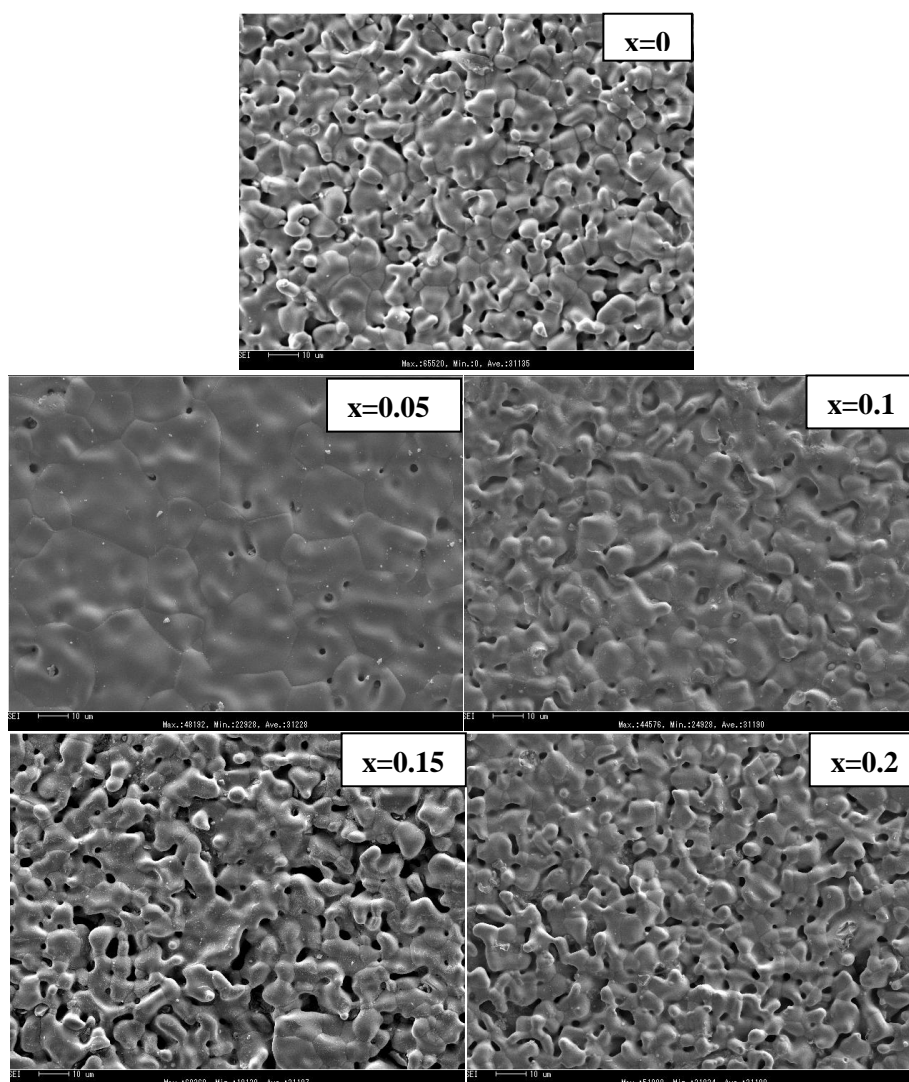
Samples	Lattice Parameter (nm)
$x = 0.00$	0.398(5)
$x = 0.05$	0.399(1)
$x = 0.10$	0.398(7)
$x = 0.15$	0.398(7)
$x = 0.20$	0.398(9)



#### 4.5.2. The surface morphology of $\text{Ba}_{0.5}\text{Sr}_{0.5}\text{Co}_{0.8}\text{Fe}_{0.2}\text{Zn}_x\text{O}_{3-\delta}$ , BSCFZn

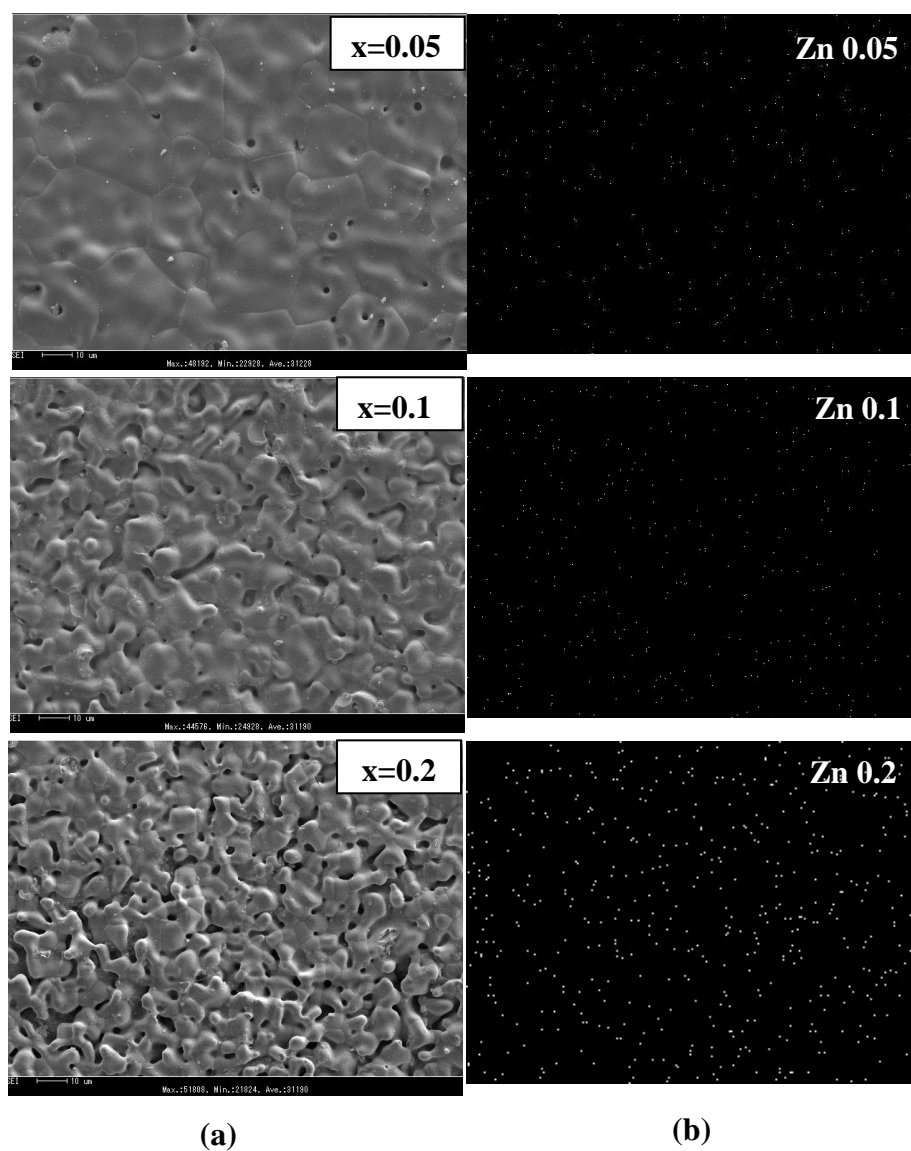
$$(0 \leq x \leq 0.2)$$

Figure 4.31 shows the surface morphology of  $\text{Zn}^{2+}$  ion added in BSCF. The surface morphologies indicated the increasing of pores concurrently with increasing of  $\text{Zn}^{2+}$  ion content. The results could be explained that the addition of  $\text{Zn}^{2+}$  ion (m.p.  $\sim 1975^\circ\text{C}$ ) increased the melting point of primitive BSCF perovskite oxide (m.p.  $\sim 1933^\circ\text{C}$ ). Thus, the nucleation process was faster than in primitive BSCF, which led to the small grain boundary obtained. However, the  $\text{Zn}^{2+}$  ion in the materials could be also confirmed by the presence of homogeneous distribution of  $\text{Zn}^{2+}$  ion in the BSCFZn as shown in Figure 4.32. The relative density of the BSCFZn specimens were summarized in Table 4.22, however there were no correlation on the relative density and amount of  $\text{Zn}^{2+}$  ion added.



**Figure 4.31** SEM micrographs of  $\text{Ba}_{0.5}\text{Sr}_{0.5}\text{Co}_{0.8}\text{Fe}_{0.2}\text{Zn}_x\text{O}_{3-\delta}$ , ( $0 \leq x \leq 0.2$ )

after sintered at  $1100^\circ\text{C}$  for 10 hrs.



**Figure 4.32** Surface morphology (a) and elemental mapping (b) of  $\text{Ba}_{0.5}\text{Sr}_{0.5}\text{Co}_{0.8}\text{Fe}_{0.2}\text{Zn}_x\text{O}_{3-\delta}$  discs.

**Table 4.22** Relative density of  $\text{Ba}_{0.5}\text{Sr}_{0.5}\text{Co}_{0.8}\text{Fe}_{0.2}\text{Zn}_x\text{O}_{3-\delta}$ , ( $0 \leq x \leq 0.2$ )

<b>Samples</b>	<b>Relative density (%)</b>
x = 0.00	76.70
x = 0.05	91.11
x = 0.10	79.96
x = 0.15	71.61
x = 0.20	75.44

#### 4.5.3 Electrical Conductivity of $\text{Ba}_{0.5}\text{Sr}_{0.5}\text{Co}_{0.8}\text{Fe}_{0.2}\text{Zn}_x\text{O}_{3-\delta}$ , ( $0 \leq x \leq 0.2$ )

The electrical conductivity of the addition of  $\text{Zn}^{2+}$  ion in BSCF was revealed in Figure 4.33. It was shown that the electrical conductivity increased as a function of the temperature and tended to slightly decrease with the increasing of  $\text{Zn}^{2+}$  ions, as shown in Table 4.23.  $\text{Zn}^{2+}$  ions that may be present in the interstitial sites of perovskite lattice, introduced the perovskite structure block. Thus, the transportation of oxygen ion was reduced and led to the decreasing of electrical conductivity from around  $55 \text{ S}\cdot\text{cm}^{-1}$  to  $35 \text{ S}\cdot\text{cm}^{-1}$  at  $400^\circ\text{C}$ . Corresponding to the study of Ishihara et.al. [41], they believed that Ga excess was introduced the rock-salt block and caused the reduction in electrical conductivity.

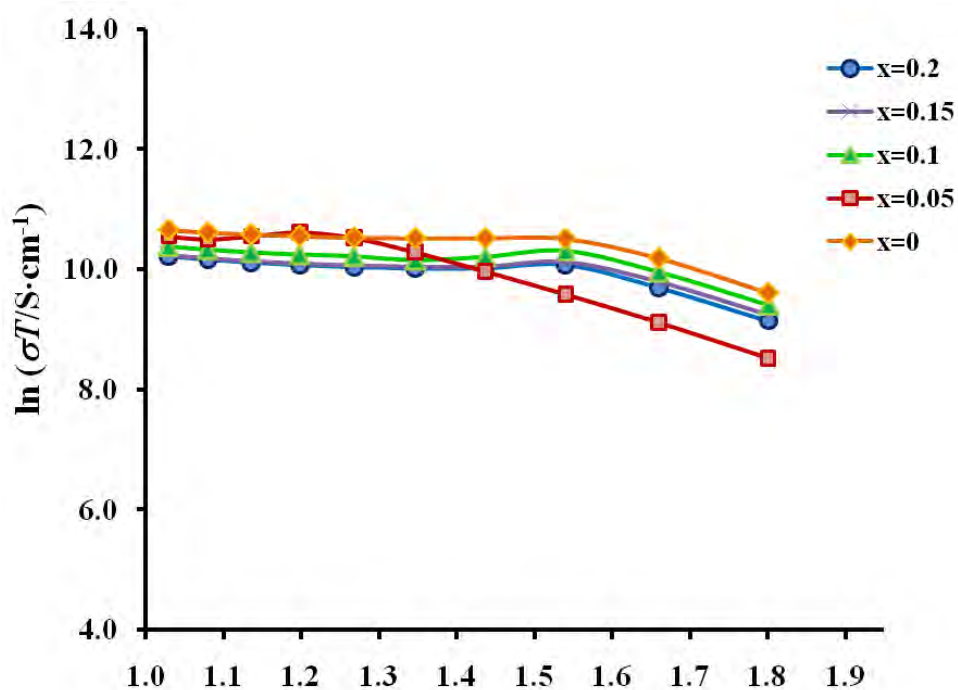


**Figure 4.33** The electrical conductivity of  $\text{Ba}_{0.5}\text{Sr}_{0.5}\text{Co}_{0.8}\text{Fe}_{0.2}\text{Zn}_x\text{O}_{3-\delta}$ , ( $0 \leq x \leq 0.2$ ) at  $300^\circ\text{C}$  to  $750^\circ\text{C}$ .

**Table 4.23** The electrical conductivity of  $\text{Ba}_{0.5}\text{Sr}_{0.5}\text{Co}_{0.8}\text{Fe}_{0.2}\text{Zn}_x\text{O}_{3-\delta}$ , ( $0 \leq x \leq 0.2$ ) at various temperature

Sample	Temperature ( $^\circ\text{C}$ )						$\sigma_{\text{max.}}$ $\text{S}\cdot\text{cm}^{-1}$ ( $^\circ\text{C}$ )
	300	400	500	600	700	800	
x = 0.00	26.57	54.28	49.04	45.19	42.89	42.47	54.28 (400)
x = 0.05	8.79	21.65	38.02	46.84	37.48	37.72	46.84 (600)
x = 0.10	21.34	44.35	33.18	32.16	31.31	31.58	44.35 (400)
x = 0.15	17.97	37.01	29.78	27.78	27.21	27.60	37.01 (400)
x = 0.20	16.27	35.09	28.86	26.97	26.48	26.90	35.09 (400)

#### 4.5.4 Temperature programmed desorption of $\text{Ba}_{0.5}\text{Sr}_{0.5}\text{Co}_{0.8}\text{Fe}_{0.2}\text{Zn}_x\text{O}_{3-\delta}$ , ( $0 \leq x \leq 0.2$ )

Figure 4.34 shows the oxygen desorption of the addition of  $\text{Zn}^{2+}$  ion in BSCF perovskite oxide. The addition of small amount  $\text{Zn}^{2+}$  ion in BSCF was increased the oxygen desorption in the oxygen vacancy. It was contributed that the increasing of positive charge ( $\text{Zn}^{2+}$  ion) led to the high attraction force in the lattice so the oxygen vacancy would be increased. However, the increasing of  $\text{Zn}^{2+}$  ions had a trend to decrease in the oxygen desorption as shown in Table 4.24, because the high content of  $\text{Zn}^{2+}$  ions in the interstitial site hindered the transportation of oxygen ion and blocked the oxygen vacancy in the lattice. Thus, the oxygen desorption of BSCFZn materials were decreased.

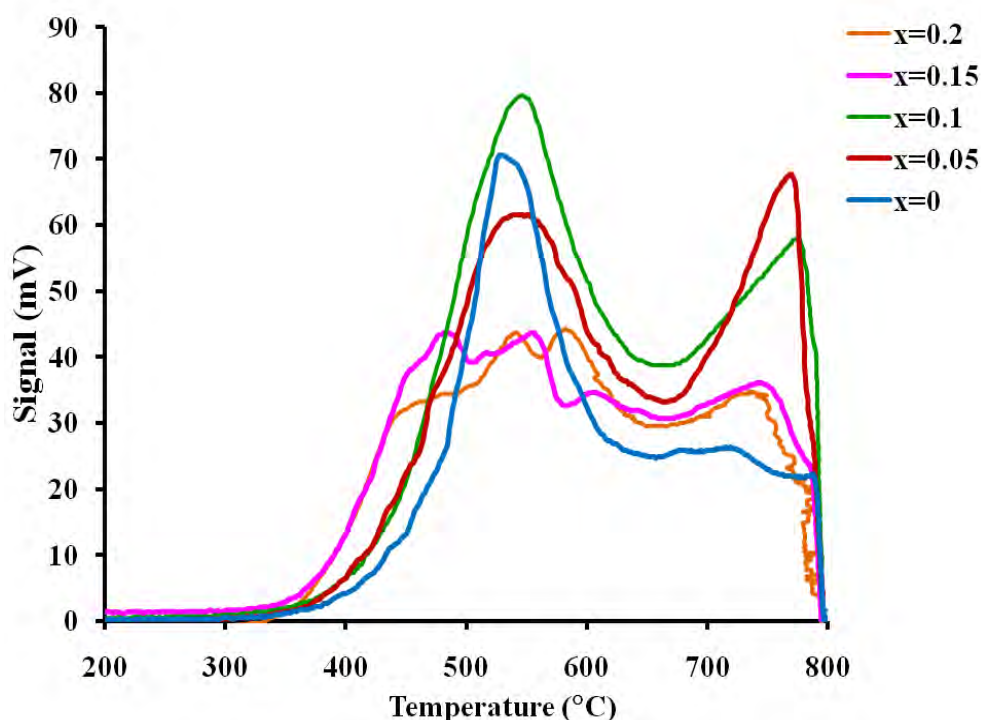


**Figure 4.34** Oxygen temperature programmed desorption curves of  $(\text{Ba}_{0.5}\text{Sr}_{0.5})_{0.8}\text{Co}_{0.8}\text{Fe}_{0.2}\text{Zn}_x\text{O}_{3-\delta}$ , ( $0 \leq x \leq 0.2$ ) at  $200^\circ\text{C}$  to  $800^\circ\text{C}$ .

**Table 4.24** Oxygen desorption peak area of  $\text{Ba}_{0.5}\text{Sr}_{0.5}\text{Co}_{0.8}\text{Fe}_{0.2}\text{Zn}_x\text{O}_{3-\delta}$ , ( $0 \leq x \leq 0.2$ )

Samples	Peak area (/0.1g)
x = 0.00	46,242
x = 0.05	66,971
x = 0.10	60,722
x = 0.15	53,112
x = 0.20	48,445

#### 4.5.5 Thermal expansion of $\text{Ba}_{0.5}\text{Sr}_{0.5}\text{Co}_{0.8}\text{Fe}_{0.2}\text{Zn}_x\text{O}_{3-\delta}$ , ( $0 \leq x \leq 0.2$ )

Figure 4.35 shows the thermal expansion of BSCFZn as a function of temperature. The thermal expansion of BSCFZn materials were increased with the rising of the temperature. Nevertheless, the addition of  $\text{Zn}^{2+}$  ion in the BSCF showed the decreasing of the thermal expansion because the increasing of  $\text{Zn}^{2+}$  ion in BSCF as the increasing of the positive charge in the lattice. Thus the attraction force between cations and oxygen ions in the lattice were increased leading to the reduction in thermal expansion. The minimum value of thermal expansion coefficient of BSCFZn was  $16.354 \times 10^{-6} \cdot ^\circ\text{C}^{-1}$  as lower than that of previous work by Bo W. et. al. [44] for substitution of the  $\text{Ba}^{2+}$  ion in  $\text{Ba}_x\text{Sr}_{1-x}\text{Co}_{0.8}\text{Fe}_{0.2}\text{O}_{3-\delta}$ , the minimum value was  $20.27 \times 10^{-6} \cdot ^\circ\text{C}^{-1}$ . The TEC values were calculated from the slope of the curves and be summarized in the Table 4.25.

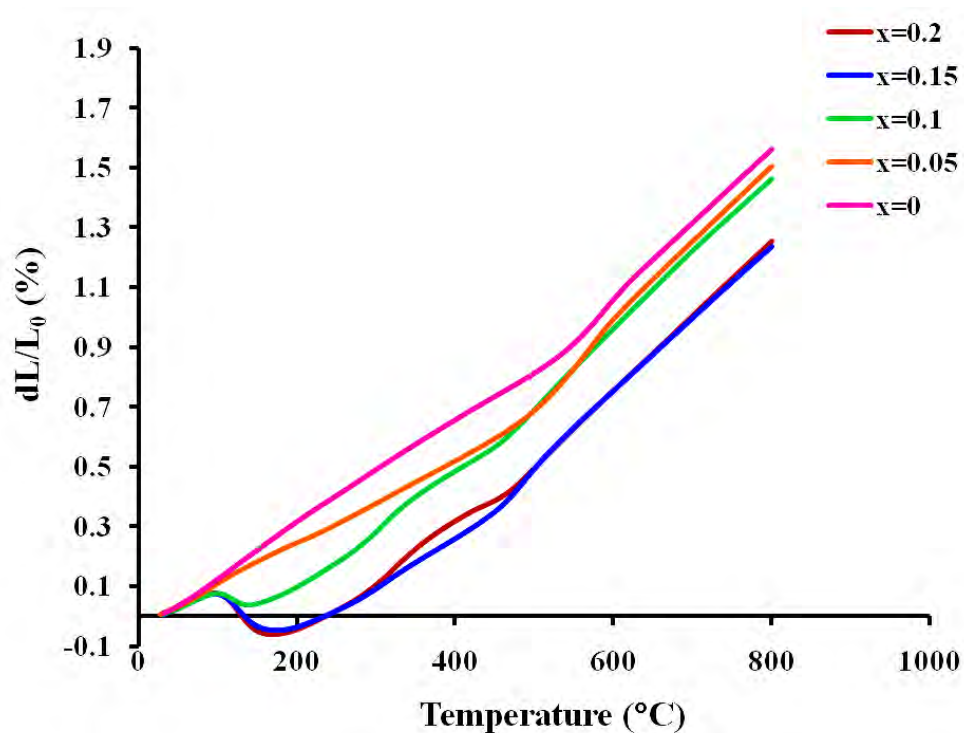


**Figure 4.35** Thermal expansion curves of  $\text{Ba}_{0.5}\text{Sr}_{0.5}\text{Co}_{0.8}\text{Fe}_{0.2}\text{Zn}_x\text{O}_{3-\delta}$ , ( $0 \leq x \leq 0.2$ ) were measured at  $50^\circ\text{C}$  to  $800^\circ\text{C}$ .

**Table 4.25** Thermal expansion coefficients of  $\text{Ba}_{0.5}\text{Sr}_{0.5}\text{Co}_{0.8}\text{Fe}_{0.2}\text{Zn}_x\text{O}_{3-\delta}$  specimens measured at  $50^\circ\text{C}$  to  $800^\circ\text{C}$

Samples	TEC ( $\times 10^{-6} \cdot ^\circ\text{C}^{-1}$ )
x = 0.00	20.375
x = 0.05	19.670
x = 0.10	19.159
x = 0.15	16.080
x = 0.20	16.354



## CHAPTER V

### CONCLUSIONS

#### 5.1 Conclusions

The partial substitution of  $\text{Ca}^{2+}$  ion,  $\text{La}^{3+}$  and  $\text{Ca}^{2+}$  ions in  $\text{Ba}_{0.5}\text{Sr}_{0.5}\text{Co}_{0.8}\text{Fe}_{0.2}\text{O}_{3-\delta}$  (BSCF) and the addition of  $\text{Ca}^{2+}$ ,  $\text{Cu}^{2+}$  and  $\text{Zn}^{2+}$  ions in BSLCF and BSCF, respectively were synthesized by modified citrate method. The phase identification of synthesized sample was investigated by XRD. Microstructures of the sintered bodies were observed by SEM. The density was determined by Archimedes method. The electrical conductivity was measured by DC four probes method. Moreover, the oxygen desorption in materials was measured by  $\text{O}_2$ -TPD technique and the thermal expansion of the materials was measured by the dilatometer.

The XRD patterns of  $(\text{Ba}_{0.5}\text{Sr}_{0.5})_{1-x}\text{Ca}_x\text{Co}_{0.8}\text{Fe}_{0.2}\text{O}_{3-\delta}$  ( $0 \leq x \leq 0.5$ ) or BSCCF were achieved the single phase of cubic perovskite structure until the  $\text{Ca}^{2+}$  ion content was 30 mol%. The relative density of the BSCCF was increased with increasing the  $\text{Ca}^{2+}$  ion content. The maximum electrical conductivity of BSCCF obtained at the 30 mol% of  $\text{Ca}^{2+}$  ions was  $96 \text{ S}\cdot\text{cm}^{-1}$ . In addition the oxygen desorption of BSCCF materials was increased with the increasing of the  $\text{Ca}^{2+}$  ions to 30 mol% and then decreased. Furthermore, the thermal expansion of BSCCF materials was not affected by the substitution of  $\text{Ca}^{2+}$  ion.

The partial substitution of  $\text{La}^{3+}$  and  $\text{Ca}^{2+}$  ions in A-site of BSCF to produce BSLCCF also showed the single phase of cubic perovskite structure. The relative density of BSLCCF was increased with increasing of  $\text{Ca}^{2+}$  ion content. However, the electrical conductivities of BSLCCF were decreased with decreasing the  $\text{La}^{3+}$  ion content, the maximum conductivity was obtained from BSLCF around  $353 \text{ S}\cdot\text{cm}^{-1}$  at  $350^\circ\text{C}$ . In addition, the oxygen desorption of BSLCCF decreased following the decreasing of  $\text{La}^{3+}$  ion content which associated with the decreasing of electrical conductivity. Nevertheless, the thermal expansion of BSLCCF was decreased with the reducing of  $\text{La}^{3+}$  ions.

The phase identification of the addition of  $\text{Ca}^{2+}$  ion in BSLCF to produce BSLCFCa perovskite oxide showed the single phase of cubic perovskite structure. The dense microstructures and the increasing of the relative density were obtained in BSLCFCa<sub>0.01</sub>. Moreover, the electrical conductivity of BSLCFCa<sub>0.01</sub> could be increased to  $591 \text{ S}\cdot\text{cm}^{-1}$  at  $350 \text{ }^\circ\text{C}$  according to the increase in oxygen desorption in the lattice from the  $\text{O}_2$ -TPD result. Moreover, the thermal expansion of BSLCFCa<sub>0.01</sub> was decreased by  $\text{Ca}^{2+}$  ion addition.

The XRD patterns of BSCFCu samples showed the single phase of cubic perovskite structure. The dense microstructures and the increasing of the relative density were obtained with the increasing of  $\text{Cu}^{2+}$  ion. However, the addition of  $\text{Cu}^{2+}$  in BSCF did not have a significant effect on the electrical conductivity. Nevertheless, the addition of  $\text{Cu}^{2+}$  ion could increase the oxygen diffusion in the lattice and maintained the thermal expansion of the BSCFCu materials.

In addition, BSCFZn showed the single phase of cubic perovskite structure. The morphology showed the increasing of porosity with high content of  $\text{Zn}^{2+}$  ions. However, the  $\text{Zn}^{2+}$  ion incorporated in the lattice of BSCF affected the electrical conductivity of BSCFZn from  $54 \text{ S}\cdot\text{cm}^{-1}$  to  $34 \text{ S}\cdot\text{cm}^{-1}$  according to the decreasing of oxygen diffusion in the lattice in the  $\text{O}_2$ -TPD result. Nevertheless, the thermal expansion of BSCFZn material was decreased with the increasing of  $\text{Zn}^{2+}$  ion content.

From this research it can be concluded that the substitution of  $\text{Ca}^{2+}$  ion and  $\text{La}^{3+}$  ion in A-site of BSCF and the addition of  $\text{Ca}^{2+}$  ion in BSLCF obviously improved the electrical property of materials and the addition of  $\text{Cu}^{2+}$  and  $\text{Zn}^{2+}$  ions developed the oxygen adsorption and thermal expansion properties of BSCF. Furthermore, the maximum electrical conductivity was achieved in this research for  $591 \text{ S}\cdot\text{cm}^{-1}$  at  $350 \text{ }^\circ\text{C}$  in BSLCFCa<sub>0.01</sub>, suggesting BSCCF with 30 mol%  $\text{Ca}^{2+}$  and BSLCFCa<sub>0.01</sub> are the potential candidates for SOFC cathode application.

## 5.2 Suggestion

From experimental results, the future work should be focused on the following:

1. To study the phase structure and surface morphology of BSLCFCa<sub>x</sub> (x = 0.02, 0.03, 0.05) after sintering and to measure the oxygen adsorption, electrical conductivity and thermal expansion of these samples.

2. To study the compatibility of BS<sub>0.9</sub>CCF with Ca<sup>2+</sup> 30 mol% and BSLCF Ca<sub>0.01</sub> with the commercial electrolyte such as YSZ or GDC.

3. To study the performance of single cell using BS<sub>0.9</sub>CCF, BSLCCF, BSLCFCa as a cathode.

## REFERENCE

- [1] Sharke, P. Freedom of Choice. *Mechanical Engineering* 126(2004): 33.
- [2] Tedmon, C.S.; Spacil, Jr.H.S. and Mitoff, S.P. *Journal of Electrochem. Society* 116(1969): 1170.
- [3] Lau, S.K. and Singhal, S.C. Potential electrode/electrolyte interactions in solid oxide fuel cells. *Corrosion* 85(1985): 1-9.
- [4] Juhl, M.; Primdahl, S. and Manon, C.; Mogensen, M. *Journal of. Power sources* 61(1996): 73.
- [5] Steel, B.C.H. and Bae, J.M. *Solid State Ionics* 106(1998): 255-261.
- [6] Wang, W. S. and Virkar, A. V. A. Conductimetric Humidity Sensor Based on Proton Conducting Perovskite Oxides. *Sensors and Actuators B: Chemical* 98(2004): 282-290.
- [7] Richter, J.; Holtappels, P.; Graule, T.; Nakamura, T. and Gauckler, L.J. Material design for perovskite SOFC cathodes. *Monatsh Chemistry* 140(2009): 985-999.
- [8] Zong, P. S. and Sossina, M. H. A high-performance cathode for the next generation of solid-oxide fuel cells. *Nature* 431(2004): 170-173.
- [9] Zhou, W. et al. Barium-and strontium-enriched  $(\text{Ba}_{0.5}\text{Sr}_{0.5})_{1+x}\text{Co}_{0.8}\text{Fe}_{0.2}\text{O}_{3-\delta}$  oxides as high-performance cathodes for intermediate-temperature solid-oxide fuel cells. *Acta Materialia* 56(2008): 2687-2698.
- [10] Shuyan, L.; Zhe, L.; Xiqiang, H.; Bo, W.; and Wenhui, S. Thermal, electrical, and electrochemical properties of Lanthanum-doped  $\text{Ba}_{0.5}\text{Sr}_{0.5}\text{Co}_{0.8}\text{Fe}_{0.2}\text{O}_{3-\delta}$ . *Journal of. Physics and Chemistry of Solid* 68(2007): 1707-1712.
- [11] Baumann, F.S.; Fleig, A. J.; Habermeier, H.-U.; Maier, J. and Planck, M.  $\text{Ba}_{0.5}\text{Sr}_{0.5}\text{Co}_{0.8}\text{Fe}_{0.2}\text{O}_{3-\delta}$  thin film microelectrodes investigated by impedance spectroscopy. *Solid State Ionics* 177(2006): 3187 -3191.
- [12] Tai, L.-W.; Nasrallah, M.M.; Anderson, H.U.; Sparlin, D.M. and Sehlin, S.R. Structure and electrical properties of  $\text{La}_{1-x}\text{Sr}_x\text{Co}_{1-y}\text{Fe}_y\text{O}_3$  Part 2. *Solid State Ionics* 76(1995): 273-283.

- [13] Tai, L.-W.; Nasrallah, M.M.; Anderson, H.U.; Sparlin, D.M. and Sehlin, S.R. Structure and electrical properties of  $\text{La}_{1-x}\text{Sr}_x\text{Co}_{1-y}\text{Fe}_y\text{O}_3$  Part 1. The system  $\text{La}_{0.8}\text{Sr}_{0.2}\text{Co}_{1-y}\text{Fe}_y\text{O}_3$ . *Solid State Ionics* 76(1995): 259-271.
- [14] Rim, H.R.; Jeung, S.K.; Jung, E. and Lee, J.S. Characteristic of  $\text{Pr}_{1-x}\text{M}_x\text{MnO}_3$  (M= Ca, Sr) as cathode material in solid oxide fuel cells. *Materials Chemistry and Physics* 52(1998): 54-59.
- [15] Mori, M.; Sammes, M.N. and Tmpsett, A.G. Fabrication processing condition for dense sintered  $\text{La}_{0.6}\text{AE}_{0.4}\text{MnO}_3$  perovskites synthesized by the coprecipitation method (AE = Ca and Sr). *Journal of Power Source* 86(2000): 395-400.
- [16] Liang, T.; Xuehong, G.; Li, Y.; Lixiong, Z.; Chongqing, W. and Nanping, X. Influence of sintering condition on crystal structure, microstructure, and oxygen permeability of perovskite-related type  $\text{Ba}_{0.8}\text{Sr}_{0.2}\text{Co}_{0.8}\text{Fe}_{0.2}\text{O}_{3-\delta}$ . *Separation and Purification Technology* 32(2003): 307-312.
- [17] Zong, P. S. and Sossina, M. H. A high-performance cathode for the next generation of solid-oxide fuel cells. *Nature* 431(2004): 170-173.
- [18] Yamazoe, N.; Teraoka, Y. and Seiyama, T. TPD and XPS Study on Thermal Behavior of Adsorbed Oxygen in  $\text{La}_{1-x}\text{Sr}_x\text{CoO}_3$ . *Chemistry Letters* (1981): 1767.
- [19] Wei, B. et al. Crystal structure, thermal expansion and electrical conductivity of perovskite oxides  $\text{Ba}_x\text{Sr}_{1-x}\text{Co}_{0.8}\text{Fe}_{0.2}\text{O}_{3-\delta}$ . *Journal of the European Ceramic Society* 26(2006): 2827-2832.
- [20] Chiwei, W. et al. Effects of Ca doping on the electrochemical properties of  $\text{LiNi}_{0.8}\text{Co}_{0.2}\text{O}_2$  cathode material. *Solid State Ionics* 177(2006): 1027-1031.
- [21] Guo, L.; Ding, X.; Liu, Y. and Gao, L. Effects of cation substitution on thermal expansion and electrical properties of lanthanum chromites. *Journal of Alloys and Compounds* 425(2006): 318-322.
- [22] Sun, J. et al. Effects of Ca doping on the electrochemical properties of  $\text{LiNi}_{0.8}\text{Co}_{0.2}\text{O}_2$  Cathode material. *Solid State Ionics* 177(2006): 1027-1031.
- [23] Su, W.; Li, S.; Lu, Z.; Huang, X. and Wei, B. Thermal, electrical, and electrochemical properties of Lanthanum-doped  $\text{Ba}_{0.5}\text{Sr}_{0.5}\text{Co}_{0.8}\text{Fe}_{0.2}\text{O}_{3-\delta}$ . *Journal of Physics and Chemistry of Solids* 68(2007): 1707-1712.

- [24] Ngampeungpis, W., Effects of doping metal ions on structures and properties of perovskites  $Ba_{0.5}Sr_{0.5}Co_{0.8}Fe_{0.2}O_{3-\delta}$ . *A Master Thesis*, Department of Chemistry, Faculty of Science, Chulalongkorn University, 2007.
- [25] Deepthi, N.R. et al. Ionic conductivity in new perovskite type oxides:  $NaAZrMO_6$  (A = Ca or Sr; M = Nb or Ta). *Materials Chemistry and Physics* 109(2008): 189-193.
- [26] Hirschenhofer, J.H.; Stauffer, D.B; Engleman, R.R. and Klett. Fuel cell Handbook, fifth Edition, Parsons Corporation Reading, West Virginia (U.S.), 2000.
- [27] Singhal, S.C. and Kendall, K., High Temperature Solid Oxide Fuel Cells. Fundamentals, Design and Application. *ELSEVIER*, 2003.
- [28] Muller, O. and Roy, R. The major ternary structural families. *Springer*, Heidelberg (1974).
- [29] Shannon, R.D. Revised effective ionic radii and systematic studies of interatomic distances in halides and chalcogenides. *Acta Crystallographica* A32(1976): 751–753.
- [30] Callister, W.D. *Jr. Materials science and engineering an introduction*. 6<sup>th</sup> edition, Wiley International Edition.
- [31] Rao, C. N. R.; Gopalakrishnan, J. and Vidyasagar, K. Superstructure. Ordered Defects and Nonstoichiometry in Metal Oxides of Perovskite and related Structure. *Indian Journal of Chemistry* 23A(4)(1984): 265-284.
- [32] Teraoka, Y.; Nobunaga, T.; and Yamazoe, N. Effect of Cation Substitution on the Oxygen Semipermeability of Perovskite-type Oxide. *Chemistry Letters* (1988): 503-506.
- [33] Zhan, Z.L.; Wen, T.L.; Tu, H.Y. and Lu, Z.Y. *Journal of Electrochem. Society*. 148 (5)(2001): A427.
- [34] Balazs, G.B. and Glass, R.S. Ac impedance studies of rare earth oxide doped ceria. *Solid State Ionics*. 76 (1995): 155-162.
- [35] Nagamoto, H.; Hayashi, K. and Inoue, H. Methane Oxidation by Oxygen Transported Through Solid Electrolyte. *Journal of Catalysis* 126 (1990): 671-673.
- [36] Singh, K.A.; Pathak, L.C. and Roy, S.K. Effect of citric acid on the synthesis of

- nano-crystalline yttria stabilized zirconia powders by nitrate-citrate process. *Ceramics International*. 33 (2007): 1463-1468.
- [37] Christie, G. M. and Berkel van, F. P. F. Microstructure-ionic conductivity relationships in ceria-gadolinia electrolytes. *Solid State Ionic* 83(1996): 17-27.
- [38] Richerson, D. W. Modern Ceramic Engineering, Properties, Processing and Use in Design, 2<sup>nd</sup> edition, 378-381p, 1992.
- [39] Rahaman, M.N. Theory of Solid-State and Viscous Sintering. *Ceramic and Sintering processing* 2<sup>nd</sup> edition, 471-486 p.
- [40] Coble, R. L. *Journal of Applied. Physics* 32(1961): 787-793.
- [41] Jorg, R.; Peter, H.; Thomas, G.; Tetsuro, N. and Ludwid, J. G. Materials design for perovskite SOFC cathodes. *Monatsh Chemistry* 140(2009): 985-999.
- [42] Tatsumi, I.; Kenichi, N.; Sachio O.; Makiko, E. and Hiroshige, M. Defect chemistry and oxygen permeation property of  $\text{Pr}_2\text{Ni}_{0.75}\text{Cu}_{0.25}\text{O}_4$  oxide doped with Ga. *Solid State Ionics* 179(2008): 1367-1371.
- [43] Jame, E. H.; Ellen, A. K. and Richard, L.K. Principles of Structure and reactivity. *Inorganic Chemistry* 4<sup>th</sup> edition, 188 p.
- [44] Bo, W. et al. Crystal structure, thermal expansion and electrical conductivity of perovskite oxide  $\text{Ba}_x\text{Sr}_{1-x}\text{Co}_{0.8}\text{Fe}_{0.2}\text{O}_{3-\delta}$  ( $0.3 \leq x \leq 0.7$ ). *Journal of the European Ceramic Society* 26(2006): 2827-2832.

## **APPENDIX**



## APPENDIX

### Density measurement

#### Theory Density

$$\rho_0 = M/Na^3$$

$\rho_0$  = Theory density

M = Molecular weight of each compound

N = Avocado Number ( $6.02 \times 10^{23}$ )

a = Lattice parameter (nm)

Note: The theoretical density used was  $5.874 \text{ g/cm}^3$  [Mori et al.].

#### Measure Density

$$\rho = \frac{Md \times \rho_{\text{liq.}}}{Mw - Ms}$$

$\rho$  = Measured density

Md = Dry weight

Mw = Wet weight

Ms = Solid weight

$\rho_{\text{liq}}$  = Density of liquid (at measuring temperature)

#### Relative density

$$\text{Relative density} = (\rho/\rho_0) \times 100 \%$$

**Ionic radius of metals****Table A.1** Ionic charge, coordination number, and ionic radius of concerned Metals [29].

<b>Ion</b>	<b>Ionic charge</b>	<b>Coordination No.</b>	<b>Ionic radius(Å)</b>
Ba	2+	12	1.610
Sr	2+	12	1.440
Co	2+	6	0.745
Co	3+	6	0.610
Co	4+	6	0.530
Fe	2+	6	0.780
Fe	3+	6	0.550
Fe	4+	6	0.585
Ca	2+	12	1.340
La	3+	12	1.360
Cu	1+	6	0.770
Cu	2+	6	0.730
Cu	3+	6	0.540
Zn	2+	6	0.740
O	2-	6	1.400

### Tolerance number

Goldschmidt (1926) defined the tolerance limits of the size of ions through a tolerance factor,  $t$  as Equation (A.1)

$$t = (r_A + r_O) / [\sqrt{2} (r_B + r_O)] \quad (\text{A.1})$$

where  $r_A$ ,  $r_B$ , and  $r_O$  are the radii of respective ions. For the substituted perovskite at A and B site,  $A_{1-x}A'_x B_{1-y}B'_y O_{3-\delta}$ ,  $r_A$  and  $r_B$  were calculated from the sum of each metal at A site and B site, respectively, times its composition.

**Table A.1** Tolerance factor of the BSCF perovskite doped.

Sample	Tolerance Factor Valence of $\text{Co}^{4+}$ , $\text{Fe}^{4+}$
<b>BSCF</b>	1.0459
<b>BSCa0.1CF</b>	1.0588
<b>BSCa0.2CF</b>	1.0521
<b>BSCa0.3CF</b>	1.0454
<b>BSCa0.4CF</b>	1.0386
<b>BSCa0.5CF</b>	1.0319
<b>BSLCF</b>	1.0536
<b>BSLa<sub>0.15</sub>Ca<sub>0.05</sub>CF</b>	1.0532
<b>BSLa<sub>0.1</sub>Ca<sub>0.1</sub>CF</b>	1.0528
<b>BSLa<sub>0.05</sub>Ca<sub>0.15</sub>CF</b>	1.0525
<b>BSLCFCa0.01</b>	1.0584
<b>BSCFCu0.05</b>	1.0459
<b>BSCFCu0.1</b>	1.0270
<b>BSCFCu0.15</b>	1.0087
<b>BSCFCu0.2</b>	0.9910

<b>Sample</b>	<b>Tolerance Factor</b> <b>Valence of Co, Fe = +4</b>
<b>BSCFZn0.05</b>	1.0457
<b>BSCFZn0.1</b>	1.0265
<b>BSCFZn0.15</b>	1.0079
<b>BSCFZn0.2</b>	0.9901

## VITAE

Miss Suwichar Deehasing was born on December 28, 1984 in Phetchaburi, Thailand. She graduated from Kasetsart University in 2006 with Bachelor Degree of General Science from Faculty of Liberal Arts and Science. She continued her study in program of Petrochemistry and Polymer Science, Faculty of Science, Chulalongkorn University in 2007 and completed in 20011.

### Presentation

22-25 June 2010

Poster Presentation “Influence of Cation Dopants in the A-Site on the Crystal Structure, Microstructure, and Electrical Conductivity of  $\text{Ba}_{0.5}\text{Sr}_{0.5}\text{Co}_{0.8}\text{Fe}_{0.2}\text{O}_{3-\delta}$  as a New Solid-Oxide-Fuel-Cell Cathode” The 3<sup>rd</sup> International Symposium on Organic and Inorganic Electronic Materials and Related Nanotechnologies (EM-NANO 2010), Toyama Conference Center, Toyama, Japan.

13-14 March 2010

Poster presentation “Structure and Electrical Conductivity of  $\text{Ba}_{0.5}\text{Sr}_{0.5}\text{Co}_{0.8}\text{Fe}_{0.2}\text{O}_{3-\delta}$  Perovskite Oxide Doped with Ca and La in A-site” International Symposium on Global Multidisciplinary Engineering 2010 (S-GME 2010), Nagaoka University of Technology, Niigata, Japan.

### Publication

“Influence of cation dopants in the A-site on the crystal structure, microstructure, and electrical conductivity of  $\text{Ba}_{0.5}\text{Sr}_{0.5}\text{Co}_{0.8}\text{Fe}_{0.2}\text{O}_{3-\delta}$  as a new solid oxide fuel cell cathode” in Japanese Journal of Applied Physics (JJAP)-Special Issue: Published.

Her present address is 29/3 M.8 Navong, Muang Phetchaburi, Thailand 76000.  
Tel: 0-86895-2228, E-mail: milky\_deeha@hotmail.com.